

DISS. ETH NO. 26171

**THz Quantum Cascade Laser: astrophysical applications
and high temperature performance**

A thesis submitted to attain the degree of
DOCTOR OF SCIENCES of ETH ZURICH

(Dr. sc. ETH Zurich)

presented by

LORENZO BOSCO

Master of Physics (Università degli Studi di Trento)

born on 02.01.1991

citizen of Italy

awaiting the recommendation of

Prof. Dr. Jérôme Faist, examiner
Prof. Dr. Carlo Sirtori, co-examiner
Prof. Dr. Alessandro Tredicucci, co-examiner
Dr. Giacomo Scalari, co-examiner

2020

Contents

Contents	i
Abstract	vii
Sommario	ix
Acknowledgments	xii
1 Introduction	1
1.1 The THz Quantum Cascade Laser	4
2 Processing Technology: Benzocyclobutene and Copper waveguides	10
2.1 THz QCL standard waveguides	11
2.2 Cu-Cu double metal waveguide	13
2.2.1 Wafer Bonding	15
2.2.2 Inductively Coupled Plasma-etching and Copper	20
2.2.3 Further notes	23
2.3 Benzocyclobutene (BCB) processing	23
2.3.1 Mask preparation	28
2.3.2 Making BCB mesas	28
3 High Temperature THz QCLs	30
3.1 Barrier and doping study	33
3.2 Radial position study	36

3.3	Operation above 200 K	38
3.4	Thermoelectrically cooled THz Quantum Cascade Laser	40
3.5	Conclusions	45
3.6	Processed samples	47
4	4.745 THz Local Oscillator for Radioastronomy	50
4.1	Heterodyne Measurement Principle	50
4.2	SOFIA: The Stratospheric Observatory For Infrared Astronomy	51
4.3	A local oscillator for SOFIA	53
4.4	Cavity Design	55
4.4.1	Back reflector: Distributed Bragg Reflector (DBR)	57
4.4.2	Amplification section: second order Distributed-Feedback (DFB)	58
4.4.3	Front reflector: first order DBR	62
4.4.4	Multisection tapering	65
4.4.5	Outcoupler	67
4.4.6	Simulation of the whole cavity	67
4.5	Results	70
4.5.1	First generation devices	70
4.5.2	Second generation devices	72
4.5.3	Third generation devices	75
4.6	Conclusions	80
5	InGaAs/GaAs based QWIP	82
5.1	The Quantum Well Infrared Photodetector	82
5.2	Design of InGaAs/GaAs quantum wells	85
5.3	Grating coupled double metal Mesa	88
5.3.1	IV measurement	89
5.3.2	Photocurrent spectra	90
5.3.3	Responsivity and LIV measurement	91
5.4	Antenna Enhanced QWIP	94
5.4.1	Cavity design and process	94
5.4.2	IV performance	97
5.4.3	Laser detection	97
5.5	Conclusions	100
6	Conclusion	101

Appendices	103
A Processing basic recipes	103
A.1 Au-Au double metal process	103
A.1.1 dry etched AlGaAs/GaAs structures	104
A.1.2 wet etched AlGaAs/GaAs structures	105
A.1.3 dry etched InGaAs/GaAs structures for QWIP	106
A.1.4 wet etched InP/InGaAs/InGaSb/AlInAs structures	107
A.1.5 Etching recipes	108
A.2 BCB processing recipes	109
A.2.1 BCB curing	109
A.2.2 BCB etching	109
B Electrical contact study	111
B.1 Pt/Au as top metallization and Au diffusion barrier .	111
B.2 GaAs as top contact layer	113
C Heat transfer computation and laser box design	115
List of Figures	120
List of Tables	126
Bibliography	128
Curriculum Vitae	137

Acronyms

AMSL above mean sea level.

AR Active Region.

Au Gold.

BCB Benzocyclobutene.

BtC Bound-to-Continuum.

Cu Copper.

CW continuous wave.

DBR Distributed Bragg Reflector.

DFB Distributed-Feedback.

DM Double Metal.

DP Direct Phonon.

EDX Energy-dispersive X-ray spectroscopy.

GREAT German REceiver At THz frequency.

HDPE high density polyethylene.

ICP Inductively Coupled Plasma-etching.

LLS lower level state.

LO Longitudinal Optical.

LO Local Oscillator.

MBE Molecular Beam Epitaxy.

mid-IR Mid-Infrared.

MM Metal-Metal.

NEGF Non-Equilibrium Green's Function.

NEP Noise Equivalent Power.

QCD Quantum Cascade Detector.

QCL Quantum Cascade Laser.

QWIP Quantum Well Infrared Photodetector.

RIE Reactive Ion Etching.

RP Resonant Phonon.

rpm rounds per minute.

RT room temperature.

SA Scattering Assisted.

SEM Scanning Electron Microscope.

SL superlattice.

SOFIA Stratospheric Observatory For Infrared Astronomy.

SP Single Plasmon.

Ta Tantalum.

TEC Thermoelectric Cooler.

THz Terahertz.

TPX Polymethylpentene.

ULS upper level state.

Abstract

The following PhD thesis is mostly based on the THz Quantum Cascade Laser (QCL), a semiconductor laser based on intersubband transitions in quantum wells. In Chapter 1 we introduce the state of the art of this technology. In Chapter 2 we treat the processing methods adopted in this thesis and, in particular, we report in detail the processing steps necessary to embed THz QCLs in Benzocyclobutene (BCB) and the challenges we faced when processing double metal waveguides replacing Gold (Au) with Copper (Cu). Chapter 3 treats the latest results on THz QCLs maximum temperature performance. Specifically, we report a systematic study involving 24 different epilayers and several processes. The conducted study culminated with a device operating up to the new world record of 210 K and able to emit a peak power of 200 mW at 40 K and 1.2 mW at 206 K, which paves the way to possible applications even when operated at high temperature. Moreover, thanks to the good high temperature performance, we demonstrate operation of a THz QCL cooled down with a thermoelectric cooler and we detect the laser radiation using a room temperature detector commercially available. This is the first demonstration of a cryogenics free

source-detector system that involves the use of a THz QCL and the most important achievement of this thesis. Chapter 4 is based on the design and development of a THz QCL used as a local oscillator for the heterodyne measurement of THz radiation coming from interstellar clouds and clusters, with a specific focus on detecting the [OI] cooling line at 4.745 THz. The local oscillator needs to satisfy several requirements, also given by the limitation of the used setup, mounted on a Boeing 747SP called Stratospheric Observatory for Infrared Astronomy (SOFIA). These requirements are operation above 40 K in continuous wave, output power > 1 mW with a single lobe far-field and single mode emission at 4.745 THz. The cavity is composed by several sections and their design exploits widely electromagnetic wave simulations. Moreover, the process involves the use of BCB and the deposition of a patch array antenna for the outcoupling of the THz radiation generated by the laser. At the end of this Chapter we will show that these devices manage to lase at the required frequency, emitting 4.5 mW in continuous wave (CW) operation at 45 K with an electrical dissipation lower than 4 W. Finally, the use of the patch array antenna shapes the beam pattern into a single lobe with a divergence angle of $\sim 30^\circ$. In the final Chapter, the same antenna design is also used in another project regarding the development of a microcavity THz QWIP and preliminary results are shown. The QWIP active region itself is a novelty because it is the first ever THz QWIP based on an InGaAs/GaAs active region. The use of the patch array antenna for the incoupling of the THz radiation allows to reduce the size of the electrical area of the device, favoring the reduction of the noise of the detector and an increase of the specific detectivity by two orders of magnitude compared to the reference QWIP employed in this thesis.

Sommario

Il lavoro di seguito presentato è basato per la maggior parte sui laser a cascata quantica nel THz (THz QCL), che sono laser a semiconduttore basati su transizioni tra sottobande che avvengono in pozzi quantici. Nel Capitolo 1 verrà introdotto lo stato dell'arte di questa tecnologia. Successivamente, nel Capitolo 2 tratteremo i metodi di fabbricazione che sono stati adottati in questa tesi e, in particolare, riporteremo dettagliatamente i passaggi necessari per fabbricare THz QCL che sfruttano il benzociclobutene (BCB) e le sfide superate per fabbricare guide d'onda a doppio metallo che rimpiazzano l'oro (Au) con il rame (Cu). Nel Capitolo 3, sono riportati i risultati più recenti sulla massima temperatura di operazione del THz QCL. Nello specifico, riportiamo uno studio sistematico coinvolgente 24 differenti *wafers* e numerose fabbricazioni. Lo studio condotto culmina in un nuovo record di temperatura presentando un THz QCL in grado di funzionare fino ad una temperatura di 210 K e di emettere 200 mW di potenza di picco a 40 K e 1.2 mW a 206 K, aprendo la strada a possibili applicazioni anche quando operato ad alte temperature. Inoltre, grazie alle buone prestazioni a temperature elevate, riusciamo a operare il THz QCL utilizzando una cella Peltier ed a rivelare il

suo segnale con un rivelatore commerciale a temperatura ambiente. Questa è la prima dimostrazione di un sistema sorgente-rivelatore privo di raffreddamento criogenico che utilizza il THz QCL e rappresenta il risultato più importante di questa tesi di dottorato. Il Capitolo 4 è basato sul *design* e lo sviluppo di un THz QCL da usare come oscillatore locale (LO) per una misura ad eterodina di radiazione THz proveniente da nubi interstellari ed ammassi stellari, con un interesse specifico per la rilevazione della linea spettroscopica [OI] a 4.745 THz. L'oscillatore locale deve soddisfare diversi requisiti, questi ultimi dati anche da limitazioni inerenti al *setup* sperimentale utilizzato che è montato su un Boeing 747SP che porta il nome di Stratospheric Observatory for Infrared Astronomy (SOFIA). Questi requisiti sono: funzionamento sopra i 40 K in onda continua, potenza in emissione > 1 mW con un campo lontano con profilo gaussiano ed uno spettro a singola frequenza a 4.745 THz. La cavità è composta da diverse parti ed il loro *design* è fatto con strumenti di simulazione per onde elettromagnetiche. Inoltre, la fabbricazione sfrutta il BCB e la deposizione di un'antenna a *patch array* per l'estrazione dell'onda THz generata dal laser. I dispositivi fabbricati soddisfano le condizioni imposte, emettendo radiazione alla frequenza richiesta con una potenza di 4.5 mW in onda continua a 45 K e dissipazione elettrica inferiore ai 4 W. Infine, l'uso dell'antenna ha consentito l'emissione di un campo lontano a singolo lobo con angolo di divergenza di $\sim 30^\circ$. Nell'ultimo Capitolo, lo stesso tipo di antenna precedentemente introdotta viene utilizzato per la realizzazione di un rivelatore infrarosso a pozzo quantico nel THz (THz QWIP) basato su una microcavità. La regione attiva utilizzata per il THz QWIP è essa stessa innovativa dacché basata per la prima volta su un'eterostruttura InGaAs/GaAs. L'uso dell'antenna a *patch array* per l'accoppiamento della radiazione THz incidente permette di ridurre le dimensioni dell'area elettrica del dispositivo,

favorendo di conseguenza la riduzione del rumore del rivelatore e l'incremento della rilevanza specifica di due ordini di grandezza rispetto al QWIP di riferimento utilizzato in questa tesi.

Acknowledgments

First and foremost, my deepest gratitude goes to Prof. Jérôme Faist. His scientific support and incredible experience have been an essential ingredient for the success of my PhD. I will forever envy his outstanding ability to always find the time to micromanage his group, discuss results and problems with its members, on top of all the duties of his professional and personal life. Jérôme has been extremely inspiring for me even beyond the simple academic aspect and I will treasure the time I have spent in his group forever. Secondly, I thank Dr. Giacomo Scalari for being a more than valid mentor during my PhD. I enjoyed the scientific discussions with him as well as his ability to keep the group unite and the *troop* morale high; an important asset for large research groups. Special thanks also go to Dr. Keita Ohtani and Dr. Christopher Bonzon, as they have introduced me to the basics of research in Jérôme's group and taught me all those fundamental tools which I have exploited extensively during my PhD. Their patience and kindness have been precious for my professional growth. I also thank Prof. Carlo Sirtori and Prof. Alessandro Tredicucci for having accepted to be co-examiner of this thesis with a really short notice and to read this manuscript in an extremely shorter time, at the limit of

the ETH regulations. I promise that for the next PhD thesis I will grant a bit more time...!

In these last almost five years I have met with a lot of scientists to whom I am really grateful. First, I thank all my colleagues; both their scientific and psychological support are other important ingredients of the work I have presented in this thesis. Specifically, I thank Dr. Mattias Beck, Dr. Martin Franckié and Dr. Elena Mavrona for the easy-going and successful collaboration that led to a new temperature record for the THz Quantum Cascade Laser. I thank Tudor Olariu for the help given in characterizing a lot of lasers and for fruitful discussions. I also thank the Workshop team, led by Andy Stüker, for their outstanding work always carried on in a short time due to my numerous last minute express orders. I thank the FIRST team, especially Dr. Yargo Bonetti and Sandro Loosli, for keeping such a good and organized environment in the cleanroom, where I have spent a consistent part of my PhD. My gratitude goes also to both my former and present office mates, Dr. Johanna Wolf, Dr. Bo Meng, Zhixin Wang and Dr. Ruijun Wang for the nice working atmosphere and the chance of a quick but relaxing chitchat at any rate. Although in different times, I had plenty of fun with Dr. Borislav Hinkov, Dr. Ileana-Cristina Benea-Chelms and Fabiana Settembrini during our training sessions at ASVZ and I will always miss them as training fellows. I thank Ms. Erna Hug for the incredible patience she has shown every time I entered her office to ask about non-physics related questions and issues (I really had more than it is acceptable to admit!) and I hereby apologize for all the bureaucracy issues I have consistently and timely been able to create and misdo during my whole PhD. I thank all the rest of my colleagues which I did not have the chance to address one by one in this acknowledgments; I am sure I will never be able to

find another group with people so motivated, goal-oriented and friendly at the same time. Undoubtedly the best people a PhD candidate can hope to find!

As if I were not already lucky enough with my colleagues, I am really glad to also say that I could always rely on the constant presence of my friends. You have always been the best mean to take a relaxing break and a good laugh. Thus, I thank the “*Nerd Team*” for all the numerous nights (I hope more to come) spent playing together an endless series of games and for all the discussions about literally any topic. My devotion also goes to “*I Ciccioni*”, the group of most brilliant and valid guys I have ever met. It is also thank to them if I have ever completed my bachelor and master degree and if I learned, to my modest capabilities, to be curious about everything. I thank especially Alberto, who has also been more than an excellent flatmate in the last four years here in Zurich. To all these friends and me, although time and “adulthood” have separated us in space scattering us all across Europe, I wish always to be able to fill this distance with any possible mean, being a plane, a train or a laugh in any voice chat.

I thank my family; recent times have been tough on us but we will never cease adapting. My love goes especially to *kid 1* and *kid 2*, as I teasingly call my niece and nephew respectively; on you resides my hope for a brighter future and the irreplaceable pleasure of making you laugh.

Finally, I thank my biggest luck: Valeria. I have stepped in and out numerous challenges, this thesis being one of the most recent ones but definitely not the last, but if any of these challenges ever had been meaningful I owe it only to you. Thanks for being at my side.

Chapter 1

Introduction

The term Terahertz (THz) indicates the range of the electromagnetic spectrum that is included between 0.3 and 10 THz. THz technology is the chain ring connecting two extremely developed fields; on the lower frequency side there is the electronics, while the higher frequency side is referred to as optics. "Sandwiched" between these two fields which play

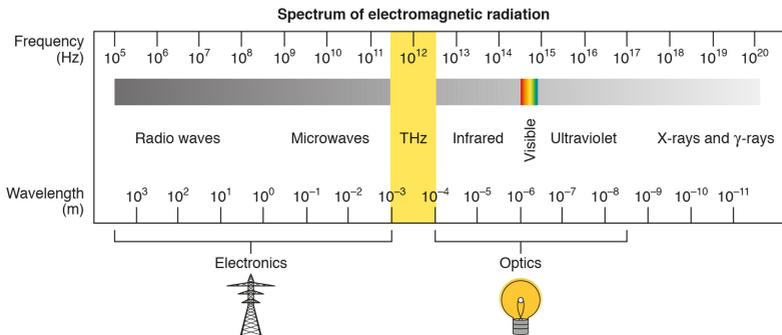


Figure 1.1: Electromagnetic spectrum. Image adapted from [1].

a major role in modern technology, only in the recent years the THz range is becoming subject to a wide range of research and

technological efforts with the goal of filling the so-called *THz gap* [2,3]. The advantages presented by this frequency range are several. First of all, since there are several materials (*e.g.* textiles, plastics and coatings) which are transparent to THz radiation, this spectral region is promising for a variety of non-invasive imaging and non-destructive testing used for quality assessment applications. Some examples are airport security screening and concealed material identification [4], as shown in Fig. 1.2.a, thickness coating measurements, which is an important step of industrial fabrication of several technologies, or also food quality assessment. Secondly, the penetrative power of THz radiation

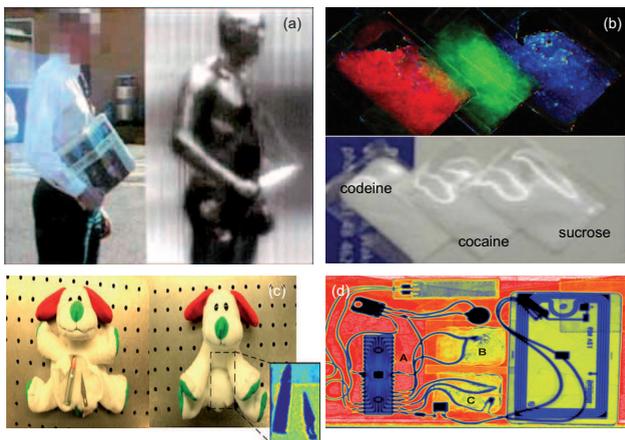


Figure 1.2: Examples of application of terahertz radiation in security (a,b,c) and process control (d). Adapted from [5] and based on [3,6–8].

in biological tissues and the fact that some spectral regions of the THz radiation are highly absorbed by water are also an interesting feature of this spectral region. Indeed, this property can be used to investigate on the level of hydration of tissue at depth and with a resolution unavailable by other spectral regions.

Recently, this feature led to an *in vivo* measurement of a basal cell carcinoma, a skin cancer which contours are not always easy to identify otherwise [9]. When it comes to communication, THz can offer a higher bandwidth than millimeter wavelengths (< 100 GHz) and wi-fi frequency bands (2.4 and 5.0 GHz) keeping at the same time a higher tolerance to alignments than optical signals. For these reasons, THz frequencies are also being investigated as a possible future generation for telecommunication systems. Finally, a high interest in THz comes from spectroscopic application. In this frequency range, indeed, unique fingerprints for several molecules and atoms can be found. Among these elements, the cooling lines of [OI] and [CII] (4.745 THz and 1.9 THz, respectively) represent important transitions for the astrophysics community, as these cooling lines give information on star formation processes in interstellar clouds. Exactly on this topic, a research application that will later be treated in this thesis work is the Stratospheric Observatory for Infrared Astronomy (SOFIA), an airborne laboratory equipped with a telescope and capable of doing spectroscopy of several elements in the whole THz range [10].

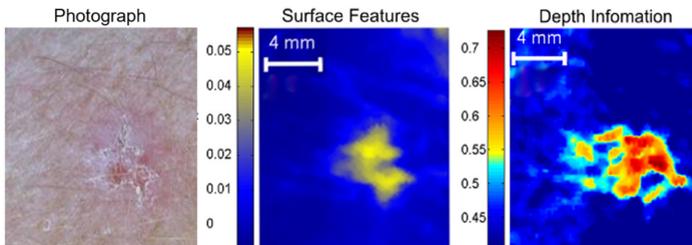


Figure 1.3: Example of imaging of a basal cell carcinoma; thanks to THz imaging is possible to uncover feature under the skin which would be otherwise invisible with simple optical imaging. Adapted from [2].

1.1 The THz Quantum Cascade Laser

In order to unlock the full potential of these applications on a large scale, compact and powerful THz sources are needed. A candidate is the terahertz Quantum Cascade Laser (QCL) [11], a compact injection laser based on semiconductor heterostructures and engineered using a similar approach as the Mid-Infrared (mid-IR) QCL, invented just 8 years before, in 1994, by Faist et al. at Bell Labs [12]. In fact, the first operating design applied for a THz QCL, called chirped superlattice (SL), took inspiration from a design already present and really successful for the mid-IR QCL [13] and based on AlGaAs/GaAs heterostructures [14]. Meanwhile in 2002 the mid-IR QCL reached continuous wave operation at room temperature with 17 mW output power [15], at that time the "newborn" THz QCL was limited to a maximum temperature of 50 K and pulsed mode operation at low duty cycle with an output peak power of ~ 2.5 mW. Over the last almost 20 years, several THz QCL designs have been developed, each provided with advantages and flaws. Quite immediately after its invention, the THz QCL adopted the Bound-to-Continuum (BtC) scheme [16–20], shown in Fig. 1.4 (b-c), where the upper level state (ULS) is localized in one quantum well and population inversion is achieved by a combination of tunneling transitions and LO phonon scattering, used to inject the electrons into ULS. The main limitation resides in the miniband, which characterizes the structure, since this tends to favor re-absorption of photons by thermally populated states, hindering performance at higher temperature and limiting it to less than 150 K. Nonetheless, the BtC scheme is up to now the design that obtained the highest output peak power (> 1 W), with a wall plug efficiency (WPE) higher than 1% [21]. To reduce re-absorption issues and improve population inversion, the Resonant Phonon (RP) scheme

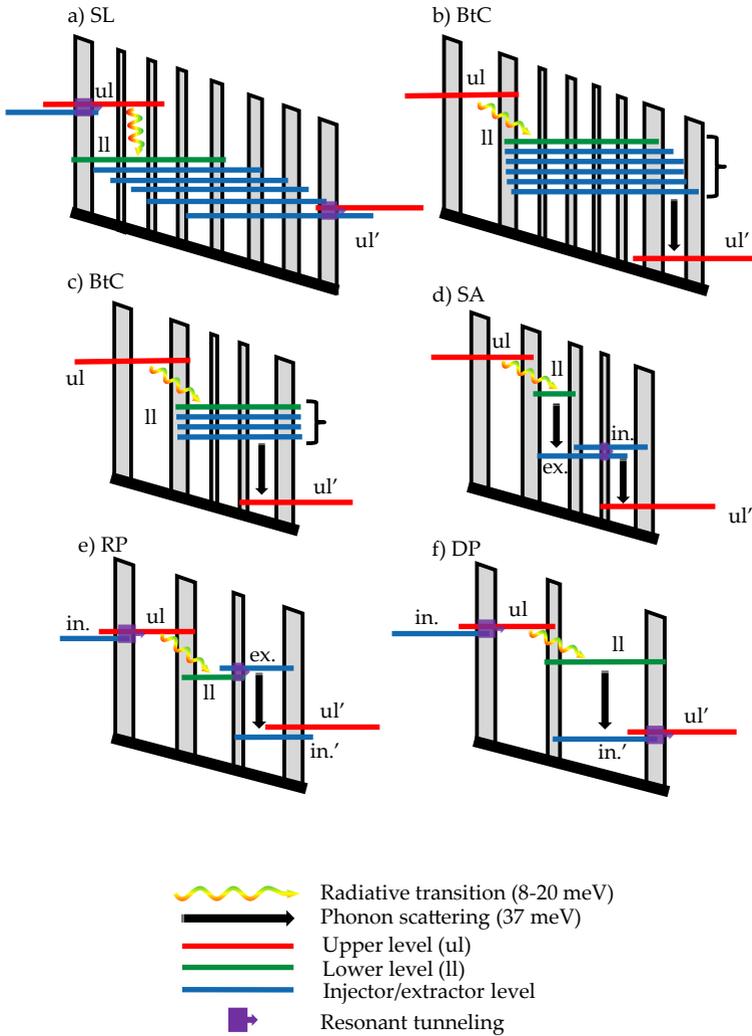


Figure 1.4: Schematic of several THz QCL designs a) Chirped Superlattice (SL). b) Bound-to-Continuum (BtC) realized with 7 quantum wells. c) Bound-to-Continuum (BtC) realized with 4 quantum wells. d) Scattering Assisted (SA). e) Resonant Phonon (RP). f) Direct Phonon (DP). At the bottom a legend shows the meaning of each used symbol.

[22, 23] – schematized in Fig.1.4 (e) – achieves efficient lower level state (LLS) extraction exploiting Longitudinal Optical (LO) phonon scattering for extracting the electron from the LLS. To this date, the highest temperature performance of 199.5 K [24] has been achieved by an RP design which uses only four states in a 3 quantum wells structure. The Scattering Assisted (SA) injection design [25] achieves good performance using only 4 active states, but exploiting twice per period the LO phonons for injection and extraction as shown in Fig.1.4 (d), presenting low absorption losses when the design is engineered for lower frequencies. The minimum number of active states for a THz QCL is three, limited by the electrical stability of the laser [26,27], and it has been realized in Direct Phonon (DP) two-quantum well designs [23, 28]. The schematic is shown in Fig.1.4 (f). However, the 2-well designs are extremely sensitive to small modifications of the layer thicknesses and only in recent years with the improvement of simulation tools – in particular using Non-Equilibrium Green’s function (NEGF) models – it has been possible to achieve close-to-record temperature performance [29, 30].

Although still not comparable in performance to its mid-infrared counterpart, the THz QCL technology has already shown high emitted powers (several hundreds mW both in pulsed and continuous wave) [21,31,32] and spectral coverage throughout the 1-6 THz range [33] with single mode and broadband devices [34]. Moreover, since they are based on III-V semiconductors, specifically GaAs/AlGaAs, the THz QCLs can rely on well known and well controlled fabrication processes. However, the THz QCL is still strongly limited by its poor temperature performance, which represents the biggest challenge to face for this technology in order to unlock practical and widespread applications. In

Fig.1.5, the maximum operating temperature of the THz QCL is reported over time, specifying explicitly the number of quantum wells employed in the design that has reached that particular temperature. The plot reports also the new temperature record

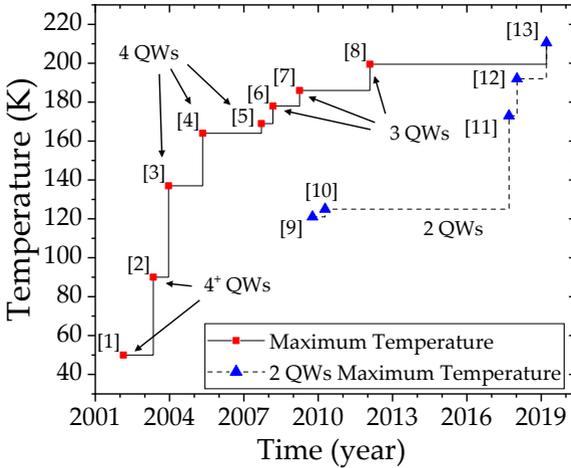


Figure 1.5: The trend of the THz QCL T_{\max} over the years with the latest results achieved in this thesis. Also the trend of the maximum temperature of the two quantum well designs is reported. Data taken from [11, 16, 23, 24, 35–38] for the maximum temperature and from [28–30, 39] for the 2-well performance.

of 210 K, achieved during this PhD work and later discussed in Chapter 3. Two things here must be noticed: the first is that there seems to be a correlation between the reduction of the number of quantum wells and the increase in maximum operation temperature, hinting that designs with a smaller number of quantum wells are desirable for high T performance. Later in Chapter 3 we will show that the trend is dependent on the number of quantum states on which the structure is based. Secondly, the large temperature improvement in two quantum well

designs in the last few years is an optimistic sign that in the near future we could expect further improvement of the performance in this regard. Achieving high temperature operation for THz QCLs is indeed an important challenge for the THz scientific community, which is also exploring alternative solutions to the standard AlGaAs/GaAs heterostructure QCLs. Worthy of mention is the intracavity difference frequency generation in mid-IR QCL [40], which has already been achieved at room temperature [41], but it is limited in output power due to intrinsically low conversion efficiency of the nonlinear down-conversion process. Other solutions are based on modifications of the Active Region (AR) material in order to reduce phonon scattering which is a source of losses at high temperature. Solutions that are being investigated are based on switching to heterostructures with non polar optical phonons [42] (SiGe) or higher energy phonons [43,44] (ZnO/ZnMgO and GaN/AlGaN).

In this framework, this PhD thesis pushes further on the limit of the AlGaAs/GaAs THz QCL structures, presenting a systematic study performed on two quantum well designs which eventually brought to a new world record in maximum temperature performance. Moreover, the first THz Quantum Cascade Laser thermoelectrically cooled is presented, with output peak powers up to 1.2 mW at 206 K. Such a power might lead, through appropriate setup design, to do THz self-mixing imaging in a cryogenics free THz QCL [45]. The first Chapter of this manuscript introduce the methods employed over the last four years for the processing and fabrication of THz QCLs. Chapter 3 will then introduce the systematic study on 2-well designs and the temperature achievement here briefly discussed. In Chapter 4, a design cavity specifically engineered for astrophysical measurements on SOFIA is presented. The design has been

developed in a successful collaboration with Dr. Matthias Justen of Köln university. The THz QCL that is based on this design has been now used for more than 30 flights on SOFIA as a local oscillator for heterodyne measurements at 4.745 Thz and it represents a good example of a technological application for which the THz QCL can be used. In Chapter 5 a short investigation on InGaAs/GaAs based quantum well infrared photodetectors (QWIP) is presented. Moreover, using the same patch array antenna applied for the development of SOFIA's local oscillator presented in Chapter 4, we show how to reduce drastically the size of the QWIP active region keeping a large optical collection area and increasing the specific detectivity of the detector.

Processing Technology: Benzocyclobutene and Copper waveguides

Processing and process development have been a large part of the presented PhD thesis. In the following chapters, structures and devices whose realization is based on the use of Benzocyclobutene (BCB) or on the use of Copper (Cu) are presented. Improving the fabrication steps involving the above cited materials has been demanding but important for the development of this work and, as we will see, the misuse of these materials can lead to undesired results.

After a brief introduction to the concept of THz waveguide for QCL, the following sections explains how to handle these materials and the reason why their use can help the fabrication of better performing THz devices.

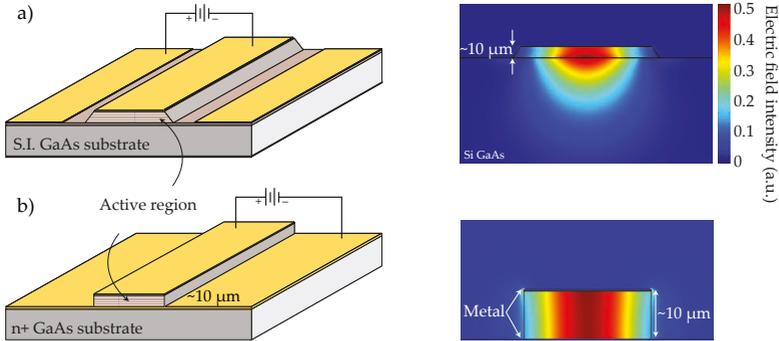


Figure 2.1: Drawing and cross section simulation of a) single plasmon waveguide and b) double-metal waveguide. Adapted from [31].

2.1 THz QCL standard waveguides

THz QCLs can be processed in two different ways: either as Single Plasmon (SP) waveguides or as Double Metal (DM) waveguides, also called Metal-Metal (MM) waveguides [31]. Schematic examples and respective simulations are shown in Fig.2.1.a and Fig.2.1.b, respectively. For the SP waveguide the AR is placed on top of a semi-insulating GaAs substrate with a thin heavily doped layer grown on top. A metal contact is deposited on the active region and the active material is etched into ridges. In this way the electromagnetic wave emitted by the QCL is confined in a mode which is a compound between the single plasmon mode bound to the top metal contact and the lower doped layer. On the contrary, the DM waveguide replaces the bottom heavily doped layer with a metal cladding, squeezing the electromagnetic wave in a sub wavelength region. Waveguides are defined by 3 parameters:

- Waveguide losses α_w describe the losses due to the free carriers absorption and the metal claddings
- Mirror losses α_m depend on the reflectivity of the facet of the

waveguide according to the relation

$$\alpha_m = \frac{1}{2L} \ln \left(\frac{1}{R_1 R_2} \right) \quad (2.1)$$

with L cavity length, R_1 and R_2 reflectivity of the two facets.

- Mode overlap Γ quantifies which ratio of the electromagnetic wave profile is confined in the active region. This value goes from 0 (no confinement) to 1 (all the electromagnetic wave is confined inside the AR).

The threshold gain g_{th} of a laser can be expressed in function of all the above values according to the relation

$$\Gamma g_{th} = \alpha_w + \alpha_m \quad (2.2)$$

In the case of the SP waveguide, waveguide losses are smaller than DM configuration but also Γ is, with typical values between 0.2 and 0.5. Moreover, the waveguide width is constrained to be larger than 100 μm in order to reduce the leakage of the electromagnetic mode into the substrate. SP waveguides exhibit high mirror losses due to low reflectivity (32%) given by the index mismatch between the AR and the vacuum. On the contrary, DM waveguides have low mirror losses because the subwavelength-confined mode ($\Gamma \sim 1$) in the waveguide is highly mismatched with the free-space propagating mode, enhancing the facet reflectivity up to even 90%. Thanks to the lower mirror losses and the higher mode overlap, DM waveguides perform better in temperature with higher maximum temperature than the SP waveguide. Hence, for the purpose of this PhD work, only DM waveguides have been processed. The standard processes used for double metal waveguide fabrication in this thesis are reported in the Appendix.

2.2 Cu-Cu double metal waveguide

The use of Cu in electronics and optoelectronics is not a novelty, and its adoption for Si and CMOS technology is now well established, despite the difficulty of developing a reliable process [46]. In the THz range, copper offers both a better thermal conductivity (hence better thermal dissipation) and lower optical losses [47, 48], desirable by most optoelectronic devices. For this reason, the THz community working on THz QCLs has substituted gold in some of their application in favor of Cu, more specifically for double metal processes of THz waveguides [24, 38, 47, 49]. In particular, in this work the interest on Cu arises from the need to improve the temperature performance of THz QCLs, leading to the results later introduced in Chapter 3.

The steps of a Cu-Cu double metal waveguide process are summarized in Table 2.1 and schematized in Fig.2.2.

N.	Processing Step	Details
1	Cleaving and cleaning	using ACE:ISO:H ₂ O
2	Metallization	Ta/Cu (5/500 nm) (E-beam evaporation)
3	Wafer Bonding	6 MPa, 300 °C for 60 minutes with post annealing at 300 °C in vacuum
4	Lapping	
5	Selective substrate removal	Citric Acid 50% (3:1 with H ₂ O ₂) at 35 °C
6	HF etching	40% concentration for 3 minutes
8	Top contact Photolitho and Evaporation	Ta/Cu/Ti/Au (5/200/20/50)
9	Hard mask deposition, photolitho and dry etching	3 μm of SiN _x
10	Ridges dry etching	Room Temperature etching using Cl ₂ /Ar plasma
11	Back lapping	Thinning down to ~ 200 μm
12	Back evaporation	Ti/Au (10/50) for back-end InAu soldering
13	Sample de-chlorination	Using ~ 1% HCl for 5 seconds
14	Hard mask removal	Buffered HF (1:5) for 3 minutes

Table 2.1: Summary of the main steps for a Cu-Cu double metal waveguide fabrication. Further details on the used recipes and similar processes in the Appendix.

The most critical steps of the process are the wafer bonding, at the beginning of the process, and the dry etching of the ridge, which, instead, finishes the fabrication. The processing steps in between show almost no difference compared to the standard Gold (Au) process carried out in our cleanroom facilities, but few notes regarding these steps will be added in the final subsection of this paragraph.

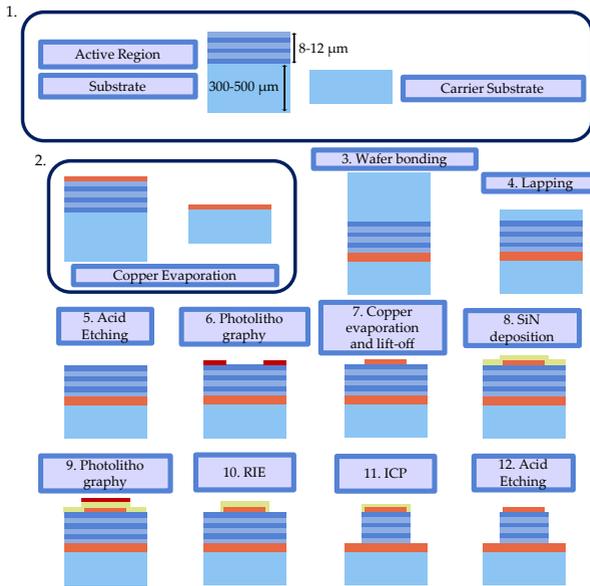


Figure 2.2: Schematic illustration of the double-metal processing steps with Cu.

2.2.1 Wafer Bonding

Tantalum (Ta) is used as an adhesion layer and diffusion barrier of Cu metallization. Right after the evaporation of a Ta/Cu layer on the active region chip and on a carrier substrate, the structure is

bonded by thermocompression. Chips that do not undergo wafer bonding immediately after the evaporation of the metal should be kept in a nitrogen box or in an Isopropanol bath in order to avoid oxidization of the Cu until it is possible to proceed to the bonding step. If a layer of CuO_x is present on the top of the surface, glacial Acetic Acid ($\sim 100\%$ purity) reacts with the copper oxide removing it without attacking the Cu itself or the active region layers [50].

Copper bonding procedures for THz QCLs have already been reported in literature [36,38,47]. Nonetheless, a systematic study of the wafer bonding process has been performed in order to improve the fabrication quality. Thermocompressive bonding tests at different temperatures have been conducted at 300, 350 and 400 °C. The bonds have been done in vacuum ($< 10^{-4}$ mbar), applying a pressure of ~ 6 MPa on the samples for a duration of 60 minutes. After that, the samples have been cooled down passively without releasing the applied pressure down to < 150 °C. After the cooling, the samples underwent a 30 minutes annealing step at the same temperature as the bonding and still under vacuum conditions.

Following a cross section SEM characterization, the process performed at 300 °C showed to have the least possible amount of voids along the bonding interface. Fig.2.3 shows a comparison between the bonded interfaces obtained performing the wafer bonding at different temperatures. Here, the bonding performed at 300 °C presents less and smaller voids compared to the ones performed at higher temperatures. It must be noted that all three samples present regions where the bonding is flawless and void-free. However, at higher temperature these regions are less frequent and they extend for shorter lengths along the interface compared to the 300 °C bond. Eventually, the bonding has been performed by applying a pressure of 6 MPa on the sample at 300 °C for 60 minutes followed up by cooling down under pressure

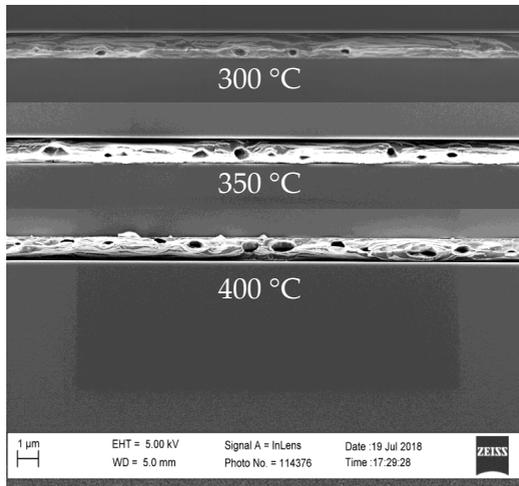


Figure 2.3: Bonding interface comparison between thermocompressive bonding performed at different temperatures as indicated in the labeling. When moving to lower temperature, the bonding interface shows smaller and sparser voids.

to a temperature lower than 150 °C before releasing the platens. After the mechanical pressure has been removed, the sample is annealed at 300 °C for 30 minutes under vacuum. Finally, after the cool down, the sample is removed from the chamber and the fabrication continues with the lapping as shown in Table 2.1. It must be noted that in order to have a higher yield for the wafer bonding, it is better to cleave chip of small size in order to avoid to build up too much thermal stress during the thermal expansion of the sample. For this reason all the Cu-Cu processes performed during this thesis will employ $9 \times 10 \text{ mm}^2$ chips.

Possible issues due to Temperature misreading

The wafer bonding step has probably proven to be the most critical step of the process. This step influences strongly the outcome of

the fabrication; the presence of defects at the bonding interface can lead to higher optical losses and to a laser with bad thermal dissipation properties. In some cases a poor wafer bonding can even determine cleaving issues when mounting the laser in the back-end part of the fabrication. Moreover, its success is difficult to forecast before the citric acid etching step (step 5 of the schematic in Fig.2.2). Indeed, only after this step the surface of the active region is exposed allowing to investigate it through optical microscope analysis. The active region surface can show defects (small cracks along the crystalline planes) that are connected to an incorrect bonding. However, this kind of analysis is not always enough to predict the outcome of the bonding. Specifically, in the initial tests we used 400 °C for the wafer bonding step and we observed diffusion of copper into the GaAs. To observe this issue it is needed to etch the active region to uncover the bottom cladding (step 11 of Fig.2.2) in order to see if any Cu diffused. In Fig.2.4.a, a typical feature of a process where the Cu diffused inside GaAs (black spots and stripes) is shown. The black regions, which in the figure form an intricate groove of structures on the top of the bottom metal, shows a continuity when passing "below" the ridges, indicating that the phenomena leading to the formation of these structures happened before the ICP etching. A further Energy-dispersive X-ray spectroscopy (EDX) analysis of the sample is shown in Fig.2.5. In the raw top-view Scanning Electron Microscope (SEM) image, light gray regions between the laser waveguides (darker stripes) are visible. These regions correspond to the black diffusion spots shown in Fig.2.4.a. The composition analysis indicated a strong presence of both Cu and GaAs on the surface of the bottom contact, as shown in different colors in the figure. A point analysis of the sample revealed that the black features are composed 31% by Ga, 35% by As and 34% by Cu, while the rest of the bottom contact is generally 99.7% Cu.

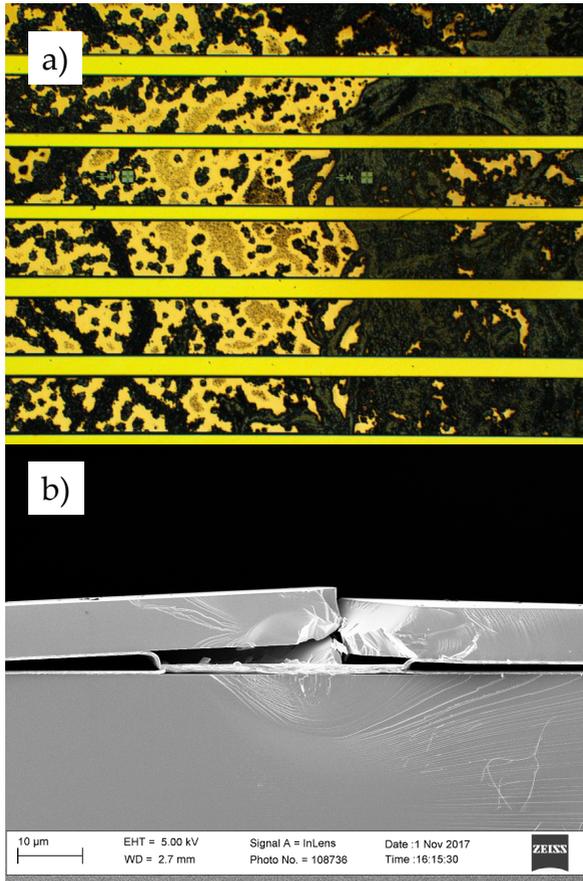


Figure 2.4: a) Top view of a Cu-Cu process in which we observed copper diffusion into GaAs. It is clear that the black stripes, which are regions where the Cu diffused, are passing "below" the ridges, hinting that the problem arose at the interface between the carrier substrate and the sample. b) Temperature difference between the top and bottom plate during the wafer bonding will lead to differences in thermal expansions between the Cu and the active region, accumulating thermal stress and thus leading to stress release on the sample. Both these samples have been bondeed at 400 °C.

Together with the optical microscope picture, this confirms the suspect that Cu diffused through Ta into GaAs, jeopardizing the performance of the laser due to an increase in optical losses (rough interface). Such diffusion phenomena, reported in literature a long time ago [51], is triggered by a too high bonding temperature ($> 400\text{ }^{\circ}\text{C}$). Although in [52] the diffusion phenomenon seems to have a threshold at $> 500\text{ }^{\circ}\text{C}$, well above the temperature we use, probably the presence of a compression pressure facilitates the process. Moreover, at the beginning of this work, a reading error of the electronics made us bond between 20 and 30 $^{\circ}\text{C}$ above 400 $^{\circ}\text{C}$. Copper bonding is also sensitive to mismatch in the platens temperature as we observed during the initial tests when we increased the Ta barrier thickness up to 30 nm in order to limit Cu diffusion. This effectively stopped the diffusion, but an electronic issue in the wafer bonding machine led to a misreading of the upper platen temperature of $\sim 20\text{ }^{\circ}\text{C}$. This temperature difference between top and bottom platen led to thermal expansion stress on the sample. Fig.2.4.b reports an example of such a situation. In the cross section SEM picture, the Cu interfaces of the active regions and the carrier substrate are in contact only in the center. The top part of the sample is cracked and the bottom shows several stress lines corresponding to the breaking point. This stress is probably caused by the mismatched thermal expansion of the bottom and top wafer.

2.2.2 Inductively Coupled Plasma-etching and Copper

In our cleanroom facilities, the Inductively Coupled Plasma-etching (ICP) for non selective-etching of GaAs/AlGaAs active regions uses a Cl_2/Ar plasma. Unfortunately, although effective, this plasma etches also metals, forcing the operators to use hard masks in order to etch the laser ridges, on the contrary of

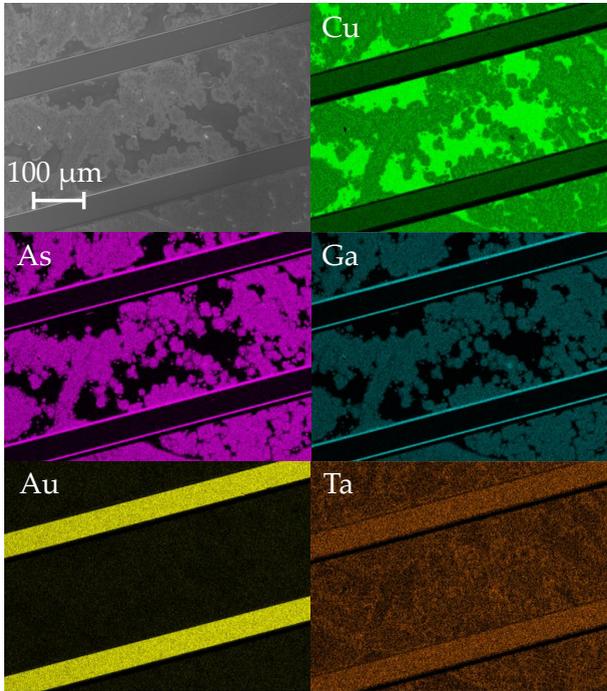


Figure 2.5: EDX analysis of a SEM picture, shown on the top left, taken from a sample where Cu diffused into GaAs. Brighter colors correspond to a higher percentage of the specified element. The analysis shows that there is presence of Cu diffused into GaAs.

other self-aligned processes – like the ones based on SiCl_4 plasma – which are etching-selective for metals [36]. Moreover, when Au is used, the exposition of the metal to the plasma leads to the sputtering of the gold on the ridge sidewalls, causing sometimes structures short circuiting or, more commonly, higher waveguide losses [5]. When the Cu is substituted to Au, instead, the metal quickly reacts with Cl_2 forming CuCl_x as a layer on top of Cu as shown in Fig.2.6.a. This process is called *chlorination* and it can also be used for selective patterning and etching of Cu [53]. In

our specific case, lacking the right gas for self aligned processes, it represents an advantage because it reduces sputtered metal on the walls, although EDX analysis has shown that Cu is still partially sputtered. In Fig.2.6.b, the same sample shown in image (a) is shown after treatment with 6% HCl acid for 1 second, that proved to be enough time to remove completely the CuCl_x . However, HCl does etch GaAs, thus a concentration of 1% of acid has been used in the final processes in order to reduce the risk of undesired etching. With this solution concentration, CuCl_x removal happens in ~ 5 seconds.

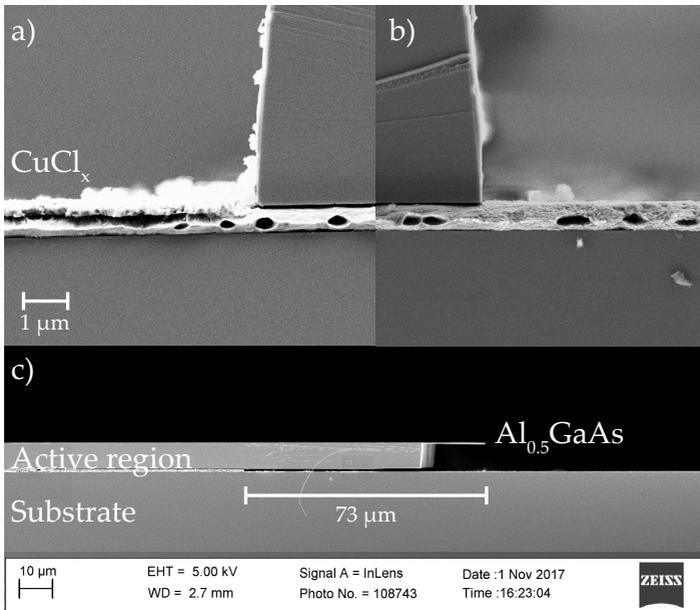


Figure 2.6: a) Cross section SEM of a sample right after the ICP dry etching step with a Cl_2/Ar plasma. On top of the bottom contact a thin layer of CuCl_x forms. b) Cross section of the previous sample after the HCl etching, which removes the CuCl_x . c) Low magnification cross section of the edge of a bonded sample just etched with 50% Citric Acid (in a 3:1 solution with H_2O_2). Copper is etched by this Acid, but the penetration depth of the acid in the interface is usually limited below 100 μm .

2.2.3 Further notes

Compared to gold, copper is a highly reactive metal. Apart from Cu diffusion into GaAs, chlorination and, of course, oxidation, Cu is etched by Citric Acid solutions. This is noticeable during the selective etching employed for the substrate removal right after the mechanical lapping (step 5 of the schematic process reported in Fig.2.2). However, as shown in Fig.2.6.c, this effect is not harmful for the process as the Cu interface etching depth of the bonded sample is usually limited to $< 100 \mu\text{m}$. Moreover, Copper reacts with Iodine, present in some Au-etching solution, forming Copper Iodide (CuI). Removal of Iodine can be achieved using Acetonitrile, a solvent which does not attack the active region nor the Cu.

2.3 BCB processing

The use of BCB is well justified by both the insulating properties of the material and the low absorption in the THz range, as shown in Fig.2.7 [54]. Moreover, the real part of the refractive index of benzocyclobutene is $n_{\text{real}} \simeq 1.55$ in the THz spectrum, allowing a good refractive index contrast with the III-V semiconductors employed for the active region of THz devices. In fact, successful applications of BCB for the fabrication of THz QCLs can be found in literature [55–58]. For the purpose of this work, Cyclotene 3022-57 has been used in order to implement metallic patch array antennas in the top metal cladding of the device waveguides. The antenna has been used for the outcoupling or incoupling of an electromagnetic radiation around 4.745 THz, which corresponds to $\sim 158 \text{ cm}^{-1}$, where the BCB absorption is $\sim 6 \text{ cm}^{-1}$. The actual applications of the antenna can be found in Chapter 4 and Chapter 5. Only double metal processes will be treated in this section, although single plasmon waveguides can be adapted to

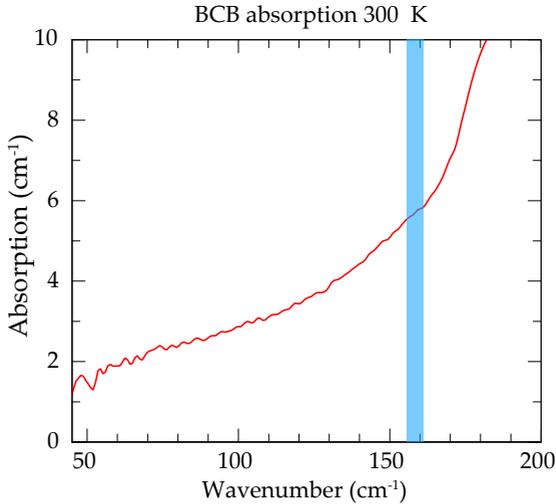


Figure 2.7: The absorption of BCB at 300 K. Although not optimal when above a wavenumber of 100 cm^{-1} , in this work the BCB has been used exclusively for a frequency of $\nu = 4.745 \text{ THz}$, corresponding to $\sim 158 \text{ cm}^{-1}$ (blue shaded region). Figure re-adapted from [59].

the process.

On the contrary to the standard double metal waveguide process, the BCB process presented in this thesis requires to dry etch the ridges¹ before the top metal deposition, as schematically illustrated in Fig. 2.8. After the dry etching of the ridges, the BCB is spun several times on the sample in order to completely cover the ridges (or mesas) with the polymer. Before each spinning step, the sample is treated with an O_2 plasma ashing in order to reduce superficial dirtiness that can be embedded into Benzocyclobutene at the next spinning. The step is run at 200 W for 2 minutes in 1 mbar of oxygen atmosphere. For the first BCB spinning, an

¹No wet etched BCB process has been performed in this thesis work, but wet etching is easily adaptable to the processing flow.

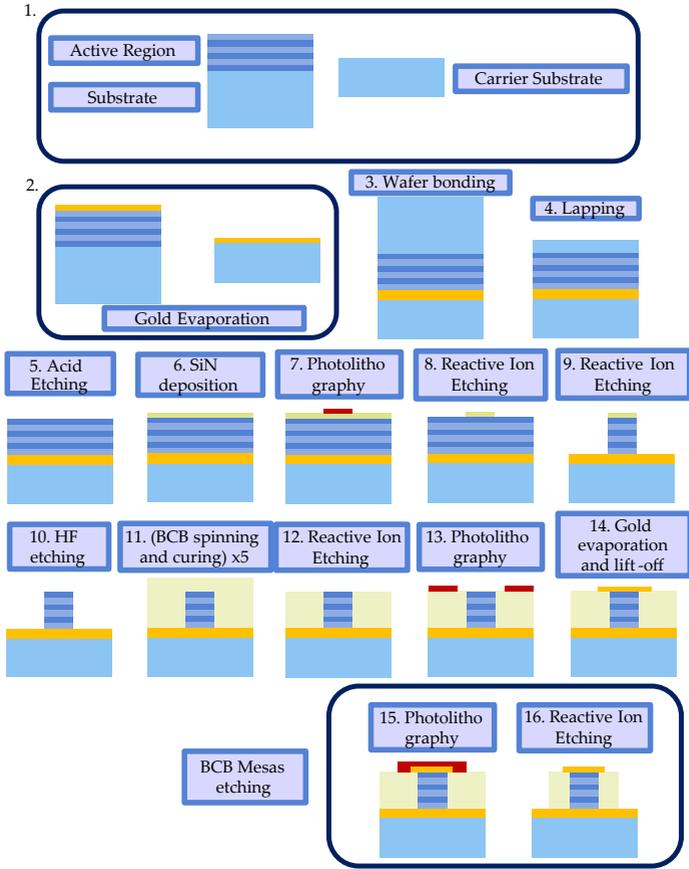


Figure 2.8: Schematic illustration of the BCB processing steps.

adhesion promoter is used (AP3000 spun for 30 seconds at 3000 rounds per minute (rpm)). Afterwards, a BCB spinning at 5000 rpm is alternated with a baking step in vacuum oven at 210 °C² in order to build up a thick layer of BCB. Each spin of Cyclotene 3022-57 has a thickness of $\sim 5.5 \mu\text{m}$, but the polymer thickness per spin can be as high as $7.0 \mu\text{m}$ when a pipette is used to collect the polymer from the bottom of the bottle, where the liquid is denser. Since the usual thickness of the active region is around $10 \mu\text{m}$, multiple spins are needed in order to embed completely the ridges (or mesas) in the polymer and keep the surface as flat as possible. After the last spinning step, the BCB is cured with a baking step that heats up the sample up to 250 °C. After being cured, BCB becomes extremely hard to remove selectively with chemical etching. Thus, a Reactive Ion Etching (RIE) step is necessary to remove it. The recipe details can be found in the Appendix. This step, called BCB *planarization*, is critical to obtain a good device yield. The goal of the step is to remove all the BCB that covers the top contact of the devices, to enable the eventual deposition of the metal that will work as a top metal cladding. At the end of the planarization step, the main possible outcomes are the following:

1. the BCB has been perfectly planarized, uncovering the top contact of the active region and having the same profile height of the ridges
2. the BCB is *over-etched*, i.e. the polymer is not only removed from the top contact of the device but also partially (or totally) removed from the side of the ridge. As a consequence, the height profile along the interface between the ridge and the BCB presents a step of several hundreds of nanometers

²recipe details can be found in the Appendix

3. the device is partially covered by BCB, leaving unexposed parts of the top contact
4. a mixture of the above-introduced outcomes, where some devices enters in the first category, some on the second and finally others in the third

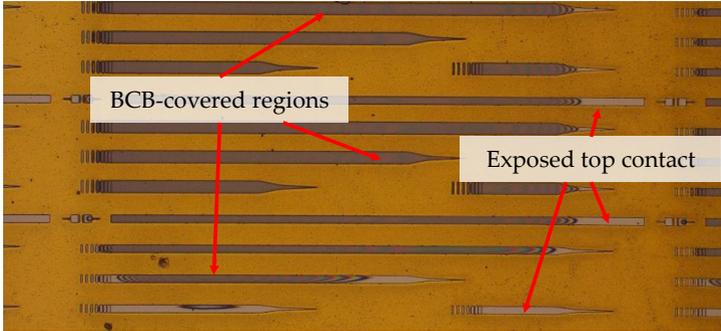


Figure 2.9: BCB planarization example. In the optical microscope picture, several ridges are visible and on some of them the top contact is starting to be exposed.

Among the aforementioned options, the most realistic outcome is the number 4. This scenario is extremely common since the BCB is never completely flat after a spin; due to its high viscosity and the inhomogeneity of the distribution of the ridges/mesas, ripples and small modulation of the height are formed on the surface of the spun polymer. Processing large samples ($> 15 \times 15 \text{ mm}^2$) bonded on even larger carrier substrates ($20 \times 20 \text{ mm}^2$) helps to have a flatter BCB spinning in the center because it reduces the influence in the central part of the sample of the so called edge bead effects, for which close to the edge of the sample the spun liquid is thicker.

After the planarization, the top contact can be deposited, involving a last photolithography, a deposition and a lift-off step. Eventually, the back of the sample is lapped down if a thinner

device is needed for better thermal dissipation properties before evaporating a back layer of Ti/Au which will be used for In/Au soldering on a Cu submount during the back-end fabrication.

2.3.1 Mask preparation

BCB is viscous and when spun it will be not flat if the sample has already been etched in mesas. Since this is the case for our project, the effect of viscosity must be considered when designing the mask. Structures with the maximum feature size below $\sim 20 \mu\text{m}$ are not an obstacle for the spinning of the BCB, which results overall flat. When bigger structures are etched a "compact" mask pattern is suggested in order to avoid excessive modulation of the BCB height between the etched structure. In particular, for the case of the laser cavity later presented in Chapter 4, the maximum feature size was 1 mm (laser cavity length) and the width approximately $50 \mu\text{m}$. Using a spacing between the cavities of $\sim 280 \mu\text{m}$, planarization of the BCB with a maximum overetching deviation from the top contact of the ridges of 500 nm has been possible. However, depending on the lasing wavelength and the application, optical cross-talking between the structure must be considered when reducing too much the distance between the ridges.

2.3.2 Making BCB mesas

For the purpose of making electrically floating devices, *i.e.* a device that presents a bottom contact which is not galvanically coupled to the copper submount, etching the BCB only in specific regions of the chip is needed in order to expose again the metal of the bottom cladding of the device and be able to wire bond it (step 15 and 16 of Fig.2.8). The RIE step for removing the BCB is extremely aggressive to any polymer, such that only metals have a selective

ratio higher than 1 [60,61]. However, using a metal as a hard mask actually involves a photolithography, an evaporation and a lift-off step in order to deposit and pattern it. After these steps, a selective etching for the deposited metal is needed in order to remove it after the exposed BCB has been etched. Moreover, the selective etching of the hard mask metal could harm the top metalization if it composed by a similar metal to the hard mask.

A better and safer solution can be the use of a thick photoresist mask [61]. As the photoresist is etched by O_2 at a rate comparable to the one of BCB, its minimum thickness is strictly equal to the thickness of BCB that must be removed. In this thesis, a negative photolithography mask is used with the photoresist AZ n-Lof 2070. The photoresist is spun at 1500 rpm for 60 seconds, in order to obtain a thick and homogeneous layer. After the spinning the sample underwent a soft bake at $110\text{ }^\circ\text{C}$ for 120 seconds and then exposed with 200 mJ/cm^2 . The hard bake has been done at $115\text{ }^\circ\text{C}$ for 90 seconds, followed by the development in AZ 726 mif for 120 seconds. The thickness of the photoresist after these steps is $\sim 10\text{ }\mu\text{m}$, allowing to etch BCB which is $\leq 10\text{ }\mu\text{m}$ thick. Thicker layers can be achieved with multiple spinning of photoresist or lower rpm.

The resist can be burned during the RIE step that is used to remove the exposed BCB. In this conditions, the photoresist can not be removed using Acetone or DMSO, even at temperature higher than room temperature. A solution to this problem is using a remover, Technistrip NI555, at $85\text{ }^\circ\text{C}$. The remover does not attack BCB nor the metal on top of it.

High Temperature THz QCLs

As introduced in Chapter 1, the widespread application of THz QCLs is strongly limited by its temperature performance. Indeed, discoveries and investigations on THz radiation are driving increasing interest in this field [2], but there is still a lack of efficient and easy to use THz sources. Specifically, the maximum temperature operation reached by the THz QCL is still below 200 K since 2012, when the world record of 199.5 K has been reached by Fatholouloumi et al. in a 3-well resonant phonon structure [24], and the technology still requires expensive cryogenics system to operate.

During this PhD work, we focused on 2-well designs whose aim was to improve further the maximum temperature performance of the THz QCLs. In the following sections, we will introduce a systematic study of several 2-well structure sequences and their performance dependencies on slight modifications of the QCL active region. The parameters characterizing a QCL structure are several; the number of quantum wells, the quantum well and barrier thicknesses, the barrier height and finally the doping position, width and dose. In this thesis work we investigate only on the variations of the quantum well and barrier thicknesses

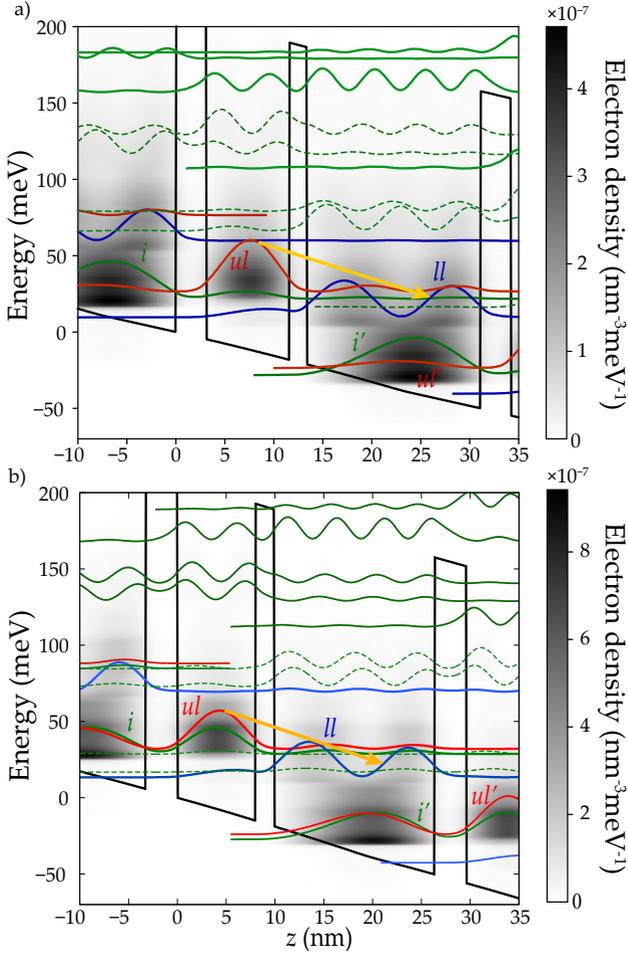


Figure 3.1: a) EV2416 and b) EV2624 band structures and respective electron densities simulated with a non-equilibrium Green's function model at maximum gain at 200 K lattice temperature. These two layers have reached high temperature operation and played a major role in the development of this work. The yellow arrow indicates the radiative transition, i is the injector level, ul the upper level state and ll the lower level state. The apex indicates that the level is relative to the following period of the structure.

and on the doping dose. Due to the reduced number of states and parameters of the 2-well design, each parameter variation has strong influence on the performance outcome. Experimental data will show that the structures are extremely sensitive even to small variations of the period thickness. A practical example of a simulated design is given in Fig.3.1 where the designs of EV2416 and EV2624 are shown. In both the designs we can distinguish the three most important energy levels: the injector level (i), the upper level state (ul) and the lower level state (ll). The electron passes from the injector level to the upper level state via resonant tunneling through the injector barrier. Once in the upper level the electron relaxes into the lower level state via diagonal transition, graphically represented by a yellow arrow, emitting a photon at the designed energy. Eventually, phonon scattering extracts the electron from the lower level state into the injector level of the next period, where the process repeats again.

The thickness of the injector barrier determines how likely is the resonant tunneling between the injector level and the upper state level to happen. A barrier too thick would hinder the electrons from populating the upper level state. However, a barrier too thin would lead to couple the injector level directly into the lower level state, introducing current leak and reducing the population inversion. On the other hand, the laser barrier, or coupling barrier, separates the upper level state from the lower level state. Its thickness determines the oscillator strength of the transition and this value must be optimized in order to avoid a too fast de-population of the upper level (barrier too thin) or a too weak coupling (barrier too thick). The optimization of the structure must be done with high accuracy and for this reason we employed Non-Equilibrium Green's Function (NEGF) models for all the band structure simulations [62, 63]. The simulations,

based also on in-house optimization algorithms, have been done in collaboration with Dr. Martin Franckíé.

Several layers have been grown for this study and a complete list can be found at the end of the Chapter. In the following sections we will introduce the layers that have played a more significant role for this investigation.

3.1 Barrier and doping study

The optimization performed with NEGF used the computed gain at room temperature as a merit function. Once a first structure with gain at room temperature has been simulated, a first optimization has been conducted on the doping level of the doped quantum well and on the injection barrier thickness. In particular, five structures have been grown. The first three designs have all the same layer sequence and varying doping density. These designs are namely EV2379 ($3.0 \times 10^{10} \text{ cm}^{-2}$), EV2413 ($2.25 \times 10^{10} \text{ cm}^{-2}$) and EV2414 ($4.5 \times 10^{10} \text{ cm}^{-2}$). The other two designs, namely EV2415 and EV2416, had the same doping density of $4.5 \times 10^{10} \text{ cm}^{-2}$ but different injection barrier width (37 and 31 Å respectively). The layers have been processed with a Au-Au wet etched process (see Appendix for details) and cleaved in 1 mm long devices, with width varying from 120 to 160 μm . They have then been measured in a homemade FTIR using a pre-calibrated Si-Bolometer as a detector. The maximum temperature of the devices versus the simulated gain is reported in Fig.3.2; the trend of the maximum temperature with respect to variation of the injector barrier thickness and doping dose agrees with what expected by the simulations. In particular, the sample EV2416 has shown the best performance, reaching a maximum operating temperature of 164 K.

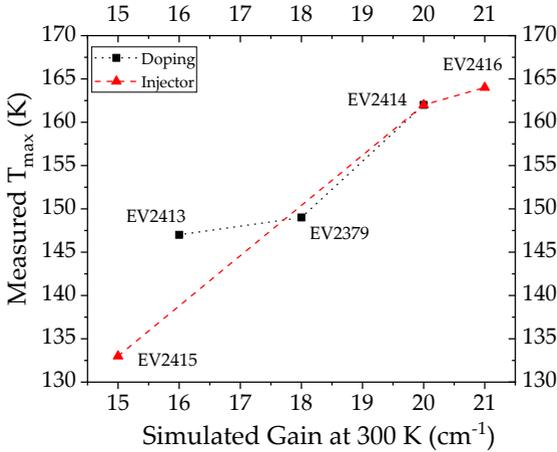


Figure 3.2: Maximum operating temperature versus the simulated gain at 300 K for several structures. EV2413, EV2379 and EV2414 have some layer sequence but different doping, while EV2415, EV2414 and EV2416 have same doping but different injector barrier thickness. Adapted from [29].

A Cu-Cu dry-etch process, as described in chapter 2¹, has been run on the layer that exhibited the best performance, EV2416. In Fig.3.3 the LIV, the spectrum and the T_0 fit of the best of ~ 20 measured devices are shown. Here, the laser is pumped using 50 ns pulses with a repetition rate of 415 Hz. The copper process improved the maximum temperature performance up to 193 K in pulsed mode. On the contrary, cleaving longer devices did not improve the temperature performance. We attributed the saturation of the maximum operating temperature as a function of length to the fact that the active region thickness is limited to 8 μm , suggesting that the waveguide losses are dominating over the

¹It must be noted that this process was also a preliminary test. Hence, the bonding and annealing have been executed at 400 °C, not at optimal temperature. Moreover, instead of 5 nm of Ta, a thicker layer of 10 nm has been used as diffusion barrier, thus increasing the waveguide losses of the cavity because of the higher losses of Ta with respect to Cu.

mirror losses [64].

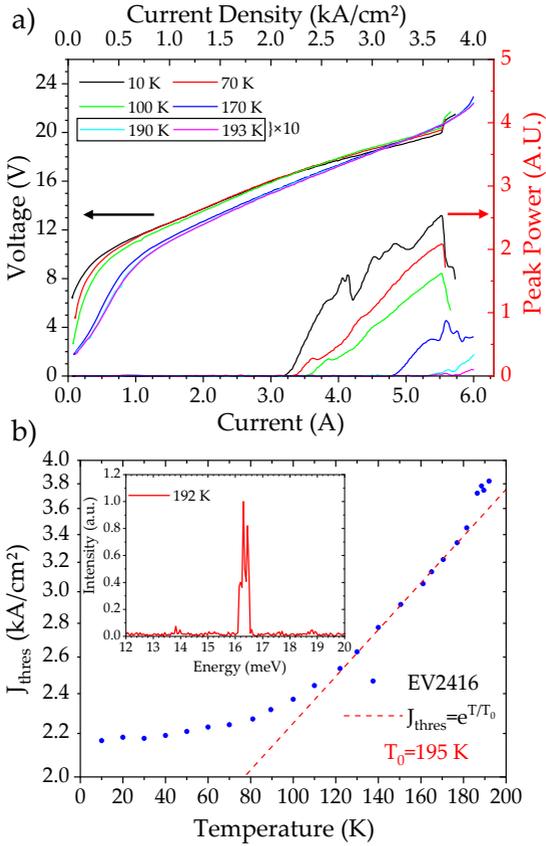


Figure 3.3: a) LIV curves vs T of EV2416. The maximum temperature measured was ~ 193.5 K. b) Threshold current density versus device temperature. In the inset, the spectrum of the laser at 192 K.

3.2 Radial position study

As suggested by the results previously presented, an extreme sensitivity of the temperature performance to small variations of the barriers has been observed. A more general dependence on the whole period thickness has also been observed on EV2416. For layers grown with the Molecular Beam Epitaxy (MBE), there is a gradient in period length along the radius with a variation up to -4% when moving from the center of the wafer to the edge, as schematized in color plot in Fig.3.4.a. Experimental data are reported overlapped to the schematic of the 3" wafer in the same figure. The nominal thickness t is grown in the center of the radius and it varies by $\Delta t \pm 2\%$ when moving to the center or to the edge of the wafer, respectively. From this specific layer, 6 chips have been processed. For each chip, the maximum recorded temperature in pulsed operation is reported in Fig.3.4.a. The chip surrounded by a solid line have been processed together and after the chips enclosed in a dashed line. Here, an increase of the maximum operating temperature of the devices can be seen when moving toward the edge of the wafer, *i.e.* toward a thinner layer. The slightly lower temperature performance of the most recent devices is caused by the appearance of temperature mismatch between the lower and the upper platen, as discussed in Chapter 2. The temperature mismatch caused the formation of a higher number of defects at the interface due to strain and hence higher optical losses in the Cu-Cu waveguides. The maximum temperature trend with respect to the period length is also reliably reproduced in the NEGF simulations. The color plot in Fig.3.4.b reports the maximum computed gain at 300 K of designs obtained varying both the barriers and wells thicknesses. The data are shown versus the variation of the wells width for which a trend can be identified. Indeed, the maximum expected gain is found when

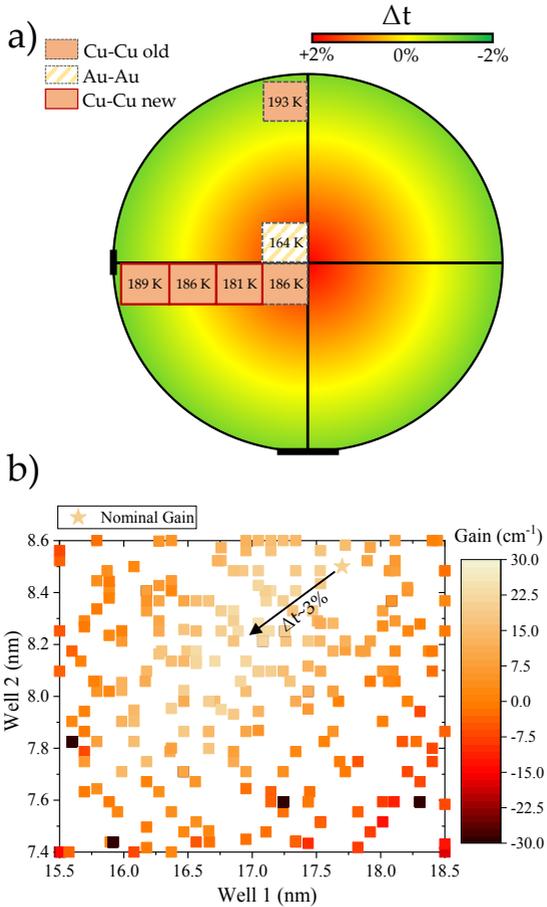


Figure 3.4: a) Maximum temperature data of EV2416 overlapped on a schematic illustration of the 3'' wafer with the thickness gradient reported. It is possible to see that for chips belonging to the same processing batch there is a correlation between maximum temperature and radial position. b) Maximum gain of the design of EV2416 for small variation of both barrier and well widths versus the well widths. The maximum gain is obtained for a structure which is $\sim 3\%$ thinner than the grown one.

varying homogeneously the quantum well thicknesses by $\Delta t - 3\%$ with respect to the nominal thickness represented by the star. The simulation results suggest that further temperature improvement could be achieved using a structure which is $\Delta t \sim -3\%$ thinner than the nominal design of EV2416.

3.3 Operation above 200 K

Following the results introduced in the previous section, a series of new layers have been grown, namely EV2622, EV2624, EV2626 and EV2628 which sequence can be found in Table 3.1 at the end of this Chapter. In particular, EV2624 is a new optimization of the design of EV2416 with a fine tuning of the well and barrier thicknesses. EV2628, instead, has the same layer sequence of EV2416 but it is grown with the nominal thickness placed in the center of the wafer. All of these layers were grown 12 μm thick in order to decrease the waveguide losses at the price of increased mirror losses caused by a decrease of reflectivity from $\sim 75\%$ to $\sim 65\%$ [64]. Lasers obtained from EV2624 and EV2628 lased above 200 K. Both layers have been processed from the center towards the edge of the wafer, in order to move again to thinner structures and to check the radial trend of the temperature of the devices. The layer EV2628 did not show the trend previously recorded for EV2416 and it presented, instead, a maximum operating temperature of 202.5 K for all the best devices, independently from the position. Statistically, considering devices of equal width (150 μm) but various length, 7 devices over 12 lased above 200 K. In contrast, EV2624 did show a radial position dependence like EV2416 and a wider statistics has been collected. Statistical results of the measured maximum temperature are summarized in Fig.3.5.a. The 3D histogram reports the maximum temperature of all the 23 tested lasers with a width of 150 μm and lengths between 1 and 2 mm with varying period thickness,

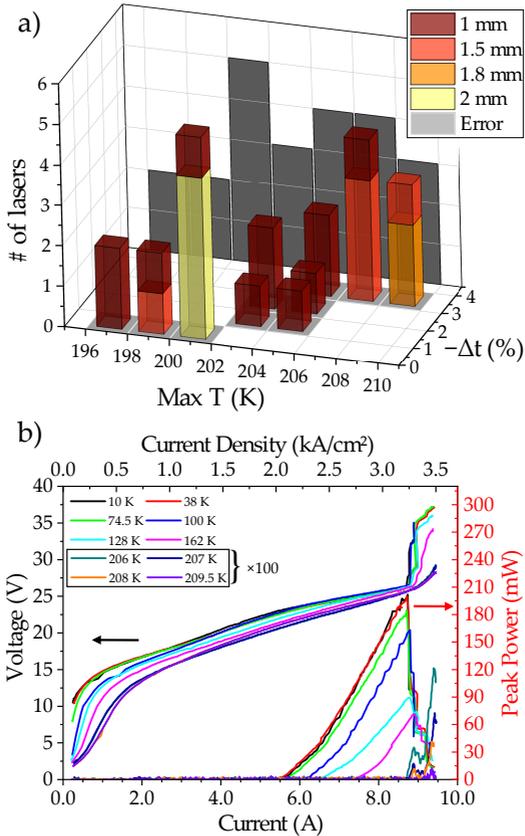


Figure 3.5: 3D histogram of the statistics collected over 23 lasers with a width of $150 \mu\text{m}$ and a length between 1 and 2 mm, as specified by the color scale, versus the layer Δt with respect to the central thickness. The projection in dark grey on the XY plane sums over all the thickness variation statistics. b) LIV characteristic of the best device. The laser has been pumped electrically with 50 ns width pulses at 415 Hz and operated up to ~ 210 K.

exploring ranges of $\pm 0.5\%$. As confirmed by the simulations, the maximum operating temperature (T_{\max}) improves when the period length is shortened. As reported before, for 8 μm thick layers no temperature improvement has ever been observed for longer devices. For a 12 μm thick waveguide, instead, the reduction of the waveguide losses and the increase of the mirror ones led to a different trend; longer devices usually outperform shorter ones. The best device, found for $\Delta t \approx -3.5\%$, was 1.8 mm long and lased up to a maximum temperature of ~ 210 K, as shown in Fig.3.5.b. The device showed a peak power of 200 mW between 10 K and 40 K, and a notable peak power of 1.2 mW at 206 K, close to the maximum operation temperature. With an applied bias of 25 V and an injected current of 9 A, the laser shows a wallplug efficiency of $\sim 0.1\%$, in line with typical values for Fabry Perot double metal structures. Longer devices could not be cleaved from this chip due to limitation of the setup on the maximum current of the injected pulse.

3.4 Thermoelectrically cooled THz Quantum Cascade Laser

The biggest practical limit to the application of a THz QCL is the use of cryogenics to cool down the device. Using a flow cryostat takes space and it requires a continuous source of Helium, which is expensive on the long run. A better solution is the use of Stirling coolers, but this technology presents usually high consumption power (> 150 W) and they are expensive with prices ranging from 1000 to 10000 \$. For this purpose, an important step in the development of the THz QCL is to be able to cool down and operate these devices employing cheap and easy-to-use Thermoelectric Cooler (TEC). Using the laser introduced in the previous section and high-performance TEC, we operate for the

first time a THz QCL in a cryogenics free system.

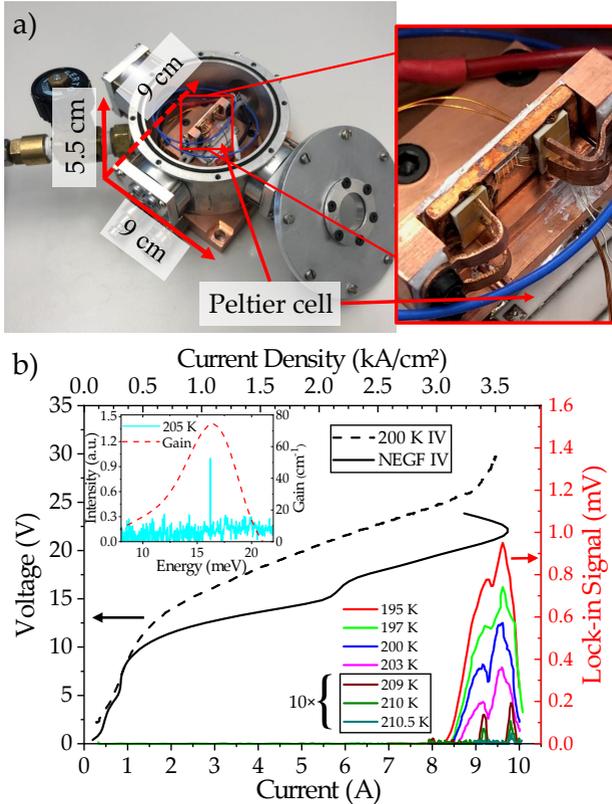


Figure 3.6: a) The laser box with Peltier cell and mounted QCL. The box footprint ($\sim 9 \times 9 \times 5.5 \text{ cm}^3$) is significantly reduced compared to a flow cryostat (even without taking into account the He dewar). At maximum capacity, the Peltier cell uses $\lesssim 30 \text{ W}$ to cool the laser down to 195 K. b) LI curves obtained cooling down the laser in the laser box and detecting it using a He-cooled Ge bolometer. In dashed and solid black lines, a comparison between the measured IV and the simulated IV at a lattice temperature of 200 K is shown. The IV has been measured in a flow cryostat setup. In the inset, it is possible to see that the emitted frequency at 205 K fits the simulation prediction of the gain.

In order to cool down the laser we employed the 4-stage TEC from II-VI Marlow Industries, model SP2394, with a maximum

$\Delta T = 130$ °C and a maximum power consumption of $\lesssim 30$ W (characteristic curves shown in Appendix). The laser box prototype is shown in Fig.3.6.a. The box has a footprint limited to $\sim 9 \times 9 \times 5.5$ cm³, definitely smaller than a standard flow cryostat. The hot side of the thermoelectric cooler is in thermal contact with flowing water at 17 °C. The laser is connected with only one wire, in order to minimize the thermal load on the cold side of the Peltier cell. As a consequence, the voltage drop across the laser could not be measured during operation with the TEC. Two M3 plastic screws pressing on the laser holder are used to clamp the TEC on the heat sink, in order to have a good thermal contact. At the same time, the polymer material of the screws assures a low thermal conductivity and hence a small heat load on the cold side of the TEC. Thermal contact has been improved using thin layers of Arctic silver thermal paste (heat conductivity $q = 8.50$ W/(K·cm)). The thermal load computed considering only the screws and wires contribution is ~ 130 mW (see Appendix for more details). Temperature has been measured using a 1 kOhm NTC thermistor (44000RC series from TE connectivity) with a two-wires sensing technique.

Under vacuum ($\lesssim 10^{-4}$ mbar), the laser has been cooled down to ~ 195 K and operated. In Fig.3.6.a, the LI curves of the laser operated in the laser box are shown. The THz radiation has been detected using a He-cooled Ge bolometer, collecting the light coming from the laser with an elliptical mirror. The laser was electrically pumped with 50 ns current pulses at 380 Hz. The maximum operating temperature measured with the thermistor has been $T_{\max} = 210.5$ K, confirming the results already acquired with the flow cryostat within an error of 1 K. Moreover, as visible in Fig.3.7.a, J_{thres} data acquired during operation with the laser box shows consistency with data collected in the flow cryostat. A

fit of T_0 based on the formula $J_{\text{thres}} = J_0 \exp(T/T_0)$ gives a value of 229 K.

The relatively high peak power of the device even at high temperatures actually allowed to acquire spectra using a commercial room temperature (RT) DTGS detector provided in a Bruker Vertex 80. In Fig.3.7.b, the acquired spectra of the device at different laser temperatures are shown. Laser was operated at maximum power and the signal was integrated for 10 minutes with a resolution of 0.2 cm^{-1} . With the integration times that were chosen, the intensity peak has been resolved up to 207 K, although longer integration times could have been used in order to acquire the spectrum at even higher temperature. The acquisition of the signal using a RT detector is the first demonstration of a cryogenic-free source and detector system involving the use of a THz QCL.

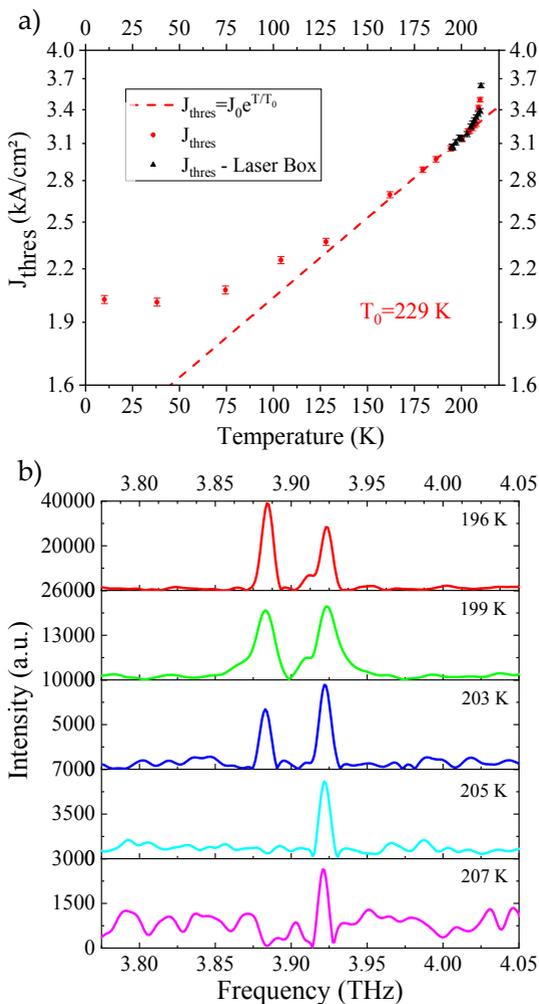


Figure 3.7: a) T_0 fit of the threshold current density J_{thres} reported on a log scale. The threshold current density versus temperature data is fitted with an exponential dependence on data points collected in cryostat operation (red circles), but agrees well with the data collected during the thermoelectric cooling operation (black triangles). A $T_0 = 229$ K is obtained. b) Spectra taken with the laser cooled down using a thermoelectric multistage cooler and using the DTGS room temperature detector of a Bruker Vertex 80 FTIR. Laser has been operated at maximum power.

3.5 Conclusions

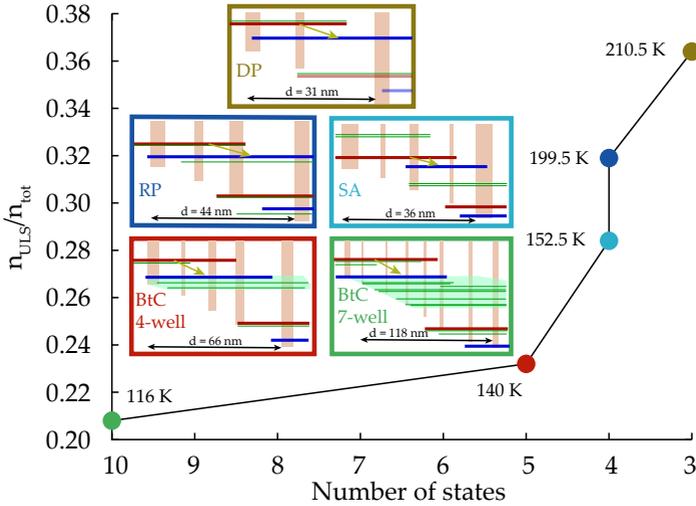


Figure 3.8: Relative density of the upper laser state (n_{ULS}) calculated with a nonequilibrium Green's function (NEGF) model for five THz quantum cascade laser designs with different number of active states per period. Schematics of the simulated QCLs are shown in the five insets and represent direct phonon (DP), resonant phonon [24] (RP), scattering-assisted (SA) injection [65], 4-well [18] and 7-well [17] bound-to-continuum (BtC) designs. The DP QCL is the layer EV2624 presented in this Chapter. For each design we show the upper laser state (ULS) in red, the lower laser state (LLS) in blue, and green lines indicate the other relevant states. The vertical bars show the barriers separating the quantum wells. Image and contained data are gentle concession of Dr. Martin Franckić.

In this Chapter we have introduced a 2-well design optimized using a NEGF model and we have shown the reliability of this design tool in predicting qualitatively the collected experimental data. The results here shown are a consistent improvement in the maximum temperature performance since the outstanding work of Fatholouloumi presented in [24]. The better temperature performance of the 2-well with respect to the other possible designs can be explained with a simple argument. The small

number of states of the 2-well together with a proper optimization of the design can achieve a high ratio of upper laser state (ULS) electron population with respect to the total population. This simple ratio can be taken as parameter for measuring the "goodness" of a design as a higher ratio corresponds to a smaller number of free electrons, key source of re-absorption and optical losses [66]. The improvement in the temperature performance can indeed be correlated to the population of the ULS as depicted in Fig.3.8. Here, the relative density of the ULS for five different structures is computed with NEGF simulations. The structures taken into consideration, shown in the inset, are the direct phonon (DP) [28,39], resonant phonon [23,24] (RP), scattering-assisted (SA) injection [25,65], 4-well [18] and 7-well [17] bound-to-continuum (BtC) designs. The plot shows that decreasing the number of states of the design increases both the electron population of the ULS and the maximum temperature of the laser based on that specific design.

Further optimization of the 2-well design using the NEGF models as well as the improvement of the yet not perfect Cu-Cu process employed in this work will surely bring to further improving the temperature performance. For AlGaAs/GaAs THz QCL this probably represents the best path to follow in order to get closer to the coveted room temperature performance as well as to increase the extracted power at high temperature. It must also be noted that, even if the high dissipated power of the presented device will hinder higher duty cycle operation, the peak power of 1.2 mW at 206 K is probably enough to achieve self mixing imaging in a THz QCL [45].

3.6 Processed samples

For the realization of this work, 24 layers have been grown and tested. The majority of these layers has shown lasing operation, demonstrating the soundness of NEGF as a QCL design tool. In the following two tables 3.1 and 3.2, a summary of all the grown and processed 2 quantum wells layers is given.

Layer	Layer sequence	Intended Doping [cm^{-2}]	Measured Doping [cm^{-3}]	J_{max} [kA/cm^2]
EV2378	<u>18/87/30/60/34/85</u>	5.07e16	6.35e15	~ 0.7
EV2379	<u>18/87/30/60/34/85</u>	1.01e17	1.70e16	~ 3.1
EV2413	<u>18/87/30/60/34/85</u>	1.71e17	1.44e16	~ 1.9
EV2414	<u>18/87/30/60/34/85</u>	3.43e17	1.45e16	~ 2.4
EV2415	<u>18/87/30/60/37/85</u>	3.43e17	1.70e16	
EV2416	<u>18/87/30/60/31/85</u>	3.43e17	1.80e16	~ 3.7
EV2417	<u>21/87/30/60/34/85</u>	3.43e17	4.44e16	~ 2.9
EV2418	<u>16/87/30/60/34/85</u>	3.43e17	5.50e16	
EV2420	<u>16/87/30/60/34/85</u>	3.43e17	4.60e16	
EV2421	<u>16/87/30/60/34/85</u>	2.57e17	2.30e16	
EV2455	<u>18/136/30/11/31/85</u>	3.43e17	2.90e16	
EV2457	<u>18/96/0/81/31/85</u>	1.03e11	2.90e16	
EV2470	<u>18/96/0/81/31/85</u>	5.97e10	N.M.	
EV2473	<u>18/96/0/81/31/85</u>	2.99e10	N.M.	
EV2506	<u>18/87/30/60/31/85</u>	2.08e17	1.79e16	~ 2.0
EV2508	<u>18/87/30/60/31/85</u>	1.45e17	8.70e15	~ 1.4
EV2532	<u>18/87/30/60/31/85</u>	2.08e17	1.89e16	
EV2539	<u>18/87/30/60/31/85</u>	2.08e17	1.63e16	~ 3.5
EV2587	<u>18/87/30/60/31/85</u>	2.08e17	N.M.	~ 3.6
EV2610	<u>18/87/30/60/31/85</u>	1.66e17	N.M.	~ 1.6
EV2622	<u>18/87/30/60/31/85</u>	1.92e17	1.76e16	~ 3.2
EV2624	<u>19.7/87/30/53.5/33.8/82.8</u>	1.92e17	1.92e16	~ 3.2
EV2626	<u>18/87/30/60/31/85</u>	1.31e17	1.57e16	~ 3.2
EV2628	<u>18/87/30/60/31/85</u>	1.92e17	1.90e16	~ 3.0

Table 3.1: Summary of all the 2QW layers tested and the comments on the peculiarities and/or performances of these layers. In the layer sequence, the italic refers to the wells, the bold to the barrier and the underlined numbers are doped.

Layer	Pr.	Max T. (K) [Cu]	Comments
EV2378	1	NL	
EV2379	2	149 [172.5]	wet-etched Cu process
EV2413	1	147	
EV2414	1	162	pre-bonded Cu sample never processed
EV2415	1	133	
EV2416	6	164 [194]	Cu
EV2417	1	134	
EV2418	1	NL	used as dummy sample for etching tests
EV2420	1	115	33.5% Al barriers
EV2421	1	142 [147]	wet-etched Cu process
EV2455	1		shifted doping with no rotation
EV2457	7		delta doping with no rotation
EV2470	2		less doped version of EV2457
EV2473	2		less doped version of EV2470 and double thickness
EV2506	1	144	redo of EV2416
EV2508	1	120	redo of EV2416 with less doping
EV2532	NP	NL	Double thickness of EV2416 but Al cell broke the last 4 μm growth
EV2539	1	122	Retry of EV2532 but the new Al cell introduced a positive background doping
EV2570	1	NL	it is EV2532 etched down by 4 μm with regrown contact and processed
EV2587	4	[165]	used for top contact testing (see Appendix)
EV2610	4	147	used for top contact testing (see Appendix)
EV2622	1	[155]	redo of EV2416, 12 μm thick
EV2624	4	[210]	New optimization, 12 μm thick
EV2626	1	[153]	redo of EV2622, special wafer orientation
EV2628	4	[202.5]	redo of EV2622

Table 3.2: Summary of all the 2QW layers tested and the comments on the peculiarity and/or performances of these layers. The number or processes (Pr.) executed on the given layer is specified and the maximum temperature in square bracket refers to Cu-Cu double metal processes.

4.745 THz Local Oscillator for Radioastronomy

In this chapter we will discuss a scientific application of a THz QCL for astrophysical measurements. As introduced in Chapter 1, many roto-vibrational transitions and atomic cooling lines can be found in the THz frequency spectrum. For some of these transitions, THz radiation is extremely important in astrophysics, because spectroscopy in this frequency range can give information about large interstellar clouds and their evolution [67,68].

4.1 Heterodyne Measurement Principle

However, detection of THz radiation coming from the outer space is arduous and it can be done only using heterodyne measurement because of the low intensity nature of the signal collected [69]. The principle is relatively easy; in a non-linear medium the incoming (weak) signal of amplitude E_s and frequency ω_s is coupled with a pump signal coming from a Local Oscillator (LO) and with amplitude $E_{LO} \gg E_s$ and frequency ω_{LO} . Due to non-linear

mixing the out-coming signal intensity I_{out} can be written as

$$I_{\text{out}} \propto \frac{1}{2}E_s^2 + \frac{1}{2}E_{\text{LO}}^2 + 2E_sE_{\text{LO}} \cos(\omega_s t + \varphi) \cos(\omega_{\text{LO}} t) \quad (4.1)$$

where φ is an arbitrary phase and t is the time variable. Filtering out the two DC component of the intensity, the signal shows a mixed term E_sE_{LO} which oscillates in time and creates the sum and difference frequency waves which depends on both the pump and the signal amplitude, resulting in an enhancement of the signal. Moreover, if $\omega_{\text{LO}} \approx \omega_s$, the difference frequency term is a slow radiofrequency signal, which intensity is proportional to E_{LO} , that can be acquired and processed in an easier way than a THz radiation.

4.2 SOFIA: The Stratospheric Observatory For Infrared Astronomy

The obstacles for successfully performing an heterodyne measurement in the THz range are many-fold, but among these there are two which matters the most for the purpose of this thesis:

- avoiding the atmosphere absorption of THz radiation to reduce attenuation of the collected signal
- providing a reliable local oscillator, *i.e.* a coherent THz source which emits enough power to pump the mixers¹

The first problem arises from a high absorption due to the water molecules present in Earth atmosphere. Fig.4.1 shows that even when the absorption spectrum is taken at a relatively high altitude (Chajnantor is ~ 5 km above mean sea level (AMSL)) the THz transmission between 1 and 5 THz (50 – 300 μm) is negligible.

¹For the setup that will be introduced the mixers are provided by the Physics Institute of Köln University [70,71]

THz transmission increases only starting from the beginning of the Earth stratosphere (~ 13 km AMSL), where it becomes possible to detect an incoming THz signal from the outer space.

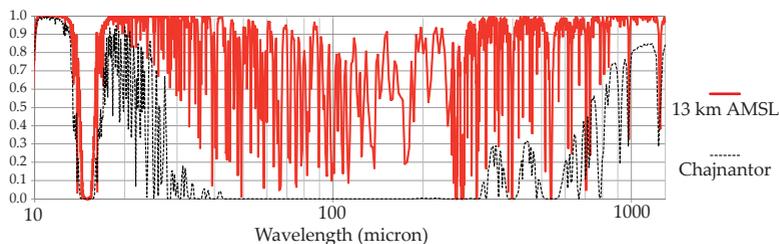


Figure 4.1: Atmospheric absorption at two different altitudes; Chajnantor observatories (placed at 5 km AMSL) and at 13 km AMSL. As it can be seen no THz radiation is detectable even at relatively high altitudes, forcing the scientists to find alternative solutions to the common observatories. Figure adapted from [10].

A possible solution to this issue is the deployment of a satellite orbiting around Earth and equipped with the necessary technology to perform a THz detection. Albeit expensive, it would be indeed enough to deploy a “THz telescope”, in the similar fashion of Hubble space telescope for optical radiation, to overcome this challenge. This has actually been done with the deployment of the Herschel telescope in 2009, but the telescope stopped working in 2013, when the 2300 liters of liquid helium run out and the setup could not be operated anymore [72]. The maintenance and upgrading of a technology which gets “segregated” to fly several hundreds of kilometers above Earth is an expensive task and a more flexible alternative was needed. The astrophysicist community, mostly led by the National Aeronautics and Space Administration (NASA) and the *Deutsches Zentrum für Luft- und Raumfahrt e.V.* (DLR), has discussed at length and found a solution in a project that took more than 10 years of work to start: the Stratospheric Observatory For Infrared Astronomy (SOFIA) [73].

SOFIA is a Boeing 747SP (Special Performance) with a modified fuselage able to host a 2.5 m telescope (see Fig.4.2). The choice of a Boeing 747SP is justified by the shorter length compared to a standard Boeing 747, which makes SOFIA able to fly for a longer time up to ~ 13.7 km AMSL, enough to sufficiently reduce atmospheric absorption in the THz range according also to Fig.4.1. This solution has allowed a degree of flexibility to the experiment which is totally lacking on a satellite; at the end of each measurement flight, SOFIA comes back to the hangar, where it is possible to exchange the setup attached to the telescope in order to investigate on another THz frequency range.



Figure 4.2: SOFIA with the open fuselage in order to expose the telescope and test it in a pre-flight on-ground test. Personal picture.

4.3 A local oscillator for SOFIA

As a consequence of its flexibility, SOFIA instruments pool is not limited to one single setup and each experiment has a certain frequency range that can be investigated, often changing accordingly both local oscillator and detector [75]. Among the

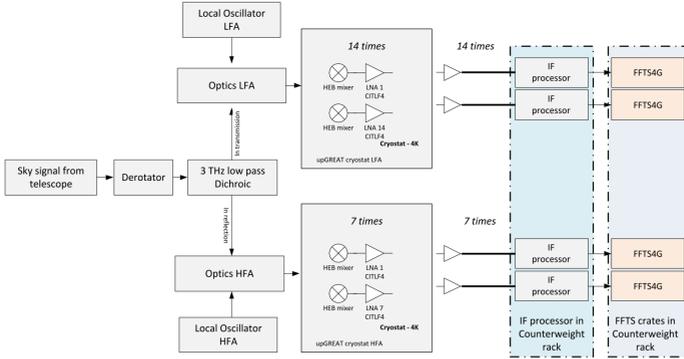


Figure 4.3: upGREAT setup schematics. Illustration adapted from [74].

different projects², we strictly collaborated with the German REceiver At THz frequency (GREAT) [76], recently upgraded to upGREAT [74]. Goal of the experiment is to measure and quantify the amount of Carbon and Oxygen atoms in specific nebulae through the measurement of [CII] and [OI] cooling lines, respectively. These two transitions are placed in the THz region, specifically at ~ 1.9 THz and at ~ 4.745 THz. During this PhD work we have focused good part of the efforts in developing a reliable LO source which could be used for a heterodyne measurement at 4.745 THz. The requirements for such a LO must satisfies several conditions which are imposed by the limitations of the experimental setup that SOFIA can mount during the flight. Thus, the ideal SOFIA's LO candidate must satisfy the following conditions

1. it must be single mode at 4.745 THz, in order to be used for a heterodyne measurement
2. it must be tunable in frequency by at least ± 2 GHz in order to extract information about the speed of the observed

²A list of the several instruments that can be mounted on SOFIA is given in [75]

interstellar cloud (through Doppler effect)

3. emitted power must be above 1 mW in continuous wave operation, in order to pump properly each mixer (up to 7 pixel for the 4.745 THz channel) and be able to boost the signal enough to be processed and measured
4. the emitted beam pattern of the LO must have a Gaussian shape so to optimize the coupling to the detector's pixels, which are provided with a horn antenna for the radiation collection
5. the dissipated power must be relatively low, as the performance of the Stirling cryocooler used to cool down can assure temperatures lower than 50 K, with a minimum limit of ~ 40 K, only when the thermal load is lower than 5 W. This requirement represents a challenge depending on the laser, since above 50 K emitted power could be not enough to pump the mixers.

4.4 Cavity Design

In the past, different and successful approaches to achieve a THz quantum cascade laser that would satisfy the requirements above were developed [5,78]. Among these, the more notable are cavity designs based on a first order Distributed-Feedback (DFB) lasers or a third order one. In the first case, the laser waveguide is single plasmon, which schematic has been introduced at the beginning of Chapter 2. This configuration increases the mirror losses in favor of more emitted power. Moreover, the laser has a far field pattern that diverges less than in a double metal configuration and it can be corrected through the use of lenses and mirrors in order to make it Gaussian-like. This laser has shown an emitted power of 150 μ W with a tuning of +2 to -4 GHz across the

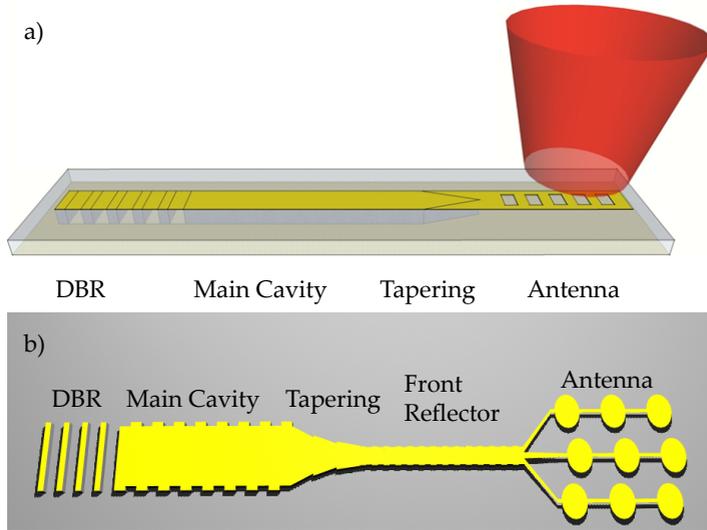


Figure 4.4: a) Design of the prototype of a laser with an integrated slot array antenna. Adapted from [77]. b) A not in scale illustration of the laser cavity design. Five sections compose the whole cavity. Starting from the left to the right: 1) the DBR, 2) the main cavity with a second order lateral grating, 3) a multisection tapering, 4) a front reflector based on a first order lateral grating and 5) an outcoupling patch antenna array. Adapted from [57]

target frequency. The latter approach, instead, exploited a Au-Au double metal waveguide, which has the advantage of improving thermal dissipation and it usually performs better in temperature than the single plasmon [31]. The extracted power was several hundreds of μW but the far-field pattern was sub-optimal with an elongated shape that limited the optical power coupling to the mixers [79, 80]. However, the increasing demand of power due to the increased number of detector pixels required to achieve better performances. The 4.745 THz solution here presented is based on the successful application of a Benzocyclobutene (BCB) process on the development of a 1.9 THz local oscillator [56] and on preliminary studies on the electromagnetic wave engineering

in cavities with integrated patch and slot array antennas [77], for which a design example is shown in Fig.4.4.a. As illustrated in Fig.4.4.b, the specific cavity design is composed by five different parts (following the figure from left to right):

1. a DBR which acts as a high reflective mirror placed on the back of the cavity
2. a second order lateral grating is the main feature of the amplification section. The lateral grating increases the radiative losses of the higher order transversal modes, favoring the lasing of only the fundamental one
3. a multisection tapering filters further the fundamental transversal mode and couple the wave to the front mirror
4. a first order DFB acts as the front mirror. Due to the shallow refractive index contrast the reflectivity band is narrow, selecting the longitudinal lasing mode
5. a patch array antenna for surface outcoupling.

The antenna is embedded in the top metal cladding of the laser cavity, and it lies on top of BCB, which is previously spun and planarized around the laser cavity, as explained in Chapter 2. The following sections are meant to report the details of the laser cavity that has been simulated using the computational methods that will be introduced when needed.

4.4.1 Back reflector: DBR

Since the electromagnetic wave must be out-coupled through the patch-array antenna, the back reflector is designed to have a high reflectivity for a wide frequency band. The designed DBR is based on a repetition of two alternated layers of BCB ($n_{\text{BCB}} = 1.55$) and GaAs ($n_{\text{GaAs}} = 3.72$). The single layer length depends on the

Bragg's wavelength λ_B , which is at the center of the reflected band, and it is fixed to a length d such that it satisfies the following relationship:

$$d = \frac{\lambda_B}{4n_{\text{eff}}} \quad (4.2)$$

where n_{eff} is the effective refractive index in the medium of the layer. Selecting the lengths $d_{\text{BCB}} = 4.334 \mu\text{m}$ and $d_{\text{GaAs}} = 10.290 \mu\text{m}$ respectively for the BCB and the GaAs layers, the reflectivity reported in Fig.4.5.a has been simulated for a 4 period DBR.

Computation of the DBR reflectivity

The simulation of the DBR reflectivity has been done using CST Microwave Studio, a finite element method (FEM) software for 3D electromagnetic wave simulations. The small number of periods (4) as well as the reduced size of the structure allows to use 3D simulation for the computation of the reflectivity maintaining the simulation time relatively low.

4.4.2 Amplification section: second order DFB

The laser must emit a relative high power ($> 1 \text{ mW}$) and operate in single mode over the whole dynamical range in order to exploit to the maximum the frequency tuning due to Stark shift [81]. These two conditions compete with each other. Indeed, the first requirement can be satisfied with a wider main cavity, but this would allow the amplification and oscillation of higher order transversal modes – thus multi-mode emission – as soon as the cavity is as wide as roughly the wavelength of the electromagnetic wave in the medium. In order to circumvent this problem, we have added a second order lateral grating to the waveguide. The grating perturbs the modes, increasing the losses of all the modes due to lateral radiative extraction. As the fundamental mode is more

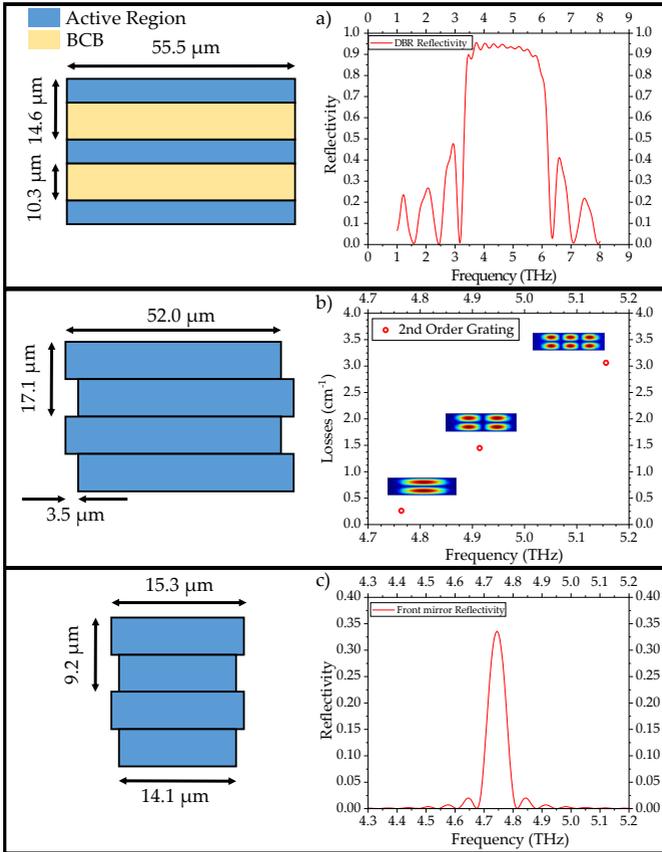


Figure 4.5: a) On the left, the schematic of the DBR period, which works as a broadband back reflector mirror. On the right, the simulated reflectivity of the DBR section, with a maximum value higher than 90% for the target frequency band. b) On the left, the schematic of the second order grating section, which introduces losses to the higher order lateral modes. On the right, the simulated losses versus the frequency are plotted. Next to each point the simulated electric field distribution shows that for higher order lateral modes the losses increase. c) On the left, the schematic of the first order grating section, which works as a narrowband front reflector for the selection of only one longitudinal mode. On the right, the simulated reflectivity of the section, with a half width half maximum of ~ 35 GHz.

confined inside the cavity and it has a lower overlap factor with the sidewalls of the waveguide, it interacts less with the grating, reporting a smaller loss compared to the higher order transversal modes. In Fig.4.5.b we report the details of the second order grating. On the left, the schematic of the second order grating period. The grating consists of a lateral corrugation on both sides of a $52.0\ \mu\text{m}$ wide cavity. The period of the grating is $17.0\ \mu\text{m}$ with a 50% duty cycle and the corrugations on the two sides of the waveguide have the same phase. On the right hand of Fig.4.5.b, the results of a simulation conducted on a waveguide composed by 10 of these periods. The figure shows that the losses of the higher order transversal mode are sensibly higher than the fundamental one. This assure that the transversal fundamental mode will have more gain and it will be more likely to achieve lasing threshold than the other modes.

Computation of the second order grating

For the simulation of the second order grating two models have been used: a 3D simulation with periodic boundaries for the computation of the eigenmodes of the second order DFB and another 3D simulation for the estimation of the losses induced by the corrugation. Both of these simulations have been done using COMSOL. The simulation of the eigenmodes has been run on a single period of the grating, imposing a periodic boundary conditions on the structure faces where the period is repeated, as shown in Fig.4.6.b. An eigenmode study has been done in these conditions, sweeping over the period length until the fundamental lateral mode has been found at the target frequency (4.745 THz). In the losses simulations, the structure is simulated with 10 periods, removing the boundary conditions and creating a finite cavity with a second order lateral grating. The software automatically

computes for an arbitrary number of modes the Q factor, which is inversely proportionally to the losses. The optimal value for the lateral grating depth can be found sweeping over it in order to increase the losses of the higher order lateral mode without perturbing the fundamental one.

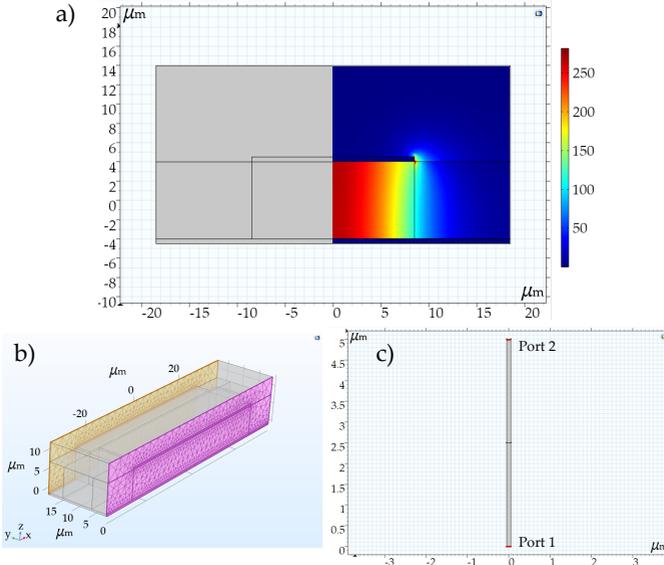


Figure 4.6: Examples of structures simulated with COMSOL Multiphysics. a) The n_{eff} estimation of the mode is done via 2D simulation. In color scale the electric field distribution of the fundamental TM mode is shown. b) 3D simulations have been used mainly for periodic structure. In the example the periodic boundaries of the second order lateral grating are highlighted. c) Quasi-1D simulation example of a single period of the front mirror. The gray rectangles are front mirror sections with different n_{eff} . The system is provided with two ports, but only one is excited with an electromagnetic wave at an arbitrary frequency.

4.4.3 Front reflector: first order DBR

Despite the presence of the second order lateral grating on the main cavity, the longitudinal modes, or Fabry-Perot modes, can still be all amplified by the cavity leading to multi-mode emission. These modes are inversely dependent on the length of the cavity and they are spaced by the *free spectral range* $\delta\nu_{FSR} = \frac{c}{2n_g L}$ where n_g is the group index of the medium, L the cavity length and c the velocity of light in vacuum. As a consequence, the longer the device the denser the spectrum of longitudinal modes. As in the case of the lateral modes, there is again a trade off: in order to extract more power, a longer main cavity would allow a higher power generation, but the longitudinal mode would be closer in frequency due to a decrease of $\delta\nu_{FSR}$ and more modes could be within the reflection bandwidth of the cavity. A solution to this problem is represented by using a narrow band mirror that decreases the mirror losses α_m only for a specific frequency mode. The mirror is composed by a shallow first order lateral grating so to have a small refractive index contrast Δn_{eff} and consequently a small bandwidth $\Delta\nu$ of the mirror, expressed by the relationship

$$\frac{\Delta\nu}{\nu_B} \propto \arcsin\left(\frac{n_{\text{eff}1} - n_{\text{eff}2}}{n_{\text{eff}1} + n_{\text{eff}2}}\right) \quad (4.3)$$

where ν_B is the frequency associated to the Bragg's wavelength λ_B for which $n_{\text{eff}1}$ and $n_{\text{eff}2}$ are the effective refractive indexes of the medium. The reflectivity of the mirror and the refractive index contrast are tightly connected by the coupling coefficient κ of the 1D photonic crystal by the relationship

$$|\kappa| = \frac{\pi\Delta n_{\text{eff}}}{\lambda_B} \quad (4.4)$$

When propagating along the 1D photonic crystal, the wave gets reflected back at a spatial rate quantified by κ . The lower κ is the narrower is the gap and thus the reflectivity bandwidth, but

also the reflectivity of the front mirror decreases, leading to an increase of the mirror losses. Increasing the number of periods increases the reflectivity again but reduces $\delta\nu_{FSR}$. Therefore, the trade off mentioned above can be reformulated in function of κ . Indeed, the value $L_m = 1/\kappa = \lambda_B/(\pi\Delta n_{\text{eff}})$, quantifies the distance that an electromagnetic wave, which frequency is centered in the bandgap, can travel inside the 1D photonics crystal mirror before its amplitude is reduced by a factor e . Thus, in order to have the longest possible cavity one has to decrease as much as possible the refractive index contrast Δn in order to have a band narrow enough to filter the unwanted longitudinal modes. Considering technological limits, in order to keep using standard photolithography, we decided to keep a Δn such that the size of the lateral corrugation is $\sim 1 \mu\text{m}$. In Fig.4.5.c, the simulated reflectivity of a mirror composed by 70 periods is shown. The single period is long $9.2 \mu\text{m}$ and equally divided between a section $15.3 \mu\text{m}$ wide and a section $14.1 \mu\text{m}$ wide. The half width half maximum of the mirror is 35 GHz.

Computation of the front mirror

The front mirror simulation consists of three different steps:

1. a 3D simulation with periodic boundary – similar to the one done for the amplification section – computes the eigenmodes of the first order lateral grating
2. a 2D simulation computes the effective mode index n_{eff_1} and n_{eff_2} of the two regions of different width composing the 3D model just computed (Fig.4.6.a)
3. a quasi-1D simulation is used to compute the reflectivity of several periods of the first order grating.

The 3D simulation is used to compute the band-edge eigenmodes

and a sweep in period length is used to adapt the structure to the target frequency, although this time the wanted frequency will be centered between the two band edge modes of the front DBR, where the reflectivity is maximum. The spectral distance between the band edge modes can be varied with a sweep of the section widths and selected in order to have a value close to the desired mirror bandwidth. This first simulation step roughly sets the parameters defining the front mirror, but these values are refined with several iteration sequentially done with the following steps. A reflectivity computation using a 3D model requires too much time and RAM to be run on a regular computer when the number of periods involved are several tens. As a consequence, the model must be scaled down to lower dimensions. In order to do so, we use a 2D simulation to compute the effective mode index n_{eff_1} and n_{eff_2} of the two different regions of the front mirror. The computation is done at the target frequency and mode (fundamental lateral mode). Then a quasi-1D simulation is created as shown in the example in Fig.4.6.c where a single DBR period is reproduced: each one of the two regions is approximated by a 2D rectangular block with length equal to the designed length but width extremely reduced in size. The model is laterally constrained by perfect electric conductor boundary condition, in order to have no losses in the system. The effective refractive indexes n_{eff_1} and n_{eff_2} are assigned alternatively to each block, reproducing a period of the first order DBR. Two *Numeric Ports* are added to the model, at the extremities of the structure, and a Frequency Domain simulation is run exciting an electromagnetic radiation at a chosen frequency range from one of the Ports³. The S-parameter of the system is extracted and running this simulation

³COMSOL needs a preparatory study, once per port, of *Boundary Mode Analysis* in order to determine the electromagnetic wave profile at the Port before being able to run the Frequency Domain simulation.

for several repetition of the period gives a good estimation of the reflectivity bandwidth and of the Bragg frequency.

4.4.4 Multisection tapering

The transition between the main cavity with the second order lateral grating and the front mirror which employs a first order grating, it is done through the use of a tapering, which goal is to minimize the reflections at the interface between the two regions for the fundamental lateral mode. Based on the paper [82], the best solution for this problem is represented by a multisection tapering as illustrated by Fig.4.7.a. The multisection tapering design is formed by three isosceles trapezoids, which are individually defined by three quantities: b_a , b_b and l , respectively the major base, the minor base and the height of the trapezoids. In the figure, each quantity has a numbered label to specify the trapezoid. The multisection tapering has been optimized over several days of computation using the built-in optimization algorithms of CST Microwave Studio. Using the parameter in table 4.1 and as shown in Fig. 4.7.b, the transmission for the fundamental mode is greater than 90%, but it is strongly reduced for the higher order lateral modes. Therefore, this section would select further the fundamental transversal mode over the higher order modes, as these radiate out of the tapering.

	b_a (μm)	b_b (μm)	l (μm)
Section 1	48.2	37.8	16.8
Section 2	38.6	28.3	16.7
Section 3	30.5	20.7	22.2

Table 4.1: Optimized parameters for a multi-section tapering at 4.75 THz.

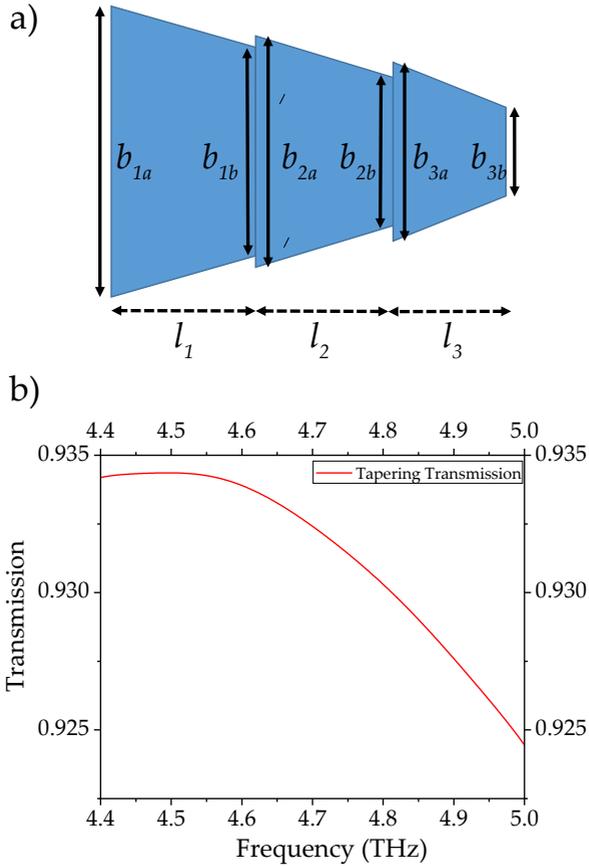


Figure 4.7: a) illustration of a multi-section tapering composed by three isosceles trapezoids which main parameters are specified in figure. b) Transmission properties of optimized tapering.

4.4.5 Outcoupler

The very front part of the laser, shown in the illustration in Fig.4.4, is not strictly part of the cavity, but part of the metal cladding that is deposited on the top of the cavity. The patch array antenna lies upon a BCB layer that is spun as described in Chapter 2 and it works as a surface outcoupler. The beam pattern emitted is single lobed and gaussian-like as shown in Fig.4.8.a, with an efficiency of $\sim 90\%$ [56].

4.4.6 Simulation of the whole cavity

A 2D or 3D simulation of the whole cavity would be computationally too heavy to be carried out with standard machines. Thus an in-house software called MIRREF is adopted in order to compute the threshold gain of the structure versus the frequency. MIRREF applies the transfer matrix method for the computation of the transmission. For the purpose of the simulation all the components of the photonic structures must be approximated to a sequence of layers which are identified by three quantities: the real and imaginary part of the refractive index and the length of the layer. As real part of the refractive index the n_{eff} computed via the 2D COMSOL simulation has been used. For the second order lateral grating section the losses estimated with a 3D simulation are inserted in the 1D model as thin layers of waveguide with an imaginary part of the refractive index proportional to the estimated losses. The layers were placed at the interface where the lateral offset is applied in order to spatially mimic where the loss due to the grating takes place. Carrying on the approximation in the described way, it has been possible to compute the threshold gain of all the four cavity sections arranged together. The result of the computation is summarized in the plot in Fig.4.8.b for three different number N of periods employed for the front mirror. All

the structures clearly show that a lasing mode placed at ~ 4.75 has a lower threshold gain, making it more likely to lase compared to other frequencies. Eventually, a $N = 70$ periods has been employed for the design of the front mirror.

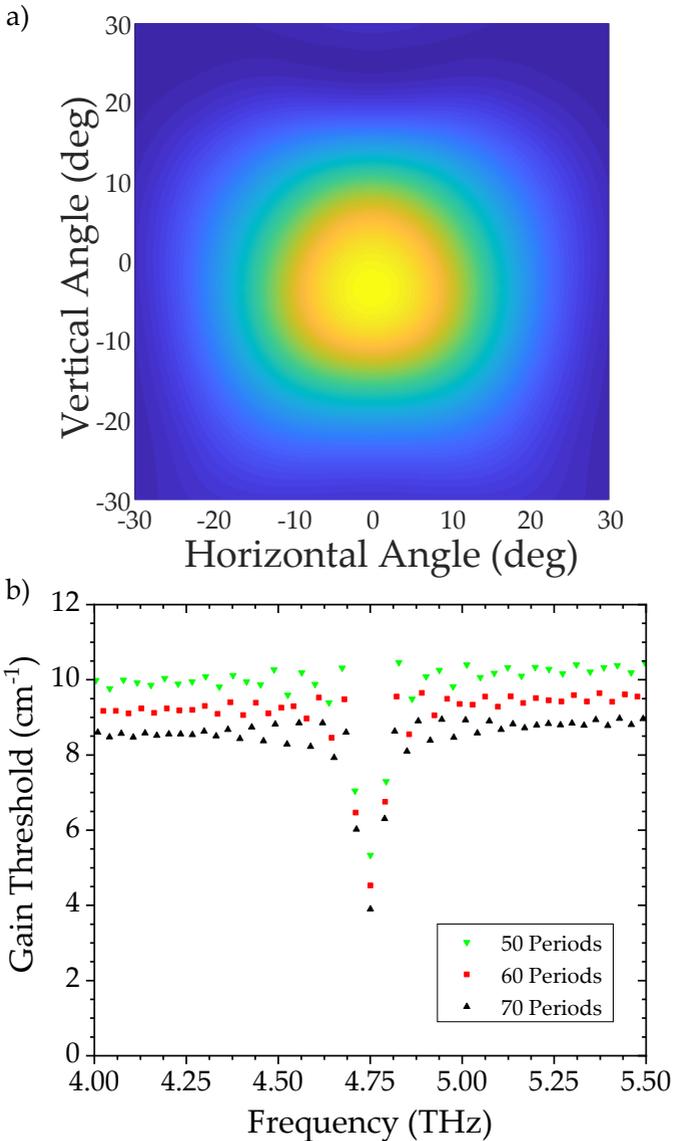


Figure 4.8: a) Simulated far-field pattern. b) The threshold gain analysis computed using the 1D transfer matrix method over the whole cavity design switching between $N = 50, 60$ and 70 periods for the front mirror. The computation shows that an electromagnetic wave at frequency 4.75 THz is more likely to lase.

4.5 Results

The process of the laser has been carried out with a standard BCB process as explained in Chapter 2. During this work, different layers as well as slightly different cavity designs have been tested. In the following subsection we will introduce all the tested generations, specifying the changes and the layers processed for that specific generation. All the layers are replica of EV1858, based on EV1116 and adapted to the required frequency (= 4.745 THz) [83]. The layer sequence is (in Å with barriers in bold) **51/93/10/105/33/87/42/165**, where the underlined layer is doped to $n = 2.0 \times 10^{16} \text{ cm}^{-3}$. On the processed mask, a chirping on the length of the cavity has been introduced. Each section of the laser has been "stretched" or "shrunked" by the same relative amount, varying the total length up to a maximum/minimum of $\pm 3\%$. As a consequence we expected an approximate frequency tuning of $\mp 3\%$ (corresponding to $\mp 150 \text{ GHz}$). The most noticeable results have been obtained with the layers EV1911, EV1980, EV2303 and EV1858, presented hereby in the historical order in which they have been processed and tested.

4.5.1 First generation devices

For this generation, the design of the cavity included a tapering section for impedance matching between the front mirror and the antenna section. The tapering section, simulated in the same fashion of the multi tapered section between the main cavity and the front mirror, had a transmission of $\sim 80\%$ for the selected frequency. The first generation design of the cavity has been tested on layers EV1911 and EV1980. Both layers have the same structure of EV1858 but EV1980 has a smaller number of periods, in order to have a total thickness of $9.2 \mu\text{m}$, well below half the wavelength of the electromagnetic wave in the medium. During the process,

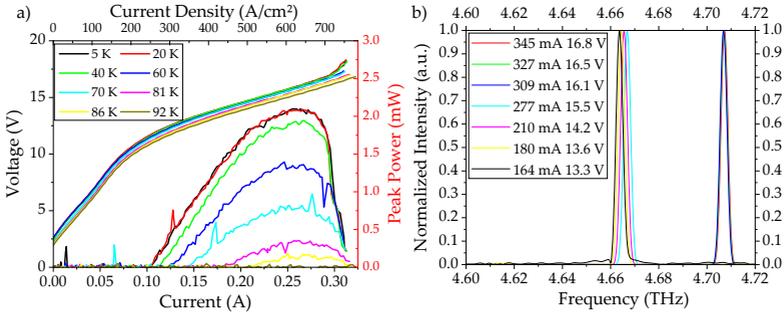


Figure 4.9: a) LIV example of a First generation device. The laser shown in this plot is obtained from EV1911 and it shows a maximum peak power of ~ 2 mW. b) First generation device spectra vs bias, acquired in continuous wave operation at 20 K. Although the majority of the devices has shown single modality over the whole dynamic range, some of them had a mode hopping close to roll-over bias.

EV1911, which active region thickness is $12.5 \mu\text{m}$, has not been etched down to $\sim 9 \mu\text{m}$ but the as-grown thickness has been kept.

After the process, only the chip obtained from the layer EV1911 lased. The reason is probably the incorrect process of EV1980 which has not received a Au etching step before spinning the BCB layers, leading to the presence of sputtered gold on the walls of the structures and a subsequent short circuit. The LIV performance of EV1911 is summarized in Fig.4.9.a, with a peak power up to 2 mW when operated at 10% duty cycle at 10 K and a maximum operating temperature above 86 K in pulsed mode. The power is measured using a Thomas Keating power meter. In Fig.4.9.b, device spectra vs applied bias acquired in continuous wave operation at 20 K are shown. The majority of the devices actually shown single modality over the whole dynamic range with sporadic presence of mode hopping close to the roll-over bias. The flaw of this generation of devices proved to be related to the final tapering; the presence of this section, thin and long, did not allow a flat BCB spinning in proximity of the

antenna. As a consequence, while the electromagnetic wave is transmitted through the tapering, it tends to radiate out from it and it is coupled into the polymer. The BCB will “unwillingly” work as a core of a lossy waveguide with a gold metal cladding below and air above. The result of this leak is shown in a far-field plotted in Fig.4.10 where the designed single mode lobe is substituted by multiple emissions coming from the coupling of the electromagnetic wave also to the antenna of the nearby passive devices. Moreover, this specific sample included on the same chip several devices at once, like shown in Fig.4.11.a, increasing the number of antenna passively emitting the coupled radiation. The thickness of the chip ($\sim 365 \mu\text{m}$ thick) made not possible to isolate a single device through cleaving technique, but with the afte this sample only chips with four or five lasers have been mounted. Lapping down to $\sim 200 \mu\text{m}$ would probably allow to cleave and isolate only one device.

4.5.2 Second generation devices

In the second generation of these devices, we focused more on optimizing the far-field. For this generation of devices, due to the lack of material for EV1911, the layers EV1980 and EV2303 have been processed. Both of these layers have a total thickness of $9.2 \mu\text{m}$. The tapering at the end of the front mirror has been removed and the antenna put closer to the front mirror edge, obtaining the design presented previously in this chapter. Moreover, the pitch between neighbor lasers has been increased from $170 \mu\text{m}$ to $225 \mu\text{m}$ in order to reduce the cross-talking between the devices. In this generation, the process of EV1980 has been successful, but the devices showed a high increase in voltage in the IV performance (Fig.4.12) which is probably due to a contact problem arisen during the fabrication.

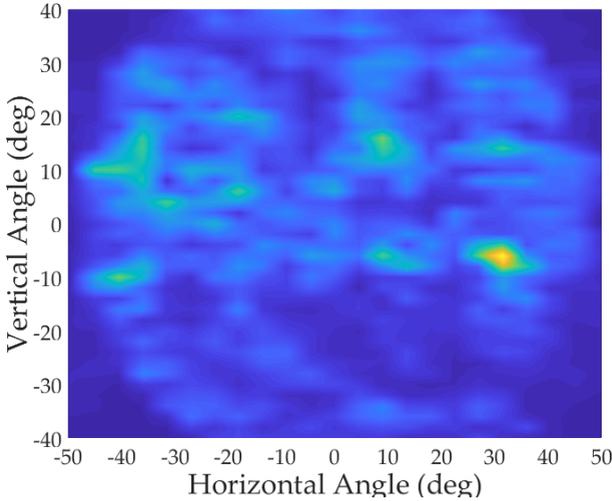


Figure 4.10: Far-field example of a first generation device. The far-field presents multiple lobes, coming from the emission of several antennas at once. This issue rose from the coupling of the electromagnetic mode also to nearby antenna, using the BCB as core of a waveguide.

As a consequence, our efforts have been focused on studying and characterizing the performances of EV2303, which are summarized in the plots in Fig.4.13, 4.14 and 4.15.a. The devices have consistently shown lasing performance up to 70 K, with an emitted power which reached almost 1.2 mW in continuous wave operation at 10 K as shown in Fig.4.13.a. For the fabricated lasers, the single modality has been achieved for 30 out of 31 lasers measured of the lasers and the device frequency followed well the frequency trend expected with the chirping of the cavity. Indeed, in Fig.4.14 the measured frequency versus the expected one is shown for the two processes that have been carried out for this generation. The graph shows that the trend followed by the measured frequency is approximately linear with a statistical deviation of $\sigma_{1st} = 21$ GHz for the first process and $\sigma_{2nd} = 6$ GHz

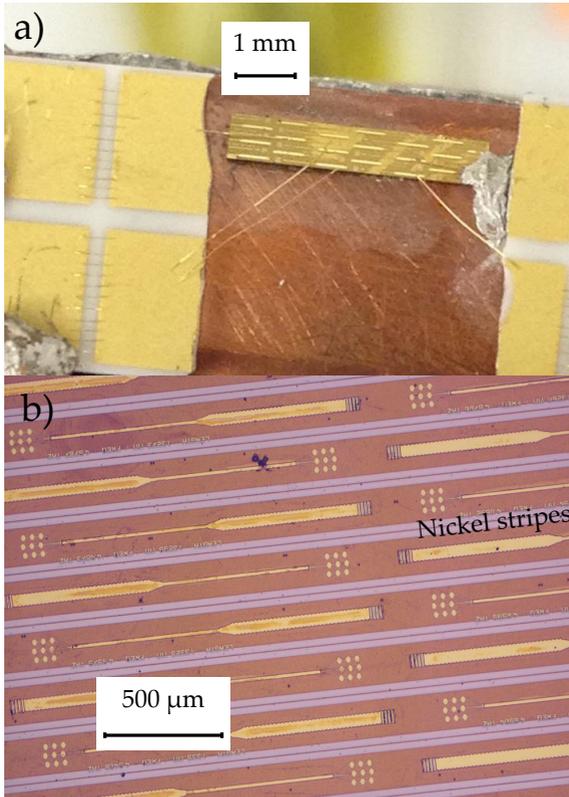


Figure 4.11: a) example of a mounted sample. In this picture, multiple devices distributed over three columns are visible. Neighbor devices are placed in opposite verses. b) A possible way to improve the far-field interference is to deposit Nickel stripes between the lasers in order to absorb leaking radiation.

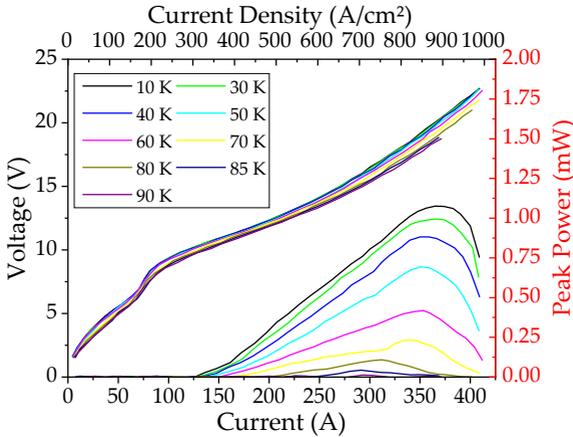


Figure 4.12: LIV example of EV1980. The high voltage is probably due to a contact problem arisen from unidentified fabrication issues.

for the second one. The second process also showed a blue offset of the frequency of ~ 25 GHz.

4.5.3 Third generation devices

This generation has been tested on EV2303 and EV1858. The only difference compared to the previous designs is that the pitch between the lasers has been increased again from 225 to 280 μm . Moreover, a final optional step has been added in order to deposit nickel metal stripes between neighbor devices as shown in Fig.4.11. Nickel is a high losses metal which absorbs leaking radiation and avoid cross-coupling between the antennas. The LIV and spectral performances of EV2303 are consistent to the second generation but, when the Nickel stripes are applied, the far-field results to be free from strong interference patterns as visible in the color plot in Fig.4.15.b.

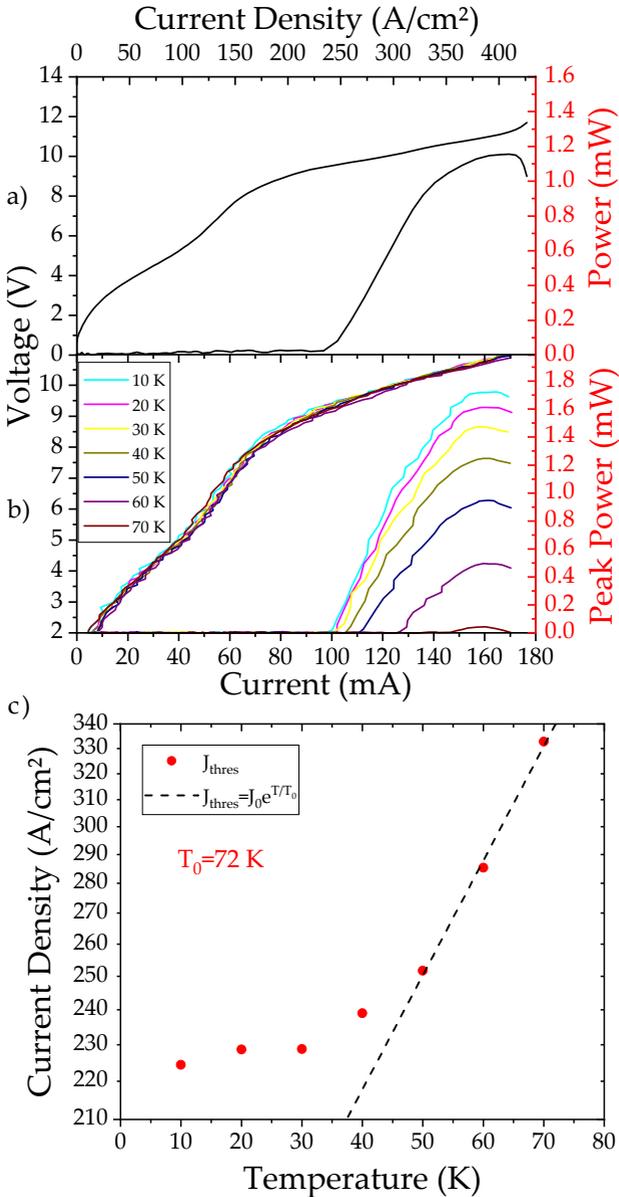


Figure 4.13: LIV performance of EV2303 both in a) continuous wave at 10 K and b) pulsed mode versus temperature at 80% duty cycle. c) panel shows the trend of J_{thres} versus the Temperature and the $T_0 = 72$ K resulted from the fit.

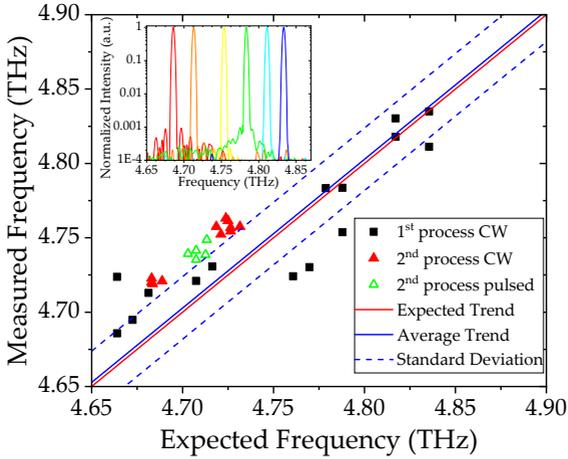


Figure 4.14: Trend of the measured frequency vs the simulated (expected) frequency of the device. The devices follow the expected trend with a statistical deviation $\sigma_{1st} = 21$ GHz for the first process and of $\sigma_{2nd} = 6$ GHz for the second process, although with an offset of $\Delta\nu = 25$ GHz.

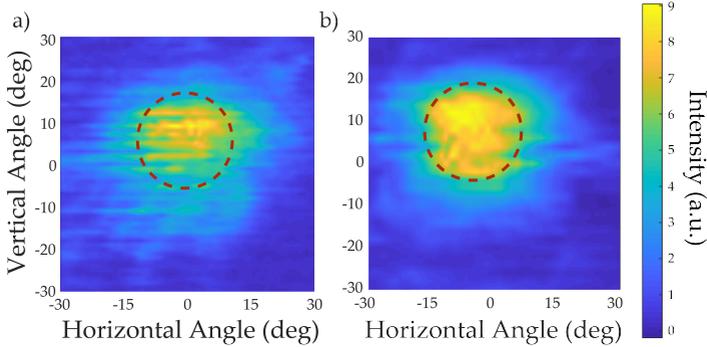


Figure 4.15: a) The far field of the second generation shows a single lobe pattern. However, an interference pattern is still present due to the nearby antenna cross-talk. b) When the Nickel stripes are deposited, the cross-coupling between the laser and the neighbor antennas is weaker and the interference pattern is almost completely removed, getting a result that is close to the simulated one. For both the far field, the red dashed line represent the full width half maximum.

EV1858

The emitted power of the devices processed from the layer EV1858 resulted to be almost 10 mW in pulsed operation and to be as high as 4.5 mW in continuous wave at 40 K. As shown in Fig.4.16.b, the output power resulted to be almost 10 times larger than for EV2303, although at a price of higher dissipated power. The devices of this batch have shown far-field patterns consistent to simulations. However, the fabrication yield of single mode devices has abruptly decreased to 33 devices over 61 measured and it has been more difficult to predict the laser frequency. Nonetheless, it has been possible to characterize devices with the target frequency spectrum.

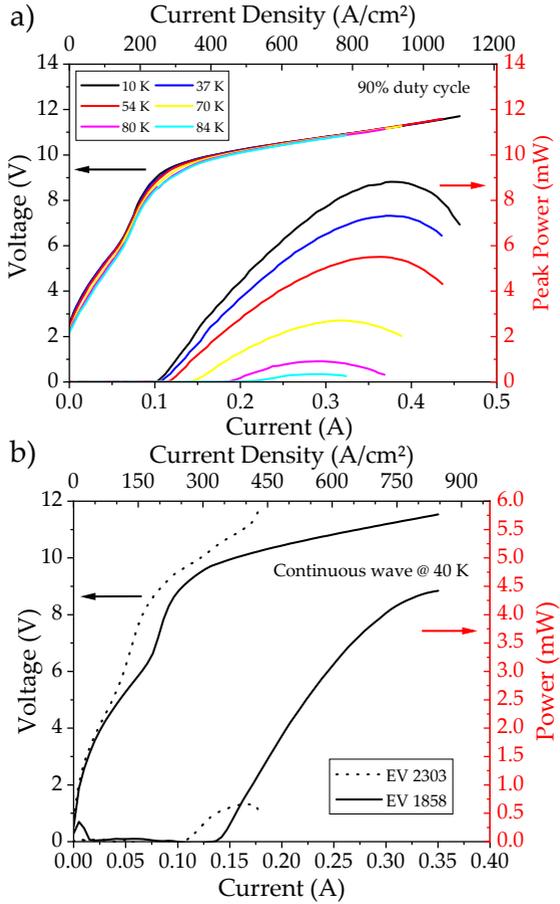


Figure 4.16: LIV in pulsed mode (above) and continuous wave (below) for EV1858. A comparison also to the layer EV2303 is shown, with an emitted power difference of almost a factor of 10.

4.6 Conclusions

On May 22nd 2018, a third generation device obtained from EV1858 has been employed as a local oscillator for the GREAT setup of SOFIA. The device showed lasing at a tunable frequency of $\nu = 4.745 \pm 0.003$ THz with sufficient output power to pump all the seven pixels assigned to the high frequency experiment of GREAT. The flight left from Palmdale, California, US, at sunset and landed again at dawn (~ 11 hours later) in the same location. That was the first of an ongoing > 30 flights series. More details about the setup mounting the laser treated in this chapter can be found in [74]. Future improvement of the design of a THz QCL for the purpose of a LO for SOFIA will probably move towards the VECSEL configuration, which has shown wide tunability range, gaussian far field patterns with low divergence and high emitted power [84].



Figure 4.17: In the picture (in random order): Urs Graf, Matthias Justen, Karl Jacobs, Robert Simon, Anna Parikka, Denise Riquelme, Timea Csengeri, Ronan Higgins, Oliver Ricken, Andreas Bell (and me). Thanks to you I have *literally* reached the highest altitude I will probably ever experience in my life.

InGaAs/GaAs based QWIP

While the challenges and achievements related to QCLs have been treated in the previous chapters, we will focus here on exploring a possible variation of a well established technology for THz detection: the Quantum Well Infrared Photodetector (QWIP) [85, 86]. On one side, we will investigate on the use of InGaAs/GaAs as active region for a QWIP, describing specifically the challenges in the design of quantum wells with this material system. Afterwards, we will show preliminary results on a QWIP cavity that takes inspiration from two state of the art QWIPs, one presented by Palaferri et al. involving the use of patch array antennas [87, 88] and the other exploiting LC resonances and loop antennas to couple light into microcavities as presented by Paulillo et al. [89].

5.1 The Quantum Well Infrared Photodetector

Along with the growing interest into THz radiation and the development of THz sources, also the need of better and more efficient detectors for the far-infrared grew along. However, when moving from the near and mid-infrared spectral region to longer

wavelength, interband transition can not be used anymore to produce efficient detectors because photon energies are too low to excite this transition. In this frequency range, common approaches are heat-based detectors, e.g. bolometers and pyroelectric crystals, which are sensitive but intrinsically slow [90]. Other THz-sensitive devices, such as non linear optical crystals and Schottky diode mixers, can utilize a coherent detector scheme, but they present limitation in sensitivity or in production cost. On the other hand, a well established detector which is instead based on III-V technology is the Quantum Well Infrared Photodetector. Like the QCL, the QWIP – as well as the Quantum Cascade Detector (QCD) [91] – is based on intersubband transition where the quantum well plays the role of the building block of the structure. These categories of devices are not as sensitive as bolometers but compensate with a higher speed. The working principle, well explained in [85], is basically depicted in Fig.5.1; a superlattice of quantum wells of equal thickness with one state mainly confined is subject to an electrical bias. Due to the applied bias a dark current is collected due to the drift of free carriers and thermally excited electrons. When the device is illuminated with a radiation which energy $h\nu_0$ is higher than the energy difference E_{21} between the confined state and the top of the barrier, electrons are excited out of the well into the continuum. Here they start to drift due to the applied bias and a new current is generated, called photocurrent, which is proportional to the number of photons absorbed. For the THz region, the most used material system is GaAs/Al_xGa_{1-x}As, where the composition x of Al and the width of the quantum well are used to select the peak detection wavelength [93]. Moreover, while for mid infrared QWIP the aluminum fractions varies from 15% to more than 20%, for the THz QWIP the percentage is abruptly reduced down to few percents, since the energy difference between the barrier height and the

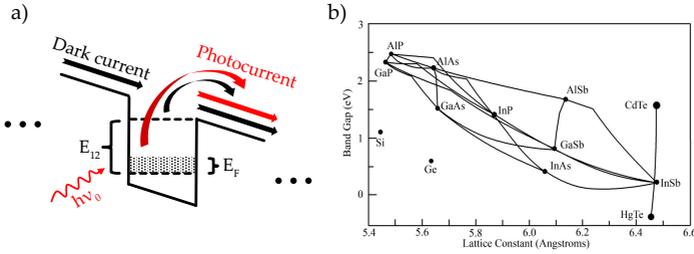


Figure 5.1: a) Illustration of the working principle of a QWIP. When an electrical bias is applied a dark current is collected due to the free carriers in the continuum. If a photon of sufficient energy $h\nu_0 > E_{12}$ is absorbed, a photocurrent is generated thanks to the transition into the continuum of the electron that absorbed the radiation. b) Lattice match diagram for several semiconductors. $\text{In}_x\text{Ga}_{1-x}\text{As}$ and GaAs heterostructures are lattice matched only for a specific composition of 53% In [92].

confined state must be comparable to the same energy of the THz radiation that the device must detect [93].

We decided to take advantage of this feature of the THz QWIP in order to explore $\text{In}_x\text{Ga}_{1-x}\text{As}/\text{GaAs}$ as a new material system for the engineering of a quantum well infrared photodetector. With such a material system, GaAs would now play the role of the barrier, while InGaAs would be the quantum well in the conduction band. This allowed to have a purer material for the barrier – which is the longest section of the single period – avoiding the use of Aluminium which is very reactive and tends to create ionized impurities reducing the electron mobility in the system. However, as visible in Fig.5.1.b, InGaAs and GaAs are not lattice matched. This means that during the epitaxial growth of $\text{In}_x\text{Ga}_{1-x}\text{As}$ upon a GaAs substrate the structure will accumulate strain that it will get relieved creating dislocations and defects once a certain thickness called *critical thickness* is reached [94]. The critical thickness reduces in size when increasing the mismatch between the epilayer and the substrate. In our specific case, the

higher the In concentration x , the lower the total thickness of quantum wells that can be grown epitaxially. However, as we will see, the amount of Indium needed for a THz QWIP is $\sim 2\%$, small enough to grow a strained structure which is $5 \mu\text{m}$ thick.

5.2 Design of InGaAs/GaAs quantum wells

The design of the structure has been made challenging by the wide amount of literature references reporting different information on InGaAs/GaAs heterostructures [95]. For the design we adopted the values reported by Vurgaftman et al. in [96], but we will show *a posteriori* that a better prediction is done according to a small re-adaptation of the work of Arent et al. [97]. A couple of assumption has been made for the design of the structure. The first assumption is that the effective mass of the electrons inside InGaAs is the same of GaAs. This assumption holds as long as the In concentration is low, which is our case. Secondly, we assumed that the strain was not changing the conduction band offset ΔE_c between InGaAs and GaAs and that, as a consequence, the value reported in [96] would faithfully approximate the real system. Experimental results will show later that this is not true. However, based on these assumptions, a $\Delta E_c = 20 \text{ meV}$ has been computed for $x = 2.0\%$. On this value, the design of the structure has been carried out using *sewself*, an in-house solver of Schödinger-Poisson self-consistent equations. The grown layer sequence has been **900**/75/100/75 Å, where bold character refers to the barrier and the underlined layer is doped with $3.5 \times 10^{16} \text{ cm}^{-3}$, according to the value used in [93]. The results of the simulation are summarized in Table 5.1 and the band structure is plotted in Fig.5.2.a. The table reports also the Fermi energy E_F computed according to the formula valid for a two level system $E_F = (\pi\hbar^2/m^*)n_D$, where n_D is the sheet doping density. The

activation energy E_{act} defined as the energy difference between the top of the barrier and the ground level energy (including E_F) is reported as well.

A better approximation of ΔE_c can be found using the empirical formula for the bandgap obtained by Arent et al. in [97] for $\text{In}_x\text{Ga}_{1-x}\text{As}$ single quantum wells with $x \leq 25\%$. The following formula for the band gap at 77 K of $\text{In}_x\text{Ga}_{1-x}\text{As}$ has been derived from [97] substituting the E_g value for GaAs at 0 K with the one of [96] (more recent):

$$E_g^0 = 1.519 - 1580x + 0.496x^2 \quad (5.1)$$

where x is the fraction of In in the ternary heterostructure. For the computation of the band offset, we assume a conduction/valence band offset ratio of 80/20, although literature is not really clear on this regard [95]. For 2% In one can compute $\Delta E_c = 26.6$ meV, a value much larger than the one computed before. We compared in Fig.5.2.b and in Table 5.1 the structures computed using the two different sources for the discontinuity values. The most important difference is the fact that the excited state is now confined inside the well. This will prevent the efficient extraction of the electron for low electrical biases.

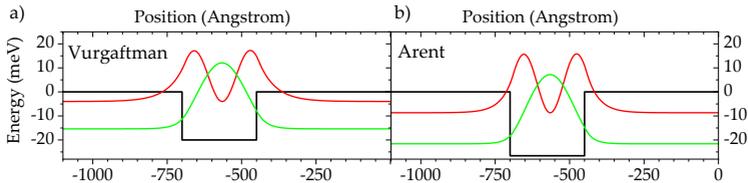


Figure 5.2: a) band diagram structure obtained with the ΔE_c value computed using Vurgaftman et al. data [96] versus b) the band diagram structure simulated considering the strain of the material according to Arent et al. [97]

	Vurgaftman et al.	Arent et al.
$\Delta E_c(2\%)$ [meV]	20	26.6
E_1 [meV]	4.63	4.99
E_{21} [meV]	11.39	12.94
z_{21} [Å]	69.39	65.17
E_F [meV]	1.25	1.25
E_{act} [meV]	14.12	20.36

Table 5.1: Table summarizing the main differences between the InGaAs/GaAs QWIP simulations with parameters adopted from two different source 96 and 97. $\Delta E_c(2\%)$ is the conduction band discontinuity between $\text{In}_{0.02}\text{Ga}_{0.98}\text{As}$ and GaAs, E_1 the confinement energy of the first eigenstate, E_{21} and z_{21} respectively the energy difference and the dipole moment between the excited and the ground level.

Depolarization shift

Many body effects are not actually predicted by *sewself* and must be computed and added a posteriori. The depolarization shift is typically the dominating many-body effect and it arises from the Coulomb interaction between the electron excited by the incident electromagnetic wave and all the other electrons [98]. The effect is mainly a shift of the absorption peak and it can be approximated by the formula:

$$E_{\text{depol}} \approx \frac{e^2 \hbar^2 n_{3D} f_{12}}{2\epsilon E_{21} m^*} \quad (5.2)$$

where E_{depol} is the depolarization shift, \hbar the Planck constant, e the elementary charge, n_{3D} the doping density, f_{12} and E_{21} respectively the oscillator strength and the energy difference between the ground and excited level of the quantum well, ϵ the dielectric function of the quantum well material and m^* the electron effective mass in the material. The oscillator strength can also be rewritten as:

$$f_{12} = \frac{2m_0}{\hbar} |z_{12}|^2 E_{21} \quad (5.3)$$

with m_0 electron rest mass and z_{12} the dipole moment between the levels considered. Substituting in equation 5.2 one can find

$$E_{\text{depol}} \approx \frac{e^2 m_0}{\varepsilon m^*} n_{3D} |z_{12}|^2. \quad (5.4)$$

For an InGaAs quantum well with low In concentration we assumed $\varepsilon = 12.9$ and $m^* = 0.067$. Using the values of the design the computation of the depolarization shift results in $E_{\text{depol}} = 3.09$ meV. In the THz range this is a consistent change in the level resonance to higher frequencies that must not be ignored.

5.3 Grating coupled double metal Mesa

Based on the layer sequence presented in the previous section, the layer EV2557 has been grown. The active region is composed by 42 periods with a total thickness of $\sim 5 \mu\text{m}$. The layer underwent a Au-Au double metal process (reported in Appendix) and square mesas of size $500 \times 500 \mu\text{m}^2$ have been fabricated. The thermocompressive bonding has been done with a semi-insulating layer of GaAs, so to keep the devices electrically floating. On top of the mesa a metal grating is used as surface coupler leaving a setback of $70 \mu\text{m}$ per side as contact pads. The grating is composed by metal stripes $10 \mu\text{m}$ wide and placed with a pitch of $\sim 20 \mu\text{m}$, designed to be resonant at ~ 4.7 THz. The process has been carried out using Ge/Au/Ni/Au as metalization for both the top and bottom contacts, consequently annealed at $400 \text{ }^\circ\text{C}$ for 2 minutes in order to obtain an ohmic contact. After processing, the sample has been cleaved in several chips of 4 mesas each and mounted on a flow cryostat provided with cryoshield and cold window in order to reduce the thermal radiation.

5.3.1 IV measurement

IV measurements of the QWIP have been taken in dark condition as well as in presence of thermal background using a cryoshield to reach a minimum temperature of 4.5 K. For the measurement of the IV in presence of a background, two different configurations have been used for the cryostat:

1. fitted with a Polymethylpentene (TPX) window, transparent to both far infrared and mid infrared radiation (as well as visible light)
2. fitted with a high density polyethylene (HDPE) window and a cold window for the cryoshield, in order to attenuate mid-infrared and thermal radiation

The IV measurement versus the temperature are shown in Fig.5.3. The difference in current between the measurement taken with a TPX window and a HDPE one plus a cold window configurations is justified by the presence of absorption of mid-infrared and perhaps even optical radiation, which contributes to generate a larger photocurrent. Following this result we only used the cryostat fitted with a cold window and a HDPE window for the remaining measurements. Comparing the data taken with the cold window configuration and in dark condition, a $T_{\text{BLIP}} = 10 \pm 1$ K can be extracted. Moreover, the activation energy E_{act} can be computed fitting the change in current (density) with the temperature T for a fixed bias according to the trend

$$J \propto \exp\left(-\frac{E_{\text{act}}}{k_b T}\right) \quad (5.5)$$

with J current density and k_b Boltzmann constant. For a bias of 200 mV, $E_{\text{act}} \simeq 17.1$ meV. This value is qualitatively in agreement with the simulations run with the parameters of Arent et al. (see Table5.1), indicating that the barrier height, *i.e.* ΔE_c (2%), is higher

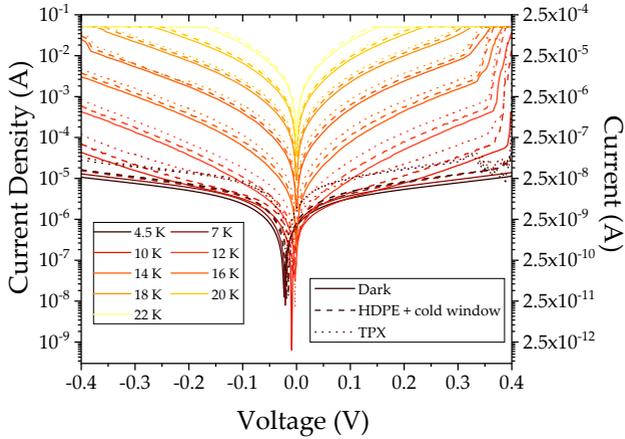


Figure 5.3: IV measurement of the QWIP vs temperature in three different configurations: dark condition, with a TPX window and with HDPE plus a cold window in order to screen the mid-infrared radiation. The comparison between the IV values measured in these configurations show that radiation at frequencies higher than THz frequencies are absorbed by the QWIP, contributing to the photocurrent, which is larger for the cryostat fitted with the TPX window.

than expected by the computation run with the values adopted by Vurgaftman et al. [96].

5.3.2 Photocurrent spectra

Using the QWIP as external detector of a commercial Bruker Vertex 80, spectrum of the glowbar used as internal source of the FTIR has been measured scanning for 10 minutes with a resolution of 5 cm^{-1} . The photocurrent spectrum is compared with the simulated band structure in Fig.5.4.b. The spectrum shows good agreement with the simulated band structure, with a peak absorption close to the top of the barrier, placed at 19.8 meV ($\sim 4.8 \text{ THz}$). The low frequency photocurrent peak, observed at 15.3 meV ($\sim 3.7 \text{ THz}$), corresponds to the excited level inside the quantum well when corrected with the depolarization shift E_{depol} . As the excited

level is not exactly in resonance with the top of the barrier, a tunnel-assisted thermoionic emission is observed. Indeed, the photocurrent has a strong field dependence around 3 THz.

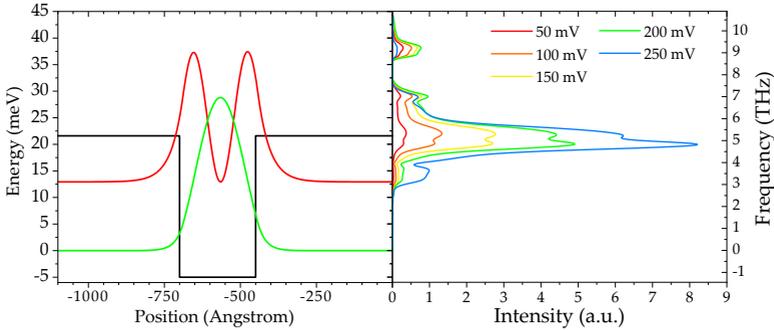


Figure 5.4: The photocurrent spectra of the QWIP is compared directly to the band structure simulation run with the parameters obtained from 97. The spectra show good agreement with the simulation.

5.3.3 Responsivity and LIV measurement

The measurement of the responsivity has been done using a third generation laser processed using the layer EV1858 of the kind introduced in Chapter 4. The setup used for carrying on the measurement is based on two off-axis parabolic mirror with a focal length of 4". The two mirrors collect and focus again the light from the laser onto the detector. In order to estimate the incident optical power, the laser has been previously calibrated using a Thomas Keating powermeter placed in the same position of the detector. Finally, a coupled power of 200 μW has been estimated acquiring the beam pattern of the laser with a THz Camera and comparing it to the collection area of the QWIP. The result of the measurement is reported in Fig. 5.5.

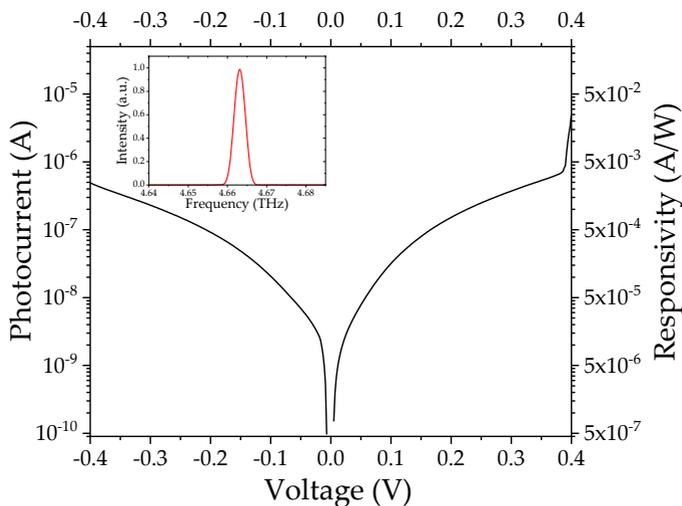


Figure 5.5: The photocurrent obtained when the detector is illuminated with 200 μ W power at 4.663 THz (spectrum shown in inset).

LIV characteristics of the laser have been measured using the QWIP as a detector. Without changing the operating condition of the laser, several LIV curves have been acquired versus the temperature of the QWIP and its bias. The collected data are reported in Fig.5.6.a and 5.6.b. In the first figure the acquired signal is plotted versus the temperature, showing that a decrease in signal can be recorded starting from 12 K and the detector stops working at around 20 K. This is consistent with the T_{BLIP} of the device. In Fig.5.6.b, the bias is swept, showing a consistent and constant increment of the detected signal. No saturation is observed, although higher bias could have been used¹.

¹However, some devices have shown degradation over time when operated above 400 mV. This has been observed especially during the measurements of IV vs T. When the sweep in voltage was done over an interval between -500 and 500 mV, from lower to higher temperatures, for some mesas it was impossible to replicate

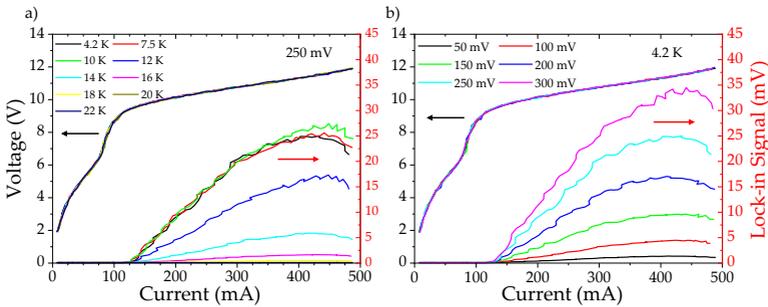


Figure 5.6: LIV characteristics of a laser obtained from EV1858 versus a) the QWIP temperature and b) the QWIP operation bias.

Responsivity measurement with Blackbody radiation

The responsivity can also be estimated from the background photocurrent of the device, using a TPX window and no cold window so to expose the photodetector to the radiation of the background, which can be approximated to a 300 K blackbody. However, since mid-infrared and visible radiations are not filtered by any window, they can contribute to the generation of photocurrent as already shown in Fig.5.3. This leads to an overestimation of the responsivity. Indeed, the incident power can be roughly computed integrating Planck's Law over the spectral range detectable by the QWIP. Knowing the TPX window size, the area of the detector mesa as well as its distance from the cryoshield allows to compute the fraction of power that is incident on the QWIP. A quick estimation of this power in the frequency range of 3 – 7 THz leads to the power value of $\leq 1.5 \mu\text{W}$, that is the upper limit of the radiation power that is absorbed by the QWIP. A responsivity lower limit of $\geq 0.025 \text{ A/W}$ at an operation bias of 300 mV can be found using the background photocurrent data

the IV measurement at low temperature and higher currents were measured.

collected with the TPX configuration and shown in Fig.5.3. This value is 5 times bigger than the one measured in this paragraph using a laser.

5.4 Antenna Enhanced QWIP

State of the art QWIPs take advantage of patch array antennas [87,99] or microcavities provided with loop antennas [89] in order to enhance the performance of the device. In the first case, the patch array antenna enhances the collection area A_{coll} of the detector and it has been shown that A_{coll} can be much larger than the geometrical cross section of the detector A_{mesa} . In the second case, a THz resonance at the desired frequency is engineered employing a loop antenna. The resonance enhance the collection efficiency of the device and it allows to detect THz radiation even with subwavelength active regions.

This paragraph introduces a design inspired by the merging of both these ideas. The successful application of BCB for the process of a local oscillator at 4.745 THz, previously presented in Chapter 4, suggested the idea of applying the same technology for the detector. Using an antenna deposited on BCB as surface in-coupler can allow a wide collection area even when the active region mesa is shrunk to a size of tens of micrometer. In this way, the active region size and the antenna size are no more co-dependent and higher value of specific detectivity can be obtained with a proper design. In the following sections, the adopted design and preliminary results are shown.

5.4.1 Cavity design and process

The cavity design of the antenna enhanced QWIP are based on the same patch array antenna used for the 4.745 THz local oscillator

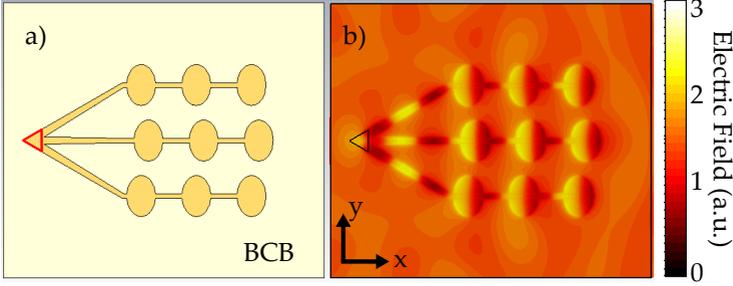


Figure 5.7: a) Top view of the design model of the microcavity QWIP simulated on CST. The red triangle at the intersection of the patch array antenna branches indicates the area of the microcavity mesa. b) The z-component (growth direction) of the electric field distribution when the model is excited with a plane wave coming from the top and polarized along the x -axis.

of Chapter 4. Active region mesas have an isosceles triangular shape of base $9.1 \mu\text{m}$ and height $8.1 \mu\text{m}$ for a total area of $\sim 37 \mu\text{m}^2$. The mesas are placed at the intersection of the feedlines of the patch array antenna as shown in Fig.5.7.a. Electromagnetic wave simulations have been run using CST Microwave Studio. The model shown in Fig.5.7.b has been excited with an electromagnetic wave at 4.75 THz polarized along the x -axis. From the results of the simulation it has been possible to compute the effective mode volume V_{eff} in the cavity [100,101]:

$$V_{\text{eff}} = \frac{\int d\mathbf{r} \varepsilon(\mathbf{r}) |u(\mathbf{r})|^2 d\mathbf{r}}{\left(\frac{\lambda}{n}\right)^3} \approx 0.7 \quad (5.6)$$

where \mathbf{r} is the position vector, $\varepsilon(\mathbf{r})$ is the dielectric function of the medium, $u(\mathbf{r})$ the electric field profile (electric field normalized by its maximum), λ the wavelength of the incident electromagnetic wave and n the refractive index of the cavity medium. Moreover, the electric field enhancement E_{en} defined as the ratio between the maximum electric field amplitude E_{max} in the cavity and the amplitude of the incident plane wave resulted to be ~ 50 .

The value of V_{eff} indicates that the electric field is not strongly confined in the cavity. Nonetheless, the efficient collection of the electric field by the antenna leads to a computed electric field enhancement up to a value of 50. The samples are processed

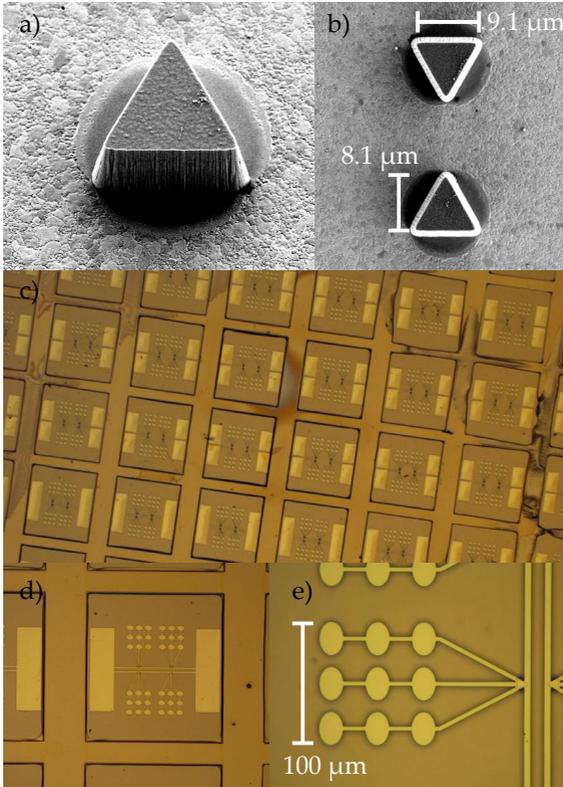


Figure 5.8: a) and b) report SEM picture of the as-etched microcavity. c), d) and e) are optical microscopy picture of the completed sample at different magnifications.

with the standard BCB process introduced in Chapter 2 including also the steps necessary to etch BCB mesas and expose the bottom

metal contact for keeping the device electrically floating. Fig.5.8 shows images acquired during and at the end of the process. As visible, the QWIPs are processed in clusters of four, with different configuration presenting only one, two or all four devices in parallel. The size of the BCB mesa is equal to the size of the grating coupled double metal QWIP mesa presented in the previous sections of this chapter in order to have optical collection areas of almost comparable size.

5.4.2 IV performance

The IV characteristics in absence of background radiation has been measured with a Keithley 2636B and plotted in Fig.5.9.a versus temperature, compared also to the IV characteristic acquired at minimum temperature in presence of background radiation. For the microcavity QWIP a $T_{\text{BLIP}} = 11 \pm 1$ K can be extracted, with a 1 K improvement compared to the grating coupled double metal mesa. In Fig.5.9.b the JV characteristics of the microcavity QWIP and the grating coupled double metal mesa (that will be regarded as "reference mesa" from now on) are compared, showing agreement in current density between the two designs.

5.4.3 Laser detection

Using the microcavity QWIP as detector of the FTIR we detected exactly the same laser signal previously measured by the reference mesa. The performance of the antenna detector was obtained by making the ratio of the signal with the one of the reference mesa in the same experimental conditions. In Fig.5.10.a, data show that the signal acquired with the reference mesa is 30 times larger than the one acquired with the microcavity QWIP. The collection area ratio between the microcavity QWIP and the grating coupled double metal QWIP is given by the ratio between the patch array antenna

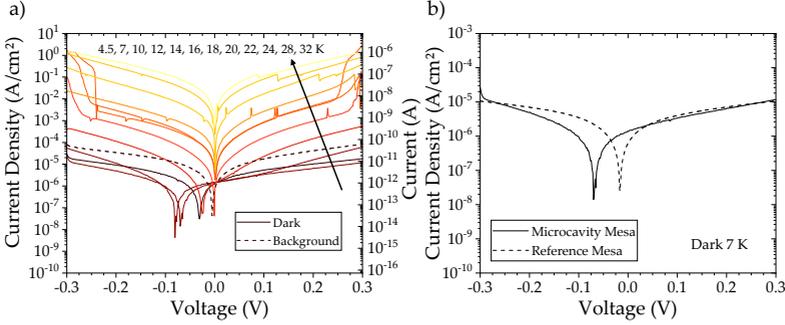


Figure 5.9: a) IV characteristic in dark environment and b) compared at 7 K with the reference mesa.

and the grating². Since the microcavity QWIP shown in Fig.5.10.a is a doublet, two antennas are used for the collection of the signal. Hence the ratio is

$$A_{\text{ratio}} = \frac{A_{\text{antennas}}}{A_{\text{grating}}} = \frac{100 \times 100 \times 2}{430 \times 430} \approx 0.1 \quad (5.7)$$

The Responsivity R of the microcavity can be computed using the data previously shown for the reference mesa. With an applied bias of 200 mV the grating coupled double metal mesa has reported a Responsivity $R_{\text{ref}} = 5 \times 10^{-4}$ A/W at the laser frequency (see Fig.5.5). Considering the ratio between the collection areas of the devices and the signal peaks acquired in the FTIR, the Responsivity of the microcavity QWIP *decreases* by a factor of 3, thus $R_{\text{micro}} = 1.7 \times 10^{-4}$ A/W at the laser frequency. The decrease in Responsivity could be explained by an attenuation of the electromagnetic wave due to absorption by the BCB and by a less efficient optical in-coupling of the wave from the antenna compared to the metal grating. Nonetheless, the

²In the following computation, we adopt a conservative definition of collection area A_{coll} , neglecting the antenna effect of the array which would enhance the collection area [88]. Reflectivity measurements of the antenna will be taken in the future in order to estimate properly A_{coll} .

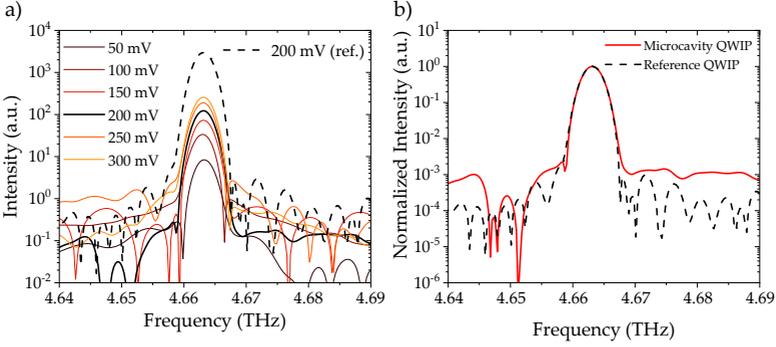


Figure 5.10: Laser spectra acquired with the microcavity QWIP and plotted in logarithmic scale. In a) the spectra are shown vs the applied bias of the microcavity QWIP reporting also the spectra acquired at 200 mV with the reference mesa for direct comparison. In b) the normalized spectra at 200 mV is compared with the reference mesa.

advantage of using a microcavity design rises from the reduced Noise Equivalent Power (NEP), defined as the amount of injected power needed to have a signal-to-noise ratio equal to 1. Indeed, the noise of the QWIP is given by the dark current, proportional to the QWIP geometrical cross section of the active region A_{mesa} according to the formula [99]

$$I_{\text{dark}}(T) \propto A_{\text{mesa}} \exp\left(\frac{-E_{\text{act}}}{k_b T}\right) \quad (5.8)$$

Specifically, the ratio of the measured dark currents for the reference mesa and the microcavity mesa at the operation bias of 200 mV and $T = 4.5$ K is

$$I_{\text{ratio}} = \frac{I_{\text{dark}}^{(\text{micro})}(200 \text{ mV})}{I_{\text{dark}}^{(\text{ref})}(200 \text{ mV})} = \frac{7.4 \times 10^{-12} \text{ A}}{10.9 \times 10^{-9} \text{ A}} = 0.7 \times 10^{-3} \quad (5.9)$$

and the NEP ratio between the microcavity and the reference mesa can be computed considering both the Responsivity ratio $R_{\text{ratio}} =$

1/3 and the I_{ratio} just computed

$$\text{NEP}_{\text{ratio}} = \frac{I_{\text{ratio}}}{R_{\text{ratio}}} = 2 \times 10^{-3} \quad (5.10)$$

that shows an improvement of the NEP performance for the microcavity QWIP. One can also compute the ratio of the specific detectivity $D^* = \frac{\sqrt{A_{\text{coll}}\Delta f}}{\text{NEP}}$, with A_{coll} collection area and Δf the considered bandwidth, equal for both the detectors. Considering the ratio just computed, the specific detectivity ratio is

$$\frac{D^*_{(\text{micro})}}{D^*_{(\text{ref})}} = 155 \quad (5.11)$$

showing a strong improvement in the performance of the microcavity detector with respect to the reference mesa.

5.5 Conclusions

The results showed in this Chapter demonstrate that the material system InGaAs/GaAs can be successfully used for the realization of THz QWIP, with a responsivity up to 5×10^{-3} A/W when measuring radiation at ~ 4.7 THz. A preliminary design of a microcavity QWIP embedded in BCB and provided of a patch array antenna has been also shown. The antenna enhanced QWIP has shown IV characteristics comparable to the reference mesa and specific detectivity 155 times larger when detecting a laser provided with the same patch array antenna for outcoupling. Possible and further development of the project will imply testing the microcavity devices at high modulation frequency, taking advantage of the reduced size of the active region area, hence of the smaller RC time constant this design offers.

Conclusion

This work has mostly been based on the THz Quantum Cascade Laser. In Chapter 1 we have introduced the state of the art for this technology. In Chapter 2 we have shown the processing methods adopted in this thesis. In particular, we have reported in detail the processing steps necessary to embed THz QCLs in Benzocyclobutene (BCB) and the challenges of processing double metal waveguides replacing Au with Cu. We have then presented the latest results on high temperature operation of this technology. Specifically, we have reported a systematic study involving 24 different layers and several processes. The conducted study culminated with a new world record device operating up to 210 K and able to emit 200 mW at 40 K and 1.2 mW at 206 K, which paves the way to possible applications even when operated at high temperature. Moreover, thanks to the high peak power emitted even above 200 K, it has been possible not only to operate for the first time a THz QCL with a thermoelectric cooler, but also to detect the signal using a room temperature detector commercially available. This is the first demonstration of a cryogenics free source-detector system that involves the use of a THz QCL and the most important achievement of this thesis. This PhD work has

also been based on the design and development of a THz QCL to be used as a local oscillator for the heterodyne measurement of SOFIA at 4.745 THz. The local oscillator needed to satisfy several requirements given by the limited equipment that SOFIA can carry on board. These requirements are operation above 40 K in continuous wave, output power > 1 mW with a single lobe far-field and single mode emission at 4.745 THz. The design of the cavity is composed by several parts and exploited widely electromagnetic wave simulations. The process, which involved the use of BCB, led after a couple of generations to satisfy the requirements. In particular, the device managed to lase at the required frequency, emitting 4.5 mW in CW operation at 45 K with an electrical dissipation lower than 4 W. Finally, the use of a patch array antenna as a surface outcoupler shaped the beam pattern into a single lobe with a divergence angle of $\sim 30^\circ$. In the last Chapter we demonstrated for the first time the operation of a THz QWIP based on a InGaAs/GaAs active region. Moreover, using a patch array antenna for the incoupling of the THz radiation allowed to reduce the size of the electrical area of the device, favoring the reduction of the noise of the detector and increasing the specific detectivity by two orders of magnitude compared to the reference detector based on a double metal grating coupled mesa.

Processing basic recipes

In the following sections we will introduce standard recipes for Au-Au double metal processes as well as some detailed recipe regarding the BCB process introduced in Chapter 2.

A.1 Au-Au double metal process

The Au-Au double metal process has been widely applied in this thesis work, especially in the wet-etched version, which represented the easiest and fastest processing recipe for THz QCL in our cleanroom, hence essential for a quick evaluation of the growth status of the MBE and benchmark of layers. In the next tables we will introduce the basic recipe steps for a Au Au double metal process. We will discuss details of the step when needed later in the Appendix.

N.	Processing Step	Details
1	Cleaning and cleaning	using ACE:ISO:H ₂ O
2	Evaporation	Ti/Au (10/250 nm)
3	Wafer Bonding	5 MPa, 320 °C for 15 minutes
4	Lapping	leaving 30 – 40 µm margin using 15 µm diamond paper
5	Selective removal	Using Citric Acid 50% (3:1 with H ₂ O ₂) at 35 °C
6	HF etching	40% concentration for 3 minutes
7	Top contact photolitho and evaporation	Ti/Au (10/250 nm)
8	Hard mask deposition, photolitho and dry etching	3 µm of SiN _x
9	Ridges dry etching	Room Temperature etching using Cl ₂ /Ar plasma
10	Back lapping	Thinning down to ~ 200 µm
11	Back evaporation	Ti/Au (10/50) for back-end InAu soldering
12	Hard mask removal	Buffered HF (1:5) for 3 minutes

Table A.1: Summary of the main steps for Au-Au double metal dry-etched waveguide fabrication for a GaAs/AlGaAs heterostructure.

A.1.1 dry etched AlGaAs/GaAs structures

N.	Processing Step	Details
1	Cleaning and cleaning	using ACE:ISO:H ₂ O
2	Evaporation	Ti/Au (10/250 nm)
3	Wafer Bonding	5 MPa, 320 °C for 15 minutes
4	Lapping	leaving 30 – 40 μm margin using 15 μm diamond paper
5	Selective removal	Using Citric Acid 50% (3:1 with) at 35 °C
6	HF etching	40% concentration for 3 minutes
7	Top contact photolitho and evaporation	Ti/Au (10/250 nm)
8	Ridge photolitho and wet etching	using H ₃ PO ₄ :H ₂ O ₂ :H ₂ O (1:1:1)
9	Back lapping	Thinning down to ~ 200 μm
10	Back evaporation	Ti/Au (10/50) for back-end InAu soldering
11	Photoresist removal	with (hot) acetone

Table A.2: Summary of the main steps for Au-Au double metal wet-etched waveguide fabrication for a GaAs/AlGaAs heterostructure.

A.1.2 wet etched AlGaAs/GaAs structures

N.	Processing Step	Details
1	Cleaving and cleaning	using ACE:ISO:H ₂ O
2	Evaporation	Ge/Au/Ni/Au (48/50/10/350 nm)
3	Wafer Bonding	5 MPa, 320 °C for 15 minutes
4	Lapping	leaving 30 – 40 μm margin using 15 μm diamond paper
5	Selective removal	Using Citric Acid 50% (3:1 with H ₂ O ₂) at 35 °C
6	HF etching	40% concentration for 3 minutes
7	Top contact photolitho and evaporation	Ge/Au/Ni/Au (48/50/10/150 nm)
8	Hard mask deposition, photolitho and dry etching	3 μm of SiN _x
9	Mesas dry etching	Room Temperature etching using Cl ₂ /Ar plasma
10	Back lapping	Thinning down to ~ 200 μm
11	Back evaporation	Ti/Au (10/50) for back-end InAu soldering
12	Hard mask removal	Buffered HF (1:5) for 3 minutes
13	Annealing	400 °C for 2 min in Nitrogen atmosphere

Table A.3: Summary of the main steps for Au-Au double metal dry-etched mesa fabrication with ohmic contacts for a InGaAs/GaAs heterostructure

A.1.3 dry etched InGaAs/GaAs structures for QWIP

N.	Processing Step	Details
1	Cleaving and cleaning	using ACE:ISO:H ₂ O
2	Evaporation	Ti/Au (10/250 nm)
3	Wafer Bonding	3.5 MPa, 280 °C for 15 minutes
4	Lapping	leaving 30 – 40 μm margin using 15 μm diamond paper
5	Selective removal	Using HCl 35%
6	Top contact photolitho and evaporation	Ti/Au (10/250 nm)
7	Ridge photolitho and wet etching	using H ₃ PO ₄ :H ₂ O ₂ :H ₂ O (1:1:1)
8	Back lapping	Thinning down to ~ 200 μm
9	Back evaporation	Ti/Au (10/50) for back-end InAu soldering
10	Photoresist removal	with (hot) acetone

Table A.4: Summary of the main steps for Au-Au double metal waveguide fabrication for a InP/InGaAs/InGaSb/AlInAs heterostructure.

A.1.4 wet etched InP/InGaAs/InGaSb/AlInAs structures

A.1.5 Etching recipes

The processing table just introduced are partly based on well-established recipe steps. The following tables introduces the recipe used for the dry etching of GaAs/AlGaAs active regions in ICP, the deposition of SiN hardmasks in PECVD and the patterning of the SiN with RIE etching.

GaAs/AlGaAs dry etching

Recipe	Bosco GaAs
Ar (sccm)	7.0
Cl ₂ (sccm)	8.0
N ₂ (sccm)	2.0
Temperature (°C)	45
pressure (mTorr)	~ 2.0
ICP power (W)	600
RF power (W)	80
etch rate (μm/min)	1.5

SiN_x deposition and etching

SiN mask deposition recipe:

Recipe	Dana SiN
SiH ₄ (N ₂) 2.5 % (sccm)	800
NH ₃ (sccm)	30
Temperature (°C)	0
Pressure (mTorr)	900
LF power (W)	0
Pulse time (s)	0
RF power (W)	20
Pulse time (s)	0
deposition rate (μm/hour)	0.86

Recipe for an RIE etching of SiN_x selectively to resist.

Recipe	Dana SiN mask
CHF ₃ (sccm)	40
O ₂ (sccm)	60
Temperature (°C)	18
Pressure (mTorr)	25
Forward power (W)	55
etch rate (μm/hour)	4.5

A.2 BCB processing recipes

BCB processing has already been introduced in Chapter 2. In the following tables we report the steps used for curing and etching the BCB. For curing a nitrogen oven is used.

A.2.1 BCB curing

BCB curing is done heating up the sample above 200 °C in a Nitrogen atmosphere in order to have glass transition. Specifically we distinguish between two different curing steps; soft and hard baking. The difference between the two resides on the baking temperature, higher for the hard version as visible in the following tables. Hard baking takes more time but creates a better uniformity between the spun BCB layers and it is advised to do a hard baking as last curing step, when all the layer have been spun.

A.2.2 BCB etching

Etching of BCB in the RIE is a delicate step that might require also short etching time (< 10 s) when the BCB is almost completely removed from the top contact of the devices.

Step	Duration (min)	Process
1	5	ramp to 50 °C
2	5	soak at 50 °C
3	50	ramp to 180 °C
4	180	soak at 180 °C
5	40	ramp to 210 °C
6	60	soak at 210 °C
7		cooldown

Table A.5: Soft baking of BCB

Step	Duration (min)	Process
1	5	ramp to 50 °C
2	5	soak at 50 °C
3	50	ramp to 180 °C
4	180	soak at 180 °C
5	40	ramp to 250 °C
6	60	soak at 250 °C
7		cooldown

Table A.6: Hard baking of BCB, used after the last spinning.

Recipe	Geiser BCB
CF ₄ (sccm)	40
O ₂ (sccm)	60
Temperature (° C)	18
Pressure (mTorr)	100
Forward power (W)	200
etch rate (μm/min)	1.05

Table A.7: Etching parameters of BCB.

Electrical contact study

Over the course of this PhD work, several layers have been grown and tested, especially for the systematic study conducted in Chapter 3. Some of the grown layer presented contact problems and needed to be reprocessed several times. The layers EV2587 and EV2610 are part of this category of layers and have represented a chance to test some contact and top metallization.

B.1 Pt/Au as top metallization and Au diffusion barrier

The layer EV2610 has been grown with an Indium-rich top contact (composition of InGaAs up to 50% in Indium) which is more than the standard 35%. Immediately after a benchmark process based on Au-Au wet etched waveguides as described in Table A.2, the performance of the laser proved to be poor, with a maximum operating temperature lower than 90 K, as shown by the dashed line in Fig.B.1. The reason of the bad performance is probably due to the diffusion of Au into the high In region at the interface with the active region. This is likely to happen at high temperature, which are applied during the wafer bonding. It has not been

checked through EDX on the processed samples, but the diffused Au would tend to form an InAu alloy at an eutectic point of fusion. This would probably hinder the performance of the laser. In order to solve the problem two approaches I have been tried. The first tentative consisted in starting the process of the sample with an etching step based on HCl etching (30 seconds in 32% HCl concentration solution) and Ar ion bombardment. This step was meant to remove the top layer of the sample, where the In concentration is higher. Once the benchmark process finished, a ~ 20 K improvement in temperature performance has been recorded, as plotted by the dotted line in Fig. B.1. The best performance has been obtained with the second approach, based on using platinum (Pt) instead of titanium as an adhesion layer (and diffusion barrier). Using 5 nm Pt / 500 nm Au as first metallization before the wafer bonding step, the processed lasers reached a maximum temperature of 147.5 K.

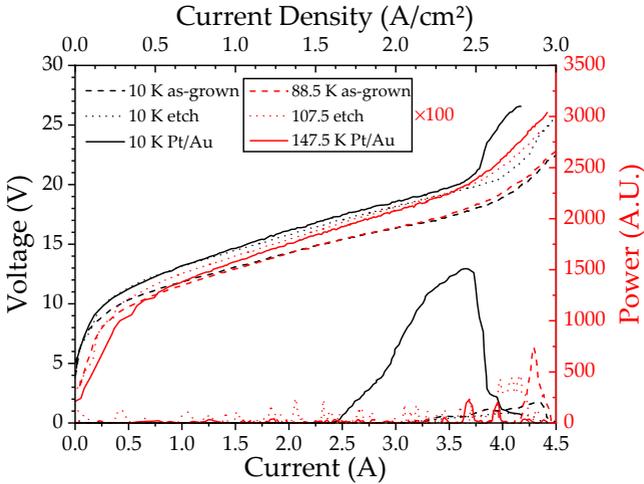


Figure B.1: LIV performance of EV2610 are plotted with different top metallization. The as-grown sample (dashed line) has poor performance when deposited with a standard Ti/Au contact, probably due to InAu alloying at the interface between the active region and the metallization. When the top contact of the active region is etched using HCl and Ar ion bombardment, the maximum temperature performance improves because the amount of In is reduced (dotted line). Eventually, a top metallization composed by Pt/Au proved to avoid any InAu alloying and outclassed in performance the other configurations (solid line).

B.2 GaAs as top contact layer

The results obtained from EV2610 suggested to improve the growth of the active region completely removing the any In from the epitaxial layer. The challenges of this task are beyond the goal of this PhD work and I have been treated by Dr. Mattias Beck. The layer EV2587 proved to be a good test layer for this experiment. After its first process, the top contact, based on 35% In, proved to be defective. This led to an extremely high applied bias in order to inject electrons, as visible in dotted line in Fig.B.2. The contact has been regrown on two different quarter of the epilayer with two different approaches. The first approach was based on a high

In-concentration top contact, in a similar fashion to EV2610. The second contact growth consisted instead of a pure GaAs epilayer heavily doped with Si. In both cases, both the contact layers led to similar results (dashed and solid line in Fig.B.2). These results assure that a top contact based on pure GaAs can be adopted instead of a InGaAs contact, avoiding undesired diffusion effect and alloying of InAu.

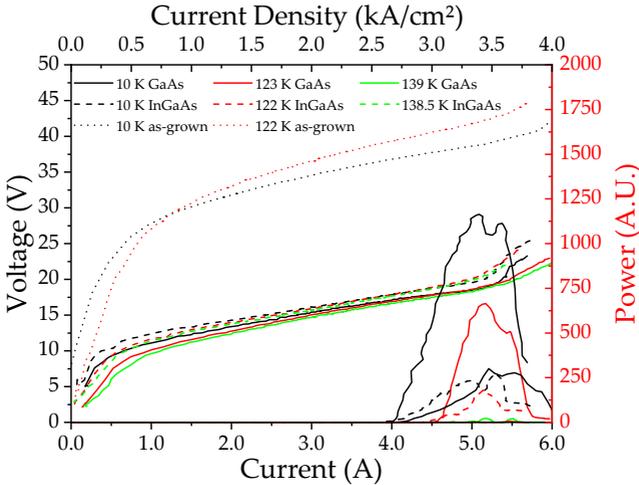


Figure B.2: LIV performance of EV2587 are plotted with different top contact growth. The as-grown sample (dashed line) has poor performance when deposited with a standard Ti/Au contact, probably due to InAu alloying at the interface between the active region and the metallization. When the top contact of the active region is etched using HCl and Ar ion bombardment, the maximum temperature performance improves because the amount of In is reduced (dotted line). Eventually, a top metallization composed by Pt/Au proved to avoid any InAu alloying and outclassed in performance the other configurations (solid line).

Heat transfer computation and laser box design

The thermoelectric cooling is an effect based on the Peltier effect for which a current flow in a junction between two conductors induces also a heat flow. It is the exact counterpart of the Seebeck effect, which generates a current across two different conductors through a difference in temperature. A Thermoelectric Cooler (TEC) or Peltier cell/cooler is a device that gets advantage of this effect to cool down one of its side and symmetrically heating up another. If one efficiently extracts the generated heat from the hot side of the cell, then it is possible to cool down the cold side even further and to reach temperatures well below 0 °C. The difference in temperature between the hot and the cold side is called ΔT . This is the most important parameter characterizing a TEC and it is usually function of the hot side temperature, the power injected into the TEC and the heat load of the cold side. In this thesis, a thermoelectric cooler has been adopted for the first time in order to cool down and operate a THz quantum cascade laser. The TEC is a 4-stage configuration from II-VI Marlow Industries, model SP2394, which specs are reported in Fig.C.1.a for an hot side temperature of

27 °C. Specifically, the TEC is able to assure a $\Delta T = 100$ °C when a heat load of 1 W is dissipated on the cold side. This would assure a minimum temperature low enough to operate a laser at 200 K. Extracting efficiently the heat from the hot side of the TEC as well as reducing as much as possible thermal bridges to the cold side are the most important goals to pursue when designing a laser box. Heat extraction is usually done using continuous flow of liquid right below the hot side of the TEC. In our specific case we used water at 17 °C, passing through a serpentine channel engraved in the copper base of the laser box, as shown in Fig.C.1.b. A pedestal in copper holding the TEC is screwed down directly on top of the channel, sealed with an o-ring and vacuum grease to avoid water and air leaks. The thermal conduction equation that regulates the heat flow between two objects at different temperature T_1 and T_2 , with $T_2 > T_1$, is

$$\dot{Q} = \frac{\kappa A (T_2 - T_1)}{d} \quad (\text{C.1})$$

where the \dot{Q} is the power exchanged, A and d the area and the length of the material connecting the two objects and κ the thermal conductivity, which depends on the material.

When it comes to choose the material and the size of the parts composing the laser box, three easy rules can be listed down:

1. Anything connected to the hot side of the thermoelectric cooler should have high thermal conductivity in order to efficiently extract the heat
2. Any thermal bridge between a room temperature object and the TEC cold side should have low thermal conductivity in order to reduce the heat load
3. in between the cold side and the laser there should be a medium with high thermal conductivity

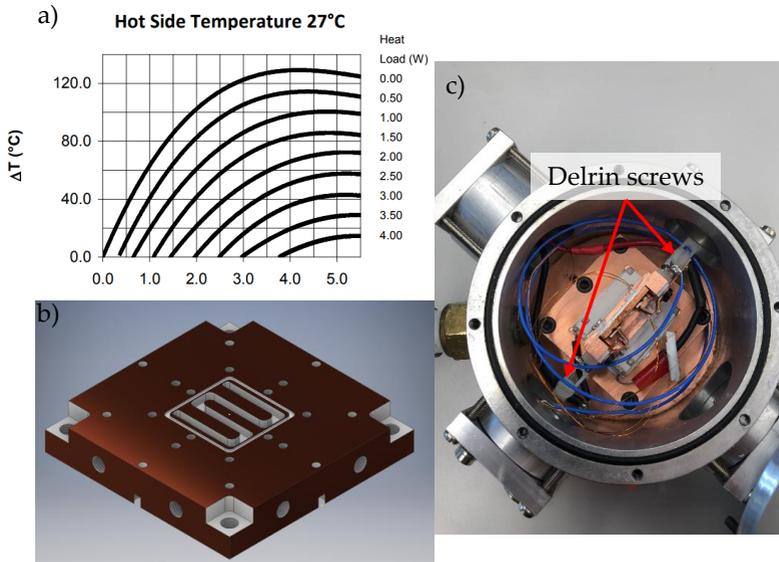


Figure C.1: a) Specifications of the adopted thermoelectric cooler (TEC) with a hot side temperature of 27 °. The TEC has a resistance of 0.5 Ω b) The copper base of the laser box is engraved with a serpentine channel in order to make water flow below the hot side of the Peltier cell. c) A picture of the laser box. Delrin screws and long wire connections are important to reduce drastically the heat load on the cold side of the TEC.

Common thermal bridges connected to the cold side of the TEC are the screws used to press the Peltier cell against the heat sink and the electrical wires that are used to inject current into the laser and to measure the thermistor resistance, all shown in Fig.C.1.c. In Table C.1 the thermal conductivity of the most used materials for the assembly of a laser box are shown. Based on this values the selection of the right material has been easy. The screws used are made of Delrin¹, a synthetic polymer with a thermal conductivity of 0.37 W/m·K. M3 screws 20 mm long have been

¹Polyoxymethylene.

used. Applying the formula C.1 for a $\Delta T = T_2 - T_1 = 130 \text{ }^\circ\text{C}$ one can find that the thermal load on the cold side of the TEC is $\sim 17.5 \times 10^{-3} \text{ mW}$ per screw. The laser is mounted on a holder with four clamps used to clamp the device to the holder. One of the clamp is electrically connected to a LEMO connector using a Lakeshore ultra miniature coaxial cable type C. The type C cable has both the center conductor and the drain wire made of silver plated copper. Both the wires have a diameter of 0.2 mm and they are connected to the laser holder, contributing equally to the thermal load. In order to minimize the thermal load long wires must be fitted into the laser box, making round trips around the laser holder and avoiding contacts with the sidewalls of the box. In Fig.C.1.c, a $\sim 20 \text{ cm}$ long cable (the one with the blue jacket) has been used. The total thermal load of the wires is $63.7 \times 10^{-3} \text{ W}$. For future applications a ultra miniature coaxial cable type SS would be better. On the contrary of most of the cables that employs a core of copper, the SS cables have a stainless steel core which offer thermal conductivity ~ 20 times lower than copper as visible in Table C.1, hence lower heat load than the type C cable. Finally, the thermistor is also connected using two copper wires (for a 2-wire measurement of the resistance). The copper wires have a diameter of 0.15 mm and a length of $\sim 20 \text{ cm}$. The total heat load from both the wires is $35.8 \times 10^{-3} \text{ W}$. The total heat load due to the wiring and the screws used to mount with the compression method is then $134.5 \times 10^{-3} \text{ W}$. Thermal contact between the TEC hot side and the heat sink, the laser holder and the TEC cold side and finally the laser mount and the laser holder has been achieved using Arctic silver thermal paste, which has a thermal conductivity of $8.5 \text{ W/m}\cdot\text{K}$ and assures good thermal performance down to $\sim 120 \text{ K}$. The applied paste should be as thin and homogeneous as possible; a thick paste would hinder thermal conduction due to the relatively low thermal conductivity with respects to metals, but a

Material	Thermal conductivity [W/m·K]
Teflon	0.25
Delrin	0.37
HDPE	0.5
Stainless steel	20
Copper	390
Thermal paste	0.6 – 11.5

Table C.1: Heat conductivity of common materials used in the laser box.

too thin one could lead to a bad mechanical contact. With water at 17 °C passing through the channel of the heat sink, the Peltier cell cooled down to 195 K under vacuum conditions. Assuming a hot side temperature of 27 °C, the TEC performed with a maximum $\Delta T_{\max} = 105$ K. According to Fig.C.1.a, the corresponding heat load for this temperature performance is between 0.5 and 1.0 W, indicating an under estimation of the heat load computation. This is expected because incident thermal radiation from the box itself and visible light passing through the window of the laser box are also a source of heat. Visible light radiation coming from the background noise can be screened using an HDPE window. A mylar superinsulation layer can instead used to screen the thermal radiation in case the heat load must be reduced further.

List of Figures

1.1	Electromagnetic spectrum. Image adapted from [1].	1
1.2	Examples of application of terahertz radiation in security (a,b,c) and process control (d). Adapted from [5] and based on [3,6–8].	2
1.3	Example of imaging of a basal cell carcinoma; thanks to THz imaging is possible to uncover feature under the skin which would be otherwise invisible with simple optical imaging. Adapted from [2].	3
1.4	Schematic of several THz QCL designs a) Chirped Superlattice (SL). b) Bound-to-Continuum (BtC) realized with 7 quantum wells. c) Bound-to-Continuum (BtC) realized with 4 quantum wells. d) Scattering Assisted (SA). e) Resonant Phonon (RP). f) Direct Phonon (DP). At the bottom a legend shows the meaning of each used symbol.	5
1.5	The trend of the THz QCL T_{\max} over the years with the latest results achieved in this thesis. Also the trend of the maximum temperature of the two quantum well designs is reported. Data taken from [11,16,23,24,35–38] for the maximum temperature and from [28–30,39] for the 2-well performance.	7
2.1	Drawing and cross section simulation of a) single plasmon waveguide and b) double-metal waveguide. Adapted from [31].	11
2.2	Schematic illustration of the double-metal processing steps with Cu.	15
2.3	Bonding interface comparison between thermocompressive bonding performed at different temperatures as indicated in the labeling. When moving to lower temperature, the bonding interface shows smaller and sparser voids.	17
2.4	a) Top view of a Cu-Cu process in which we observed copper diffusion into GaAs. It is clear that the black stripes, which are regions where the Cu diffused, are passing "below" the ridges, hinting that the problem arose at the interface between the carrier substrate and the sample. b) Temperature difference between the top and bottom plate during the wafer bonding will lead to differences in thermal expansions between the Cu and the active region, accumulating thermal stress and thus leading to stress release on the sample. Both these samples have been bondeed at 400 °C.	19

2.5	EDX analysis of a SEM picture, shown on the top left, taken from a sample where Cu diffused into GaAs. Brighter colors correspond to a higher percentage of the specified element. The analysis shows that there is presence of Cu diffused into GaAs.	21
2.6	a) Cross section SEM of a sample right after the ICP dry etching step with a Cl_2/Ar plasma. On top of the bottom contact a thin layer of CuCl_x forms. b) Cross section of the previous sample after the HCl etching, which removes the CuCl_x . c) Low magnification cross section of the edge of a bonded sample just etched with 50% Citric Acid (in a 3:1 solution with H_2O_2). Copper is etched by this Acid, but the penetration depth of the acid in the interface is usually limited below 100 μm	22
2.7	The absorption of BCB at 300 K. Although not optimal when above a wavenumber of 100 cm^{-1} , in this work the BCB has been used exclusively for a frequency of $\nu = 4.745 \text{ THz}$, corresponding to $\sim 158 \text{ cm}^{-1}$ (blue shaded region). Figure re-adapted from [59].	24
2.8	Schematic illustration of the BCB processing steps.	25
2.9	BCB planarization example. In the optical microscope picture, several ridges are visible and on some of them the top contact is starting to be exposed.	27
3.1	a) EV2416 and b) EV2624 band structures and respective electron densities simulated with a non-equilibrium Green's function model at maximum gain at 200 K lattice temperature. These two layers have reached high temperature operation and played a major role in the development of this work. The yellow arrow indicates the radiative transition, i is the injector level, ul the upper level state and ll the lower level state. The apex indicates that the level is relative to the following period of the structure.	31
3.2	Maximum operating temperature versus the simulated gain at 300 K for several structures. EV2413, EV2379 and EV2414 have some layer sequence but different doping, while EV2415, EV2414 and EV2416 have same doping but different injector barrier thickness. Adapted from [29].	34
3.3	a) LIV curves vs T of EV2416. The maximum temperature measured was $\sim 193.5 \text{ K}$. b) Threshold current density versus device temperature. In the inset, the spectrum of the laser at 192 K.	35
3.4	a) Maximum temperature data of EV2416 overlapped on a schematic illustration of the 3" wafer with the thickness gradient reported. It is possible to see that for chips belonging to the same processing batch there is a correlation between maximum temperature and radial position. b) Maximum gain of the design of EV2416 for small variation of both barrier and well widths versus the well widths. The maximum gain is obtained for a structure which is $\sim 3\%$ thinner than the grown one.	37
3.5	3D histogram of the statistics collected over 23 lasers with a width of 150 μm and a length between 1 and 2 mm, as specified by the color scale, versus the layer Δt with respect to the central thickness. The projection in dark grey on the XY plane sums over all the thickness variation statistics. b) LIV characteristic of the best device. The laser has been pumped electrically with 50 ns width pulses at 415 Hz and operated up to $\sim 210 \text{ K}$	39

3.6	a) The laser box with Peltier cell and mounted QCL. The box footprint ($\sim 9 \times 9 \times 5.5 \text{ cm}^3$) is significantly reduced compared to a flow cryostat (even without taking into account the He dewar). At maximum capacity, the Peltier cell uses $\lesssim 30 \text{ W}$ to cool the laser down to 195 K. b) LI curves obtained cooling down the laser in the laser box and detecting it using a He-cooled Ge bolometer. In dashed and solid black lines, a comparison between the measured IV and the simulated IV at a lattice temperature of 200 K is shown. The IV has been measured in a flow cryostat setup. In the inset, it is possible to see that the emitted frequency at 205 K fits the simulation prediction of the gain.	41
3.7	a) T_0 fit of the threshold current density J_{thres} reported on a log scale. The threshold current density versus temperature data is fitted with an exponential dependence on data points collected in cryostat operation (red circles), but agrees well with the data collected during the thermoelectric cooling operation (black triangles). A $T_0 = 229 \text{ K}$ is obtained. b) Spectra taken with the laser cooled down using a thermoelectric multistage cooler and using the DTGS room temperature detector of a Bruker Vertex 80 FTIR. Laser has been operated at maximum power.	44
3.8	Relative density of the upper laser state (n_{ULS}) calculated with a nonequilibrium Green's function (NEGF) model for five THz quantum cascade laser designs with different number of active states per period. Schematics of the simulated QCLs are shown in the five insets and represent direct phonon (DP), resonant phonon [24] (RP), scattering-assisted (SA) injection [65], 4-well [18] and 7-well [17] bound-to-continuum (BtC) designs. The DP QCL is the layer EV2624 presented in this Chapter. For each design we show the upper laser state (ULS) in red, the lower laser state (LLS) in blue, and green lines indicate the other relevant states. The vertical bars show the barriers separating the quantum wells. Image and contained data are gentle concession of Dr. Martin Franckić.	45
4.1	Atmospheric absorption at two different altitudes; Chajnantor observatories (placed at 5 km AMSL) and at 13 km AMSL. As it can be seen no THz radiation is detectable even at relatively high altitudes, forcing the scientists to find alternative solutions to the common observatories. Figure adapted from [10].	52
4.2	SOFIA with the open fuselage in order to expose the telescope and test it in a pre-flight on-ground test. Personal picture.	53
4.3	upGREAT setup schematics. Illustration adapted from [74].	54
4.4	a) Design of the prototype of a laser with an integrated slot array antenna. Adapted from [77]. b) A not in scale illustration of the laser cavity design. Five sections compose the whole cavity. Starting from the left to the right: 1) the Distributed Bragg Reflector (DBR), 2) the main cavity with a second order lateral grating, 3) a multisection tapering, 4) a front reflector based on a first order lateral grating and 5) an outcoupling patch antenna array. Adapted from [57]	56

4.5 a) On the left, the schematic of the DBR period, which works as a broadband back reflector mirror. On the right, the simulated reflectivity of the DBR section, with a maximum value higher than 90% for the target frequency band. b) On the left, the schematic of the second order grating section, which introduces losses to the higher order lateral modes. On the right, the simulated losses versus the frequency are plotted. Next to each point the simulated electric field distribution shows that for higher order lateral modes the losses increase. c) On the left, the schematic of the first order grating section, which works as a narrowband front reflector for the selection of only one longitudinal mode. On the right, the simulated reflectivity of the section, with a half width half maximum of ~ 35 GHz. 59

4.6 Examples of structures simulated with COMSOL Multiphysics. a) The n_{eff} estimation of the mode is done via 2D simulation. In color scale the electric field distribution of the fundamental TM mode is shown. b) 3D simulations have been used mainly for periodic structure. In the example the periodic boundaries of the second order lateral grating are highlighted. c) Quasi-1D simulation example of a single period of the front mirror. The gray rectangles are front mirror sections with different n_{eff} . The system is provided with two ports, but only one is excited with an electromagnetic wave at an arbitrary frequency. 61

4.7 a) illustration of a multi-section tapering composed by three isosceles trapezoids which main parameters are specified in figure. b) Transmission properties of optimized tapering. 66

4.8 a) Simulated far-field pattern. b) The threshold gain analysis computed using the 1D transfer matrix method over the whole cavity design switching between $N = 50, 60$ and 70 periods for the front mirror. The computation shows that an electromagnetic wave at frequency 4.75 THz is more likely to lase. 69

4.9 a) LIV example of a First generation device. The laser showed in this plot is obtained from EV1911 and it shows a maximum peak power of ~ 2 mW. b) First generation device spectra vs bias, acquired in continuous wave operation at 20 K. Although the majority of the devices has shown single modality over the whole dynamic range, some of them had a mode hopping close to roll-over bias. 71

4.10 Far-field example of a first generation device. The far-field presents multiple lobes, coming from the emission of several antennas at once. This issue rose from the coupling of the electromagnetic mode also to nearby antenna, using the BCB as core of a waveguide. 73

4.11 a) example of a mounted sample. In this picture, multiple devices distributed over three columns are visible. Neighbor devices are placed in opposite verses. b) A possible way to improve the far-field interference is to deposit Nickel stripes between the lasers in order to absorb leaking radiation. 74

4.12 LIV example of EV1980. The high voltage is probably due to a contact problem arisen from unidentified fabrication issues. 75

4.13 LIV performance of EV2303 both in a) continuous wave at 10 K and b) pulsed mode versus temperature at 80% duty cycle. c) panel shows the trend of J_{thres} versus the Temperature and the $T_0 = 72$ K resulted from the fit. 76

4.14	Trend of the measured frequency vs the simulated (expected) frequency of the device. The devices follow the expected trend with a statistical deviation $\sigma_{1st} = 21$ GHz for the first process and of $\sigma_{2nd} = 6$ GHz for the second process, although with an offset of $\Delta\nu = 25$ GHz.	77
4.15	a) The far field of the second generation shows a single lobe pattern. However, an interference pattern is still present due to the nearby antenna cross-talk. b) When the Nickel stripes are deposited, the cross-coupling between the laser and the neighbor antennas is weaker and the interference pattern is almost completely removed, getting a result that is close to the simulated one. For both the far field, the red dashed line represent the full width half maximum.	77
4.16	LIV in pulsed mode (above) and continuous wave (below) for EV1858. A comparison also to the layer EV2303 is shown, with an emitted power difference of almost a factor of 10.	79
4.17	In the picture (in random order): Urs Graf, Matthias Justen, Karl Jacobs, Robert Simon, Anna Parikka, Denise Riquelme, Timea Csengeri, Ronan Higgins, Oliver Ricken, Andreas Bell (and me). Thanks to you I have <i>literally</i> reached the highest altitude I will probably ever experience in my life.	81
5.1	a) Illustration of the working principle of a QWIP. When an electrical bias is applied a dark current is collected due to the free carriers in the continuum. If a photon of sufficient energy $h\nu_0 > E_{12}$ is absorbed, a photocurrent is generated thanks to the transition into the continuum of the electron that absorbed the radiation. b) Lattice match diagram for several semiconductors. $\text{In}_x\text{Ga}_{1-x}\text{As}$ and GaAs heterostructures are lattice matched only for a specific composition of 53% In [92].	84
5.2	a) band diagram structure obtained with the ΔE_c value computed using Vurgaftman et al. data [96] versus b) the band diagram structure simulated considering the strain of the material according to Arent et al. [97]	86
5.3	IV measurement of the QWIP vs temperature in three different configurations: dark condition, with a TPX window and with HDPE plus a cold window in order to screen the mid-infrared radiation. The comparison between the IV values measured in these configurations show that radiation at frequencies higher than THz frequencies are absorbed by the QWIP, contributing to the photocurrent, which is larger for the cryostat fitted with the TPX window.	90
5.4	The photocurrent spectra of the QWIP is compared directly to the band structure simulation run with the parameters obtained from 97. The spectra show good agreement with the simulation.	91
5.5	The photocurrent obtained when the detector is illuminated with 200 μW power at 4.663 THz (spectrum shown in inset).	92
5.6	LIV characteristics of a laser obtained from EV1858 versus a) the QWIP temperature and b) the QWIP operation bias.	93
5.7	a) Top view of the design model of the microcavity QWIP simulated on CST. The red triangle at the intersection of the patch array antenna branches indicates the area of the microcavity mesa. b) The z-component (growth direction) of the electric field distribution when the model is excited with a plane wave coming from the top and polarized along the x-axis.	95

5.8	a) and b) report SEM picture of the as-etched microcavity. c), d) and e) are optical microscopy picture of the completed sample at different magnifications.	96
5.9	a) IV characteristic in dark environment and b) compared at 7 K with the reference mesa.	98
5.10	Laser spectra acquired with the microcavity QWIP and plotted in logarithmic scale. In a) the spectra are shown vs the applied bias of the microcavity QWIP reporting also the spectra acquired at 200 mV with the reference mesa for direct comparison. In b) the normalized spectra at 200 mV is compared with the reference mesa.	99
B.1	LIV performance of EV2610 are plotted with different top metallization. The as-grown sample (dashed line) has poor performance when deposited with a standard Ti/Au contact, probably due to InAu alloying at the interface between the active region and the metallization. When the top contact of the active region is etched using HCl and Ar ion bombardment, the maximum temperature performance improves because the amount of In is reduced (dotted line). Eventually, a top metallization composed by Pt/Au proved to avoid any InAu alloying and outclassed in performance the other configurations (solid line). . . .	113
B.2	LIV performance of EV2587 are plotted with different top contact growth. The as-grown sample (dashed line) has poor performance when deposited with a standard Ti/Au contact, probably due to InAu alloying at the interface between the active region and the metallization. When the top contact of the active region is etched using HCl and Ar ion bombardment, the maximum temperature performance improves because the amount of In is reduced (dotted line). Eventually, a top metallization composed by Pt/Au proved to avoid any InAu alloying and outclassed in performance the other configurations (solid line). . . .	114
C.1	a) Specifications of the adopted thermoelectric cooler (TEC) with a hot side temperature of 27 °. The TEC has a resistance of 0.5 Ω b) The copper base of the laser box is engraved with a serpentine channel in order to make water flow below the hot side of the Peltier cell. c) A picture of the laser box. Delrin screws and long wire connections are important to reduce drastically the heat load on the cold side of the TEC.	117

List of Tables

2.1	Summary of the main steps for a Cu-Cu double metal waveguide fabrication. Further details on the used recipes and similar processes in the Appendix.	14
3.1	Summary of all the 2QW layers tested and the comments on the peculiarities and/or performances of these layers. In the layer sequence, the italic refers to the wells, the bold to the barrier and the underlined numbers are doped.	48
3.2	Summary of all the 2QW layers tested and the comments on the peculiarity and/or performances of these layers. The number or processes (Pr.) executed on the given layer is specified and the maximum temperature in square bracket refers to Cu-Cu double metal processes.	49
4.1	Optimized parameters for a multi-section tapering at 4.75 THz.	65
5.1	Table summarizing the main differences between the InGaAs/GaAs QWIP simulations with parameters adopted from two different source 96 and 97. $\Delta E_c(2\%)$ is the conduction band discontinuity between $\text{In}_{0.02}\text{Ga}_{0.98}\text{As}$ and GaAs, E_1 the confinement energy of the first eigenstate, E_{21} and z_{21} respectively the energy difference and the dipole moment between the excited and the ground level.	87
A.1	Summary of the main steps for Au-Au double metal dry-etched waveguide fabrication for a GaAs/AlGaAs heterostructure.	104
A.2	Summary of the main steps for Au-Au double metal wet-etched waveguide fabrication for a GaAs/AlGaAs heterostructure.	105
A.3	Summary of the main steps for Au-Au double metal dry-etched mesa fabrication with ohmic contacts for a InGaAs/GaAs heterostructure . . .	106
A.4	Summary of the main steps for Au-Au double metal waveguide fabrication for a InP/InGaAs/InGaSb/AlInAs heterostructure.	107
A.5	Soft baking of BCB	110
A.6	Hard baking of BCB, used after the last spinning.	110
A.7	Etching parameters of BCB.	110

C.1 Heat conductivity of common materials used in the laser box. 119

Bibliography

- [1] G. Pacchioni, "<http://blogs.nature.com/onyourwavelength/2018/05/21/terahertz-entering-applications>", 2018.
- [2] S. S. Dhillon, M. S. Vitiello, E. H. Linfield, A. G. Davies, M. C. Hoffmann, J. Booske, C. Paoloni, M. Gensch, P. Weightman, G. P. Williams, E. Castro-Camus, D. R. Cumming, F. Simoens, I. Escorcia-Carranza, J. Grant, S. Lucyszyn, M. Kuwata-Gonokami, K. Konishi, M. Koch, C. A. Schmuttenmaer, T. L. Cocker, R. Huber, A. G. Markelz, Z. D. Taylor, V. P. Wallace, J. Axel Zeitler, J. Sibik, T. M. Korter, B. Ellison, S. Rea, P. Goldsmith, K. B. Cooper, R. Appleby, D. Pardo, P. G. Huggard, V. Krozer, H. Shams, M. Fice, C. Renaud, A. Seeds, A. Stöhr, M. Naftaly, N. Ridler, R. Clarke, J. E. Cunningham, and M. B. Johnston, "The 2017 terahertz science and technology roadmap," *Journal of Physics D: Applied Physics*, vol. 50, no. 4, 2017.
- [3] M. Tonouchi, "Cutting-edge terahertz technology," *Nature Photonics*, vol. 1, no. 2, pp. 97–105, 2007.
- [4] N. Palka, "Identification of concealed materials, including explosives, by terahertz reflection spectroscopy," *Optical Engineering*, vol. 53, no. 3, p. 031202, 2013.
- [5] D. Turcinkova, *Terahertz Quantum Cascade Lasers for Astronomical Applications*. PhD thesis, 2015.
- [6] K. Sengupta, "Tiny low cost terahertz imager chip."
- [7] M. Theuer, S. S. Harsha, D. Molter, G. Torosyan, and R. Beigang, "Terahertz time-domain spectroscopy of gases, liquids, and solids," *ChemPhysChem*, vol. 12, no. 15, pp. 2695–2705, 2011.
- [8] A. Y. Pawar, D. D. Sonawane, K. B. Erande, and D. V. Derle, "Terahertz technology and its applications," *Drug Invention Today*, vol. 5, no. 2, pp. 157–163, 2013.

- [9] V. P. Wallace, A. J. Fitzgerald, S. Shankar, N. Flanagan, R. Pye, J. Cluff, and D. D. Arnone, "Terahertz pulsed imaging of basal cell carcinoma ex vivo and in vivo," *British Journal of Dermatology*, vol. 151, no. 2, pp. 424–432, 2004.
- [10] E. T. Young, E. E. Becklin, P. M. Marcum, T. L. Roellig, J. M. De Buizer, T. L. Herter, R. Güsten, E. W. Dunham, P. Temi, B. G. Andersson, D. Backman, M. Burgdorf, L. J. Caroff, S. C. Casey, J. A. Davidson, E. F. Erickson, R. D. Gehrz, D. A. Harper, P. M. Harvey, L. A. Helton, S. D. Horner, C. D. Howard, R. Klein, A. Krabbe, I. S. McLean, A. W. Meyer, J. W. Miles, M. R. Morris, W. T. Reach, J. Rho, M. J. Richter, H. P. Roeser, G. Sandell, R. Sankrit, M. L. Savage, E. C. Smith, R. Y. Shuping, W. D. Vacca, J. E. Vaillancourt, J. Wolf, and H. Zinnecker, "Early science with SOFIA, the stratospheric observatory for infrared astronomy," *Astrophysical Journal Letters*, vol. 749, no. 2, 2012.
- [11] R. Köhler, A. Tredicucci, F. Beltram, H. E. Beere, E. H. Linfield, a. G. Davies, D. a. Ritchie, R. C. Iotti, and F. Rossi, "Terahertz semiconductor-heterostructure laser," *Nature*, vol. 417, no. 6885, pp. 156–159, 2002.
- [12] J. Faist, F. Capasso, D. Sivco, C. Sirtori, A. Hutchinson, and A. Cho, "Quantum Cascade Laser," *Science*, vol. 264, no. 5158, pp. 553–556, 1994.
- [13] A. Tredicucci, F. Capasso, C. Gmachl, D. L. Sivco, A. L. Hutchinson, and A. Y. Cho, "High performance interminiband quantum cascade lasers with graded superlattices," *Applied Physics Letters*, vol. 73, no. 15, pp. 2101–2103, 1998.
- [14] C. Sirtori, P. Kruck, S. Barbieri, P. Collot, J. Nagle, M. Beck, J. Faist, and U. Oesterle, "GaAs/AlxGa1-xAs quantum cascade lasers," *Applied Physics Letters*, vol. 73, no. 24, pp. 3486–3488, 1998.
- [15] M. Beck, D. Hofstetter, T. Aellen, J. Faist, U. Oesterle, M. Ilegems, E. Gini, and H. Melchior, "Continuous wave operation of a mid-infrared semiconductor laser at room temperature," *Science*, vol. 295, no. 5553, pp. 301–305, 2002.
- [16] G. Scalari, L. Ajili, J. Faist, H. Beere, E. Linfield, D. Ritchie, and G. Davies, "Far-infrared ($\lambda \approx 7 \mu\text{m}$) bound-to-continuum quantum-cascade lasers operating up to 90 K," *Applied Physics Letters*, vol. 82, no. 19, pp. 3165–3167, 2003.
- [17] G. Scalari, N. Hoyler, M. Giovannini, and J. Faist, "Terahertz bound-to-continuum quantum-cascade lasers based on optical-phonon scattering extraction," *Applied Physics Letters*, vol. 86, no. 18, pp. 1–3, 2005.
- [18] M. I. Amanti, G. Scalari, R. Terazzi, M. Fischer, M. Beck, J. Faist, A. Rudra, P. Gallo, and E. Kapon, "Bound-to-continuum terahertz quantum cascade laser with a single-quantum-well phonon extraction/injection stage," *New Journal of Physics*, vol. 11, 2009.
- [19] S. Barbieri, J. Alton, H. E. Beere, J. Fowler, E. H. Linfield, and D. A. Ritchie, "2.9 THz quantum cascade lasers operating up to 70 K in continuous wave," *Applied Physics Letters*, vol. 85, no. 10, pp. 1674–1676, 2004.

- [20] M. Wienold, L. Schrottke, M. Giehler, R. Hey, W. Anders, and H. T. Grahn, "Low-threshold terahertz quantum-cascade lasers based on GaAs/Al_{0.25}Ga_{0.75}As heterostructures," *Applied Physics Letters*, vol. 97, no. 7, pp. 1–4, 2010.
- [21] L. Lianhe, L. Chen, J. Zhu, J. Freeman, P. Dean, A. Valavanis, A. Davies, and E. Linfield, "Terahertz quantum cascade lasers with >1 W output powers," *Electronics Letters*, vol. 50, no. 4, pp. 309–311, 2014.
- [22] H. Luo, S. R. Laframboise, Z. R. Wasilewski, G. C. Aers, H. C. Liu, and J. C. Cao, "Terahertz quantum-cascade lasers based on a three-well active module," *Applied Physics Letters*, vol. 90, no. 4, pp. 1–3, 2007.
- [23] S. Kumar, Q. Hu, and J. L. Reno, "186 K operation of terahertz quantum-cascade lasers based on a diagonal design," *Applied Physics Letters*, vol. 94, no. 13, pp. 2–4, 2009.
- [24] S. Fatholouloumi, E. Dupont, C. Chan, Z. Wasilewski, S. Laframboise, D. Ban, A. Mátyás, C. Jirauschek, Q. Hu, and H. C. Liu, "Terahertz quantum cascade lasers operating up to ~ 200 K with optimized oscillator strength and improved injection tunneling," *Optics Express*, vol. 20, no. 4, p. 3866, 2012.
- [25] E. Dupont, S. Fatholouloumi, Z. R. Wasilewski, G. Aers, S. R. Laframboise, M. Lindskog, S. G. Razavipour, A. Wacker, D. Ban, and H. C. Liu, "A phonon scattering assisted injection and extraction based terahertz quantum cascade laser," *Journal of Applied Physics*, vol. 111, no. 7, 2012.
- [26] J. Faist and G. Scalari, "Unified description of resonant tunnelling diodes and terahertz quantum cascade lasers," *Electronics Letters*, vol. 46, p. S46, 2010.
- [27] A. Wacker, "Extraction-controlled quantum cascade lasers," *Applied Physics Letters*, vol. 97, no. 8, pp. 8–10, 2010.
- [28] G. Scalari, M. I. Amanti, C. Walther, R. Terazzi, M. Beck, and J. Faist, "Broadband THz lasing from a photon-phonon quantum cascade structure.," *Optics express*, vol. 18, no. 8, pp. 8043–8052, 2010.
- [29] M. Franckí, L. Bosco, M. Beck, C. Bonzon, E. Mavrona, G. Scalari, A. Wacker, and J. Faist, "Two-well quantum cascade laser optimization by non-equilibrium Green's function modelling," *Applied Physics Letters*, vol. 112, no. 2, 2018.
- [30] A. Albo, Y. V. Flores, Q. Hu, and J. L. Reno, "Two-well terahertz quantum cascade lasers with suppressed carrier leakage," *Applied Physics Letters*, vol. 111, no. 11, pp. 1–6, 2017.
- [31] B. S. Williams, "Terahertz quantum-cascade lasers," *Nature Photonics*, vol. 1, no. 517, pp. 517–525, 2007.
- [32] M. Brandstetter, C. Deutsch, M. Krall, H. Detz, D. C. Macfarland, T. Zederbauer, A. M. Andrews, W. Schrenk, G. Strasser, and K. Unterrainer, "High power terahertz quantum cascade lasers with symmetric wafer bonded active regions," *Applied Physics Letters*, vol. 103, no. 17, 2013.

- [33] C. Sirtori, S. Barbieri, and R. Colombelli, "Wave engineering with THz quantum cascade lasers," *Nature Photonics*, vol. 7, no. 9, pp. 691–701, 2013.
- [34] M. Rösch, G. Scalari, M. Beck, and J. Faist, "Octave-spanning semiconductor laser," *Nature Photonics*, vol. 9, no. 1, pp. 42–47, 2014.
- [35] B. S. Williams, S. Kumar, H. Callebaut, Q. Hu, and J. L. Reno, "Terahertz quantum-cascade laser operating up to 137 K," *Applied Physics Letters*, vol. 83, no. 25, pp. 5142–5144, 2003.
- [36] B. S. Williams, S. Kumar, Q. Hu, and J. L. Reno, "Operation of terahertz quantum-cascade lasers at 164 K in pulsed mode and at 117 K in continuous-wave mode," *Optics Express*, vol. 13, no. 9, p. 3331, 2005.
- [37] S. Kumar, B. S. Williams, Q. Qin, and A. W. M. Lee, "Terahertz quantum-cascade lasers with resonant-phonon depopulation: high-temperature and low frequency operation THz Applications imaging, spectroscopy, sensing," *October*, 2007.
- [38] M. a. Belkin, J. a. Fan, S. Hormoz, F. Capasso, S. P. Khanna, M. Lachab, a. G. Davies, and E. H. Linfield, "Terahertz quantum cascade lasers with copper metal-metal waveguides operating up to 178 K.," *Optics express*, vol. 16, no. 5, pp. 3242–3248, 2008.
- [39] S. Kumar, C. W. I. Chan, Q. Hu, and J. L. Reno, "Two-well terahertz quantum-cascade laser with direct intrawell-phonon depopulation," *Applied Physics Letters*, vol. 95, no. 14, pp. 2009–2011, 2009.
- [40] M. A. Belkin, F. Capasso, A. Belyanin, D. L. Sivco, A. Y. Cho, D. C. Oakley, C. J. Vineis, and G. W. Turner, "Terahertz quantum-cascade-laser source based on intracavity difference-frequency generation," *Nature Photonics*, vol. 1, no. 5, pp. 288–292, 2007.
- [41] M. A. Belkin, F. Capasso, F. Xie, A. Belyanin, M. Fischer, A. Wittmann, and J. Faist, "Room temperature terahertz quantum cascade laser source based on intracavity difference-frequency generation," *Applied Physics Letters*, vol. 92, no. 20, pp. 128–130, 2008.
- [42] "FLASH project."
- [43] "ZOTERAC project."
- [44] G. Sun, R. A. Soref, and J. B. Khurgin, "Active region design of a terahertz GaN/Al_{0.15}Ga_{0.85}N quantum cascade laser," *Superlattices and Microstructures*, vol. 37, no. 2, pp. 107–113, 2005.
- [45] P. Dean, A. Valavanis, J. Keeley, K. Bertling, Y. L. Lim, R. Alhathlool, A. D. Burnett, L. H. Li, S. P. Khanna, D. Indjin, T. Taimre, A. D. Rakić, E. H. Linfield, and A. G. Davies, "Terahertz imaging using quantum cascade lasers - A review of systems and applications," *Journal of Physics D: Applied Physics*, vol. 47, no. 37, 2014.

- [46] IBM, "Copper Interconnects," 2012.
- [47] S. Kumar, "Development of THz Quantum-Cascade Lasers," *PhD Thesis*, 2007.
- [48] M. A. Belkin, Q. J. Wang, C. Pflügl, A. Belyanin, S. P. Khanna, A. G. Davies, E. H. Linfield, and F. Capasso, "High-temperature operation of terahertz quantum cascade laser sources," *IEEE Journal on Selected Topics in Quantum Electronics*, vol. 15, no. 3, pp. 952–967, 2009.
- [49] S. Fatholouloumi, E. Dupont, Z. R. Wasilewski, C. W. I. Chan, S. G. Razavipour, S. R. Laframboise, S. Huang, Q. Hu, D. Ban, and H. C. Liu, "Effect of oscillator strength and intermediate resonance on the performance of resonant phonon-based terahertz quantum cascade lasers," *Journal of Applied Physics*, vol. 113, no. 11, 2013.
- [50] K. L. Chavez and D. W. Hess, "A Novel Method of Etching Copper Oxide Using Acetic Acid," *Journal of The Electrochemical Society*, vol. 148, no. 11, p. G640, 2001.
- [51] F. Hasegawa, "Different diffusion behavior of copper in epitaxial and in bulk GaAs," *Journal of Applied Physics*, vol. 45, no. 5, pp. 1944–1947, 1974.
- [52] C.-Y. Chen, L. Chang, E. Y. Chang, S.-H. Chen, and D.-F. Chang, "Thermal stability of Cu/Ta/GaAs multilayers," *Applied Physics Letters*, vol. 77, no. 21, pp. 3367–3369, 2000.
- [53] S. Lee and Y. Kuo, "Chlorine Plasma/Copper Reaction in a New Copper Dry Etching Process," *Journal of The Electrochemical Society*, vol. 148, no. 9, p. G524, 2002.
- [54] L. Masini, S. Meucci, J. Xu, R. Degl'Innocenti, F. Castellano, H. E. Beere, D. Ritchie, D. Balduzzi, R. Puglisi, A. Galli, F. Beltram, M. S. Vitiello, M. Cecchini, and A. Tredicucci, "Terahertz probe of individual subwavelength objects in a water environment," *Laser and Photonics Reviews*, vol. 8, no. 5, pp. 734–742, 2014.
- [55] H. Zhang, G. Scalari, J. Faist, L. A. Dunbar, and R. Houdré, "Design and fabrication technology for high performance electrical pumped terahertz photonic crystal band edge lasers with complete photonic band gap," *Journal of Applied Physics*, vol. 108, no. 9, 2010.
- [56] M. Justen, C. Bonzon, K. Ohtani, M. Beck, U. Graf, and J. Faist, "2D patch antenna array on a double metal quantum cascade laser with >90% coupling to a Gaussian beam and selectable facet transparency at 19 THz," *Optics Letters*, vol. 41, no. 19, p. 4590, 2016.
- [57] L. Bosco, C. Bonzon, K. Ohtani, M. Justen, M. Beck, and J. Faist, "A patch-array antenna single-mode low electrical dissipation continuous wave terahertz quantum cascade laser," *Applied Physics Letters*, vol. 109, no. 20, 2016.

- [58] Z. Diao, C. Bonzon, G. Scalari, M. Beck, J. Faist, and R. Houdré, "Continuous-wave vertically emitting photonic crystal terahertz laser," *Laser and Photonics Reviews*, vol. 7, no. 5, pp. 45–50, 2013.
- [59] C. B. P. Bonzon, *Phase and mode control of structured semiconductor lasers*. PhD thesis, 2016.
- [60] R. D. Tacito, "Patterning of Benzocyclobutene by Reactive Ion Etching," *Journal of The Electrochemical Society*, vol. 143, no. 8, p. 2695, 1996.
- [61] E. B. Liao, W. H. Teh, K. W. Teoh, A. A. Tay, H. H. Feng, and R. Kumar, "Etching control of benzocyclobutene in CF_4 / O_2 and SF_6 / O_2 plasmas with thick photoresist and titanium masks," *Thin Solid Films*, vol. 504, no. 1-2, pp. 252–256, 2006.
- [62] A. Wacker, M. Lindskog, and D. O. Winge, "Nonequilibrium Green's function model for simulation of quantum cascade laser devices under operating conditions," *IEEE Journal on Selected Topics in Quantum Electronics*, vol. 19, no. 5, pp. 1–11, 2013.
- [63] M. Franckić, "Aftershoq," 2018.
- [64] S. Kohen, B. S. Williams, and Q. Hu, "Electromagnetic modeling of terahertz quantum cascade laser waveguides and resonators," *Journal of Applied Physics*, vol. 97, no. 5, 2005.
- [65] S. G. Razavipour, E. Dupont, S. Fatholouloumi, C. W. Chan, M. Lindskog, Z. R. Wasilewski, G. Aers, S. R. Laframboise, A. Wacker, Q. Hu, D. Ban, and H. C. Liu, "An indirectly pumped terahertz quantum cascade laser with low injection coupling strength operating above 150 K," *Journal of Applied Physics*, vol. 113, no. 20, 2013.
- [66] J. Faist, "Wallplug efficiency of quantum cascade lasers: Critical parameters and fundamental limits," *Applied Physics Letters*, vol. 90, no. 25, pp. 23–25, 2007.
- [67] R. T. Boreiko, A. L. Betz, and J. Zmuidzinis, "Heterodyne Spectroscopy of the 158 micron CII Line in M42," *The Astrophysical Journal*, vol. 325, pp. L47–L51, 1988.
- [68] R. T. Boreiko and a.L. Betz, "Heterodyne Spectroscopy of the 63 micron O I Line in M42," *ApJ*, vol. 464, p. 11, 1996.
- [69] H. R. Carleton and W. T. Maloney, "A Balanced Optical Heterodyne Detector," *Applied Optics*, vol. 7, no. 6, p. 1241, 1968.
- [70] P. Putz, K. Jacobs, M. Justen, F. Schomaker, M. Schultz, S. Wulff, and C. E. Honingh, "NbTiN hot electron bolometer waveguide mixers on Si₃N₄ membranes at THz frequencies," *IEEE Transactions on Applied Superconductivity*, vol. 21, no. 3 PART 1, pp. 636–639, 2011.

- [71] D. Buchel, P. Putz, K. Jacobs, M. Schultz, U. U. Graf, C. Risacher, H. Richter, O. Ricken, H. W. Hubers, R. Gusten, C. E. Honingh, and J. Stutzki, "4.7-THz superconducting hot electron bolometer waveguide mixer," *IEEE Transactions on Terahertz Science and Technology*, vol. 5, no. 2, pp. 207–214, 2015.
- [72] J. Amos, "Herschel space telescope finishes mission."
- [73] E. E. Becklin and L. J. Moon, "Stratospheric Observatory For Infrared Astronomy (SOFIA)," *Symposium - International Astronomical Union*, vol. 211, no. August 1991, pp. 465–470, 1991.
- [74] C. Risacher, R. Güsten, J. Stutzki, H.-W. Hübbers, R. Aladro, A. Bell, C. Buchbender, D. Büchel, T. Csengeri, C. Duran, U. U. Graf, R. D. Higgins, C. E. Honingh, K. Jacobs, M. Justen, B. Klein, M. Mertens, Y. Okada, A. Parikka, P. Pütz, N. Reyes, H. Richter, O. Ricken, D. Riquelme, N. Rothbart, N. Schneider, R. Simon, M. Wienold, H. Wiesemeyer, M. Ziebart, P. Fusco, S. Rosner, and B. Wohler, "The upGREAT Dual Frequency Heterodyne Arrays for SOFIA," *Journal of Astronomical Instrumentation*, vol. 07, no. 04, p. 1840014, 2018.
- [75] "SOFIA Instruments, <https://www.sofia.usra.edu/science/instruments/>."
- [76] S. Heyminck, U. U. Graf, R. Güsten, J. Stutzki, H. W. Hübbers, and P. Hartogh, "GREAT: the SOFIA high-frequency heterodyne instrument," *Astronomy & Astrophysics*, vol. 542, p. L1, 2012.
- [77] C. Bonzon, I. C. Benea Chelms, K. Ohtani, M. Geiser, M. Beck, and J. Faist, "Integrated patch and slot array antenna for terahertz quantum cascade lasers at 4.7 THz," *Applied Physics Letters*, vol. 104, no. 16, 2014.
- [78] H. Richter, M. Wienold, L. Schrottke, K. Biermann, H. T. Grahn, and H.-W. Hubers, "4.7-THz Local Oscillator for the GREAT Heterodyne Spectrometer on SOFIA," *IEEE Transactions on Terahertz Science and Technology*, vol. 5, no. 4, pp. 539–545, 2015.
- [79] T.-Y. Kao, Q. Hu, and J. L. Reno, "Perfectly phase-matched third-order distributed feedback terahertz quantum-cascade lasers.," *Optics letters*, vol. 37, no. 11, pp. 2070–2, 2012.
- [80] K. Ohtani, "Internal communication,"
- [81] J. Faist, "Quantum cascade lasers," *Oxford e*, vol. 2, no. c, pp. 2–3, 2014.
- [82] D. Vermeulen, K. Van Acoleyen, and S. Ghosh, "Efficient tapering to the fundamental quasi-TM mode in asymmetrical waveguides," *15th European conference on Integrated Optics*, pp. 2–3, 2010.
- [83] K. Ohtani, D. Turčínková, C. Bonzon, I.-C. Benea-Chelms, M. Beck, and J. Faist, "High performance 4.7 THz GaAs quantum cascade lasers based on four quantum wells," *New Journal of Physics*, vol. 18, no. 123004, 2016.

- [84] L. Xu, C. A. Curwen, J. L. Reno, and B. S. Williams, "High performance terahertz metasurface quantum-cascade VECSEL with an intra-cryostat cavity," *Applied Physics Letters*, vol. 111, no. 10, 2017.
- [85] H. Schneider and H. Liu, "Photoconductive QWIP," in *Quantum Well Infrared Photodetectors*, pp. 45–81, 2007.
- [86] F. Castellano, "Quantum Well Photodetectors," in *Physics and Applications of Terahertz Radiation* (M. Perenzoni and D. J. Paul, eds.), pp. 3–34, Springer Netherlands, 2014.
- [87] D. Palaferri, Y. Todorov, Y. N. Chen, J. Madeo, A. Vasanelli, L. H. Li, A. G. Davies, E. H. Linfield, and C. Sirtori, "Patch antenna terahertz photodetectors," *Applied Physics Letters*, vol. 106, no. 16, pp. 1–6, 2015.
- [88] D. Palaferri, Y. Todorov, A. Bigioli, A. Mottaghizadeh, D. Gacemi, A. Calabrese, A. Vasanelli, L. Li, A. G. Davies, E. H. Linfield, F. Kapsalidis, M. Beck, J. Faist, and C. Sirtori, "Room-temperature nine- μm -wavelength photodetectors and GHz-frequency heterodyne receivers," *Nature*, vol. 556, no. 7699, pp. 85–88, 2018.
- [89] B. Paulillo, J. M. Manceau, A. Degiron, N. Zerounian, G. Beaudoin, I. Sagnes, and R. Colombelli, "Circuit-tunable sub-wavelength THz resonators: hybridizing optical cavities and loop antennas," *Optics Express*, vol. 22, no. 18, p. 21302, 2014.
- [90] Y. S. Lee, *Principles of terahertz science and technology*. 2009.
- [91] M. Graf, G. Scalari, D. Hofstetter, J. Faist, H. Beere, E. Linfield, D. Ritchie, and G. Davies, "Terahertz range quantum well infrared photodetector," *Applied Physics Letters*, vol. 84, no. 4, pp. 475–477, 2004.
- [92] C. Downs and T. E. Vandervelde, *Progress in infrared photodetectors since 2000*, vol. 13. 2013.
- [93] H. C. Liu, H. Luo, C. Y. Song, Z. R. Wasilewski, a. J. Spring Thorpe, and J. C. Cao, "Design of terahertz quantum well photodetectors," *Infrared Physics and Technology*, vol. 50, no. 2-3, pp. 191–193, 2007.
- [94] A. Maros, N. Faleev, R. R. King, C. B. Honsberg, D. Convey, H. Xie, and F. A. Ponce, "Critical thickness investigation of MBE-grown GaInAs/GaAs and GaAsSb/GaAs heterostructures," *Journal of Vacuum Science & Technology B, Nanotechnology and Microelectronics: Materials, Processing, Measurement, and Phenomena*, vol. 34, no. 2, p. 02L113, 2016.
- [95] E. T. Yu, J. O. McCaldin, and T. C. McGill, *Band Offsets in Semiconductor Heterojunctions*, vol. 46. 1992.
- [96] I. Vurgaftman, J. R. Meyer, and L. R. Ram-Mohan, "Band parameters for III-V compound semiconductors and their alloys," *Journal of Applied Physics*, vol. 89, no. 11 I, pp. 5815–5875, 2001.

- [97] D. J. Arent, K. Deneffe, C. Van Hoof, J. De Boeck, and G. Borghs, "Strain effects and band offsets in GaAs/InGaAs strained layered quantum structures," *Journal of Applied Physics*, vol. 66, no. 4, pp. 1739–1747, 1989.
- [98] M. Helm, *Chapter 1 The Basic Physics of Intersubband Transitions*, vol. 62. 1999.
- [99] D. Palaferri, Y. Todorov, A. Mottaghizadeh, G. Frucci, G. Biasiol, and C. Sirtori, "Ultra-subwavelength resonators for high temperature high performance quantum detectors," *New Journal of Physics*, vol. 18, no. 11, 2016.
- [100] L. C. Andreani, J. Gérard, and G. Panzarini, "Strong-coupling regime for quantum boxes in pillar microcavities: theory," *Physical Review B - Condensed Matter and Materials Physics*, vol. 60, no. 19, pp. 13276–13279, 1999.
- [101] C. M. Maissen, *Ultrastrong Light-Matter Coupling with Metasurfaces*. PhD thesis, ETH Zurich, 2016.